

**Design and Construction of a Fibre
Interferometer for the Study of MEMS
and NEMS to Temperatures Below 1 K**

Mark James Patton, MSci

Thesis submitted to the University of Nottingham
for the degree of Doctor of Philosophy

July 2013

Abstract

Optical interferometry offers a powerful tool for the study of the mechanical motion of micro- and nano-electromechanical systems (MEMS and NEMS). By examining the modulation of reflected light the displacement can be measured with sub-nanometre precision. Recent work with fibre interferometers carried out by other groups has studied the motion of nanomechanical systems down to temperatures as low as 1 K.

Dissipation measurements in the last few years of a number of devices fabricated from high-stress amorphous silicon nitride have shown a marked increase in quality factors when compared to similar low-stress devices. The high quality factors and small masses of these devices have attracted a great deal of interest within the nanomechanical and optomechanical communities.

Measurements of dissipation in nanomechanical resonators carried out in Nottingham to date have used the magnetomotive effect to detect nanomechanical motion. This has required that a layer of metal be applied to the high-stress silicon nitride, modifying the mechanical properties. In this thesis we present an overview of the design and construction of an optical detection system designed to study MEMS and NEMS devices from room temperature to liquid helium temperatures. Optical detection is able to measure the displacement of purely dielectric structures and as such is an ideal method with which to measure dissipation in these high-Q silicon nitride resonators, complementing the other nanomechanical measurement techniques available within Nottingham.

Using this system, measurements have been made on a number of micro- and nano-electromechanical systems fabricated using processes developed during this work. Con-

focal images of these devices obtained using the fibre interferometer show a spatial resolution of $0.75 \mu\text{m}$, a value close to the diffraction limit of the system.

Micromechanical quartz tuning forks have been measured to confirm the frequency response of the interferometer, with a value for the piezo-electro-mechanical coupling constant of $\alpha = 2.18 \pm 0.06 \mu\text{Cm}^{-1}$ obtained that is in very good agreement with the values published in the literature.

Nanomechanical measurements of $200 \mu\text{m}$ square high-stress silicon nitride membranes have revealed thermoelastic damping to be the limiting dissipation mechanism for these resonators at room temperature. Using elastic theory it is possible to quantify the fQ floor predicted by thermoelastic damping seeing good agreement with experimental data.

At lower temperatures inter-membrane coupling was observed, with acoustic vibrations from neighbouring membranes coupling into and being amplified by the membrane under observation. Discrepancies in quality factor between the observed and unobserved membranes are most likely due to optomechanical damping of the observed membrane by the laser. This inter-membrane coupling offers a powerful technique for the indirect observation of the flexural modes of nearby membranes without optically damping the response.

For my grandparents.

Acknowledgements

Over the past five years I have been fortunate enough to have received support and guidance from my supervisors Dr Chris Mellor, Prof John Owers-Bradley and Dr Andrew Armour who have always been on hand to offer assistance. I am especially indebted to Chris who let me loose on his dilution fridge to build the interferometer and was on hand to provide assistance in all aspects of the project from low-temperature physics to nano fabrication. I would also like to thank the other members (past and present) of the NEMS group, Dr. Ananth Venkatesan, Dr. Kunal Lulla and Richard who I have been lucky enough to work with and who were always willing to lend a hand where needed. I also owe a big thank you to Dr Jessica Maclean for her help with proof reading some of the thesis and sharing her nano fabrication expertise with me.

The experimental work carried out in this thesis would not have been possible without the expertise of the support staff of the physics department. I'm sure that all of them over the past 5 years have contributed in some way to this PhD, but special mentions must go to Dave Holt for building the interferometer (and anything else I may have needed); Dave Laird for building the sample holders; Chris Pallender for keeping me supplied with liquid helium; Steve Booth for putting his mountaineering skills to good use on top of the cryostat to install the rf lines; Bob Chettle for building the amplifier for the photomultiplier tube; Sue and Jeff for keeping me stocked with all the little things I needed; Jas and Dave for keeping the cleanrooms running and being on hand when things weren't working and Pete Smith for always finding a technician to help with all the things I needed yesterday!

On a personal note I would also like to thank the friends I have made along the way that have all contributed in some way to a memorable and enjoyable period in Nottingham. I have been fortunate enough to not only work, but also to socialise with the other PhD students and postdocs within the department. My thanks go to them for the illuminating discussions in the tea-room and pub. There have been many people over the years, but of special note are Toni, Daphne, Kuldeep, Duncan, Lucy, Ryan (and Sam), Andy, Jau-Yi, Jan, Fintan, Suzie, Joe, Mu and everyone else. I am also grateful to Hector (who I also had the pleasure of living with for 6 months) for his friendship and support through the years.

For three years I was fortunate enough to be a tutor in Lincoln Hall where I have met many wonderful people whose friendships I will carry forward with me as I leave Nottingham and without whose support I would not have finished this thesis: Joanne and Peter Wright, Peter J, Steph, Manu, Mel, Alex, Jing, Zeynep (and Peter), Hengameh, Ben and Chris. I am especially grateful to Zeynep and Stephanie who were always there for me when I needed them and to Jing whose kindness and positive spirit has always bought a smile to my face. Two other people I have been lucky enough to meet during my time in Nottingham are Yves and Kate (and Bolt), who I am fortunate to count as good friends and to whom I will be forever grateful for their support that made the final submission of this thesis easier.

One of the most important people that I have met during my time in Nottingham is Jara who I was lucky enough to know not only through the Physics department but also through Lincoln Hall. She has always been a person I could rely on and who has always been (and I hope always will be) there for me when I needed her and without whose constant and unwavering support I would not have made it to this point.

The final and biggest thank you must go to my family; my parents, brothers, grandparents (for who I write this thesis) and all of my aunts and uncles. Without their unconditional love and support that has made me who I am today it would not have been possible to submit this thesis.

Thank you.

Contents

1	Introduction	2
1.1	Dissipation	2
1.2	Nanomechanical Displacement Detection Techniques	4
1.2.1	Magnetomotive Actuation and Detection	5
1.2.2	Capacitive Detection	6
	Gradient Field Transduction	7
1.2.3	Optical Detection	9
1.3	Outline of Thesis	9
2	Nanomechanical Systems	12
2.1	Mechanics of Resonant Systems	12
2.2	Frequency Calculations	15
2.2.1	Torsional Resonators	15
2.2.2	Membranes	18
	Rectangular Membrane	19
	Circular Membrane	20
2.3	Dissipation in Nanomechanical Devices	23
2.3.1	Extrinsic Mechanisms	25
	Gas Damping	25
	Clamping Losses	26
	Transducer Damping	26

2.3.2	Intrinsic Mechanisms	27
	Thermoelastic Damping	27
	Surface Effects	27
	Two-Level Systems	27
2.4	Review of Measurements in Silicon Nitride Systems	29
2.4.1	Dissipation in Doubly-Clamped Beams	29
2.4.2	Dissipation in Membranes	31
2.5	Summary	40
3	Optical Detection of Nanomechanical Motion	42
3.1	Optical Interferometry	43
3.1.1	Michelson Interferometry	45
3.1.2	Fabry-Perot Interferometry	51
	Multi-Layer Film Theory	56
3.1.3	Review of Previous Work Using a Cavity to Detect Nanomechanical Motion	60
	High-Finesse Cavities Used in the Detection of Mechanical Motion	60
	Low-Finesse Cavities Used in the Detection of Mechanical Motion	62
3.2	Design Decisions Based on Previous Work	72
3.3	Summary	73
4	Device Design and Fabrication	74
4.1	Lithographic Techniques	75
4.2	Substrate	77
4.3	Optical Mask Design	78
4.3.1	Optical Mask Processing Steps	80
4.4	Location Markers	81
4.4.1	Location Marker Processing Steps	82
4.5	Nanomechanical Device Fabrication	84
4.5.1	Membranes	84

Membrane Thickness Measurements	89
4.5.2 Torsional Resonators	93
Direct Fabrication of Torsional Resonators	94
Indirect Fabrication of Torsional Resonators via an Intermediate Membrane Step	95
Comparison of Torsional Resonator Fabrication Methods	97
4.6 Summary	99
5 Experimental Setup	102
5.1 Operating Principle	102
5.2 Low Temperature Considerations	104
5.2.1 Wiring Considerations	106
High Frequency Wiring	107
Low Frequency Wiring	108
Stage Control Wiring	108
5.2.2 Material Selection	108
5.3 Room Temperature Optical Arrangement	109
5.3.1 Optical Source	109
5.3.2 Fibre Coupler	110
5.3.3 Fibre Directional Coupler	110
5.3.4 Photomultiplier Tube	110
Photomultiplier Tube IV Converter	111
5.3.5 Photodiode	113
5.4 Low Temperature Optical Assembly	113
5.4.1 Fibre Chuck	115
5.4.2 Collimating Lens Mount	115
5.4.3 Focussing Lens Mount	116
Cover Slip	116
5.4.4 Nano Positioning Stage Assembly	118

5.4.5	Sample Holder	120
5.5	Measurement Techniques	122
5.5.1	Confocal Imaging	122
	Stage Control	123
	Scan Patterns	124
	Confocal Imaging of Silicon Nitride Nanomechanical Devices	126
5.5.2	RF Measurement Techniques	132
	Frequency Domain Analysis	132
	Time Domain Analysis	135
5.6	Sensitivity Calibration Using a Quartz Tuning Fork	138
5.6.1	Optical Measurements of a Quartz Tuning Fork	140
	Sensitivity Calibration	140
	Optical Measurements of a Quartz Tuning Fork	142
5.6.2	Comparison of Electrical and Optical Quartz Tuning Fork Measurements	143
5.7	Summary	145
6	Measurements of High-Stress Silicon Nitride Membranes	148
6.1	Frequency Dependence	148
6.2	Thermoelastic Damping	152
6.3	Inter-Membrane Coupling	158
	6.3.1 Optical Heating	160
	6.3.2 Optomechanical Forces	162
6.4	Summary	163
7	Summary and Future Work	166
7.1	Summary	166
7.2	Future Work	168
7.3	Conclusion	169

A Fabrication Recipes	170
A.1 Reactive Ion Etch Recipes	170
A.2 Alignment Mark Metallization	170
A.3 Location Marker Definition	172
A.4 Nanomechanical Device Fabrication	173
A.4.1 Membranes	173
A.4.2 Direct Fabrication of Torsional Resonators	174
A.4.3 Indirect Fabrication of Torsional Resonators using a Membrane . .	175

List of Symbols

Symbol	Quantity	Units
a	Thermal Diffusivity	m^2s^{-1}
α	Coefficient of Thermal Expansion	K^{-1}
c	Speed of Sound	ms^{-1}
C_v	Volumetric Specific Heat Capacity	$\text{Jm}^{-3}\text{K}^{-1}$
E	Young's Modulus	Pa
ϵ	Strain	-
\mathcal{F}	Finesse	-
k	Spring Constant	Nm^{-1}
κ_{th}	Thermal Conductivity	$\text{Wm}^{-1}\text{K}^{-1}$
ν	Poisson's Ratio	-
ρ	Density	kgm^{-3}
r, t	Reflection and Transmission Coefficients	-
R, T	Reflectance and Transmittance	-
σ	Tensile Stress	Pa

Chapter 1

Introduction

Research, over the last few decades, has led to the development of commercially available microelectromechanical systems (MEMS) that are used as sensors in a range of applications. With recent advances in nanofabrication techniques the sizes of these devices can be decreased, with a new class of nanoelectromechanical systems (NEMS) emerging.

The reduced dimensions of these mechanical devices, with cross sectional areas of less than $1\ \mu\text{m}^2$, and resonant frequencies ranging from several MHz well into the GHz range have attracted a great deal of interest in recent years. The reduced mass of these nanomechanical systems and quality (Q) factors in the range $10^3 - 10^5$ make them ideally suited for use as highly sensitive detectors in a range of physical systems, such as mass sensing [1, 2], force detection [3, 4], and spin detection [5].

1.1 Dissipation

An external force acting upon a nanomechanical resonator will damp the resonator, shifting the resonant frequency. The dissipation, (Q^{-1}) of the resonator places a lower limit on how small a frequency shift it is possible to measure; a larger dissipation results in an increased line width, obscuring any frequency shift. The improvement in Q-factor also reduces the power required to operate these devices.

Nanomechanical devices also have applications in the observation of quantum behaviour in mesoscopic structures. A typical nanomechanical resonator would have many more (10^{10}) degrees of freedom when compared to a collection of several atoms and if one were able to cool these devices sufficiently then it should be possible to observe quantum mechanical behaviour in these larger systems. In order to attain a quantum state the resonator would need to be cooled such that the thermal energy of the resonator was less than the energy of the lowest eigenmode [6]:

$$k_B T \leq \hbar \omega \quad (1.1)$$

which for a GHz nanomechanical resonator with resonant frequency, $\omega = 2\pi \times 10^9$ would correspond to a device temperature of $T \sim 50$ mK, something easily achieved with current dilution refrigerators. Unfortunately cooling the device is only half the challenge, as in order to prepare the resonator in a quantum state the device must also be sufficiently isolated from the surrounding environment, *i.e.* minimal dissipation. These challenges were overcome in 2009 when O'Connell *et al.* managed to successfully cool a dilational resonator into the quantum ground state and couple it to a qubit [7].

To these ends the study of dissipation in a range of nanomechanical structures has received a lot of attention in the last decade. Figure 1.1 shows quality factors measured for a range of nanomechanical systems fabricated from a variety of materials and measured at a range of temperatures. The general trend shows that as the volume of the devices decreases so too does the quality factor. This suggests that as device size decreases there is a change in the dominant dissipation mechanisms.

As devices decrease in size there is an increase in the surface to volume ratio which could result in increased contributions to the dissipation by surface effects and tunnelling two-level systems within the device. In order to improve the device sensitivity for use as sensors and the study of quantum mechanical behaviour the dissipation mechanisms at work must be understood and as far as possible minimised.

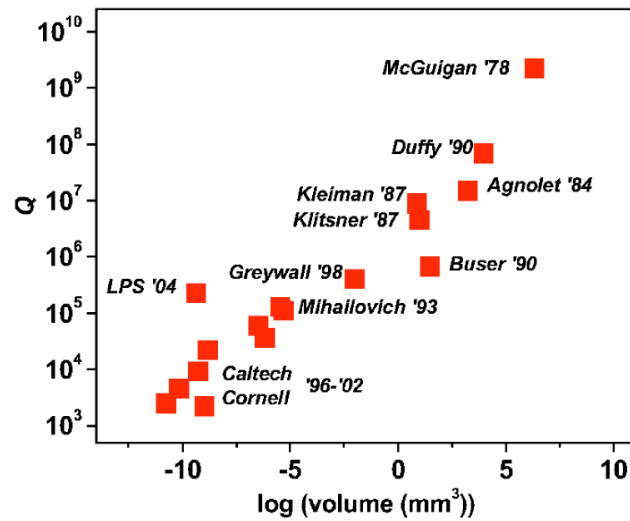


Figure 1.1: Survey of previous work on dissipation in nanomechanical systems. The measurements shown are for resonators made from a range of materials measured using a variety of different methods and at a range of temperatures. Figure reproduced from [8].

1.2 Nanomechanical Displacement Detection Techniques

As the dimensions of a mechanical resonator decrease there is a corresponding increase in the device resonant frequency, which can range from a few MHz to several GHz. The combination of increasing resonant frequency and decreasing displacement amplitudes means that detection schemes for NEMS must be ultra sensitive and those that worked well in the MEMS regime may now struggle to detect motion.

In order to successfully detect nanomechanical motion a transduction and detection scheme is required. The input should couple strongly to the device which in turn should couple strongly to the output port, however there should exist an orthogonality between input and output. The majority of detection schemes can be classified as electrical or optical. For an electrical detection system the resonator couples directly into an electrical circuit. This can limit (at least in part) the materials from which a resonator

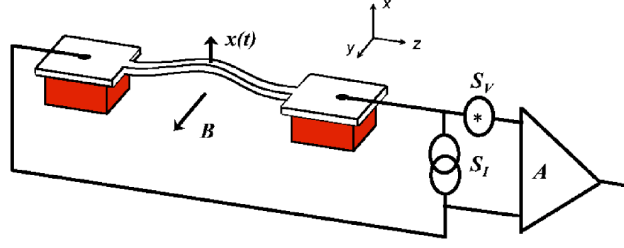


Figure 1.2: The magnetomotive detection scheme. Figure reproduced from [8].

is fabricated to those that are able to conduct electricity.

The focus of the work described in this thesis is the design and construction of a fibre interferometer to allow the optical detection of micro- and nano-mechanical motion at low temperatures. In Chapter 3 an overview of optical techniques are presented, however before that it is useful to look at other commonly used methods in the detection of nanomechanical motion.

1.2.1 Magnetomotive Actuation and Detection

One of the most commonly used detection schemes that has scaled well from MEMS to NEMS is magnetomotive detection, the arrangement of which is shown in figure 1.2 [8, 9]. An alternating current passed through a conductive loop, typically a doubly clamped beam, positioned in a static magnetic field, B will experience a Lorentz force perpendicular to both the static field and the flow of current. The resulting movement of the resonator through the static field produces an EMF across the device that can be measured. This induced emf, V_{EMF} is:

$$V_{EMF}(t) = \xi l B \frac{dx(t)}{dt} \quad (1.2)$$

where B is the size of the static field with l and x the length and displacement of the beam respectively. The constant ξ is a geometric factor quantifying the area swept out, and consequently the flux cut by the motion of the beam [10]. With V_{EMF} proportional

to the amount of flux that is cut by the beam this limits the detectable modes to odd harmonics (where the total area swept by the resonator does not equal zero). This finite flux requirement also limits the geometry of devices that can be measured using this technique to doubly clamped beams.

The motion of the mechanical element in the static magnetic field causes a damping of the resonator that results in a lower Q-factor referred to as the loaded-Q. In order to generate V_{EMF} a current, I , which is proportional to B , must be induced within the beam. Resistive losses within the beam, with resistance R , are equal to I^2R resulting in a loaded-Q that varies as B^2 .

The magnetomotive technique has been used successfully to detect nanomechanical motion at frequencies up to a GHz with a sensitivity of $2 \times 10^{-15} \text{ m}/\sqrt{\text{Hz}}$ (for a resonator of frequency 116 MHz) [11]. While the magnetomotive scheme has shown itself to be a highly sensitive method for measuring displacements in nanomechanical systems, it does suffer from some drawbacks. The large magnetic fields needed to actuate and detect the motion of the device requires cryogenic temperatures and superconducting solenoids. The ability of a current to flow through the mechanical device restricts the materials that can be studied using this technique to conductors (or at the very least a nanomechanical device containing a conductive element). Detection is also limited to odd modes, where the geometric factor $\xi \neq 0$. As the harmonic of the resonator increases there is a decrease in the ability of the system to detect the motion of these modes as the amount of flux cut by the current loop decreases.

1.2.2 Capacitive Detection

In this technique a capacitor is formed between the mechanical element and a ground electrode. As the resonator is actuated there is a variation in plate separation and consequently capacitance. The dynamic capacitance changes observed will generally be of order 10^{-18} F and in order to detect such small changes measurements are often made using balanced bridge arrangements [12], impedance matching the measurement circuits to the resonator [13] or fabricating the NEMS directly into a resonant circuit .

In work by Truitt *et al.* [13], a gate $\sim 2 \mu\text{m}$ in length separated from the resonator by $\sim 100 \text{ nm}$ was used. In this arrangement the static capacitance will be $\sim 10^{-17} \text{ F}$ (giving an impedance of $10^8 - 10^9 \Omega$ for $\omega_0 = 10 - 100 \text{ MHz}$), with nanoscale flexural motion of the beam changing the capacitance by $\sim 10^{-19} \text{ F}$. A signal this small will be lost in the parasitic capacitance of the measurement electronics, degrading both signal and bandwidth. If a voltage, V_g , is applied to the gate the resonator becomes part of an LCR circuit, and will describe the behaviour of a 1D simple harmonic oscillator. In this case the impedance of the resonator is matched to that of the detection electronics, allowing measurements of the nanomechanical motion to be made [13].

For simplicity the majority of capacitive detection schemes detect in-plane nanomechanical motion, as from a fabrication point of view it is easier to form a gate next to, as opposed to below, the resonator. Given the magnitude of the dynamic capacitances that are detected it is often simpler to actuate the resonator electrostatically using the same arrangement while detecting the mechanical motion using an optical technique. An ac drive voltage with dc bias is applied to the resonator resulting in motion of the beam. The main drawback of a capacitive transduction scheme is that for a system with only one set of electrodes it can only be used to drive or detect the motion.

The limitations of capacitive detection lie in the geometric requirements. As device dimensions decrease so too does the area that is able to form the plates of the capacitor. This decrease in capacitance can to a certain extent be overcome by placing the gate electrode closer to the mechanical element, although this then introduces additional complexities to the fabrication as it becomes technically challenging to position a gate close enough. While capacitive detection has proved invaluable in MEMS it does not scale well into NEMS and is often used to electrostatically actuate devices the motion of which is then detected optically [14–16].

Gradient Field Transduction

In an electrostatic actuation scheme a capacitor is formed between a gate and the mechanical element, requiring that the resonator be conductive. Unterreithmeier *et al.*

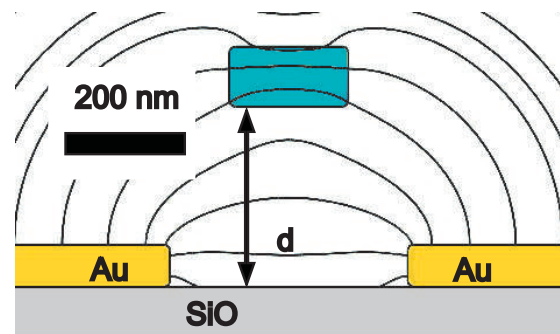


Figure 1.3: Schematic illustrating lines of constant potential produced by the electrodes as part of the gradient field technique. The dielectric element (blue) placed within this field will experience a dipolar moment and will be attracted to regions where the gradient of the electric field is largest. Figure reproduced from [17].

[17, 18] modified this scheme to allow both the actuation and detection of nanomechanical motion in dielectric resonators. The arrangement employed is shown in figure 1.3.

Two electrodes deposited on the substrate are biased with a dc voltage (V_{dc}) to generate the non-uniform electric field shown in figure 1.3. A dielectric element placed within this electric field will experience a dipolar moment that will be attracted towards regions within the E-field with a larger gradient. Modulating the dc voltage with an ac signal (V_{ac}) causes these regions to shift and the resonator to be driven.

The gradient field technique can also be used to detect motion. For this two pairs of electrodes are used; one pair to actuate, while the second monitors the motion. As the resonator moves in the electric field the capacitance is modulated and a charge generated which is monitored using an IV converter placed near the sample. Using this dielectric detection scheme the ultimate sensitivity of this system is estimated at $20 \text{ pm}/\sqrt{\text{Hz}}$ [17].

1.2.3 Optical Detection

The majority of electrical detection schemes place requirements on the material from which the resonator is fabricated. Optical detection uses an optical spot to monitor the motion of the resonator, this allows the material requirements to be relaxed and allows the study of purely dielectric materials (such as silicon nitride).

In micromechanical systems motion can be detected in two ways using beam deflection or interferometry. In beam deflection, which is normally used to detect the deflection of an AFM cantilever, an optical spot is focussed onto the tip of a cantilever and the deflection of this beam caused by the motion of the cantilever is measured. In interferometry a coherent laser beam is used to probe the resonator, and variations in the intensity of the reflected light are monitored. Beam deflection is ideally suited for a micromechanical system, where deflections are “large” (on the order of the wavelength) and as such the distance over which the beam is deflected is large enough to be measured; interferometry on the other hand will struggle when the deflections are larger than $\lambda/4$ and the periodicity of the interference makes it difficult to determine the displacement of the resonator [19].

As device dimensions decrease, so too does the amplitude of the mechanical motion and as a result the majority of optical measurements of nanomechanical displacements are made using interferometric techniques, and it is these methods that will be focussed on in this thesis.

1.3 Outline of Thesis

The aim of this thesis is to outline the design and construction of a fibre based interferometer capable of detecting nanomechanical motion to temperatures less than 1 K. In recent years much work has been done on the study of dissipation in dielectrics as they have shown far higher quality factors than metals. The majority of nanomechanical detection schemes rely on an electrical measurement and in the majority of cases requires the devices be made (at least in part) from a metal. Optical detection schemes

eliminate the requirement that the resonator contain a metallic element, allowing the measurement of purely dielectric devices.

Previous measurements carried out in Nottingham on low temperature dissipation in doubly clamped beams of high stress silicon nitride [20, 21] saw quality factors in excess of 10^6 and a temperature dependent dissipation. These measurements were carried out using a magnetomotive detection scheme that required a thin layer of gold to be deposited upon the dielectric, altering the physical properties. Optical detection does not have these requirements and would allow measurements of purely dielectric devices to be made, complementing the nanomechanical measurement techniques already available to the NEMS group of Nottingham University.

In addition to the design and construction of the fibre interferometer a range of nanofabrication processes for high-stress silicon nitride were developed to fabricate nanomechanical devices with high quality factors. In addition to flexural structures (including membranes and doubly clamped beams), torsional resonators were also fabricated from high-stress silicon nitride. It is hoped that these high-stress torsional resonators could display significantly higher quality factors than their low-stress counterparts.

Chapter 2 provides an overview of nanomechanical systems, focussing on the mechanics of resonant systems and how the resonant frequencies of nanomechanical membranes and torsional resonators are calculated. The most common dissipation mechanisms affecting nanomechanical resonators are then introduced with a review of recent dissipation studies in high-stress silicon nitride.

Having introduced nanomechanical systems, Chapter 3 will present the working principle behind several of the optical detection schemes commonly used in the detection of their motion. Multi-layer film theory is also introduced and used to calculate the film thicknesses required in a substrate suitable for use with the experimental setup. Current work into optical detection of nanomechanical motion is then reviewed and decisions made regarding the design and construction of the fibre interferometer outlined.

Chapter 4 outlines the fabrication of nanomechanical systems, introducing the nanofabrication techniques that are used before giving an in-depth discussion of the fabrication

of high-stress silicon nitride membranes and torsional resonators. More detail on these fabrication recipes including in-depth processing parameters are included in Appendix A.

The experimental setup designed and constructed during this work is outlined in Chapter 5, including design considerations and the interfacing of the fibre interferometer with a commercial dilution refrigerator. A range of measurements on micro- and nanomechanical devices are then presented to demonstrate the modes of operation of the interferometer, including measurements on a quartz tuning fork used to calibrate the response of the interferometer.

Chapter 6 presents measurements of high-stress silicon nitride membranes at both room temperature and low temperature and explores several of the dissipation mechanisms at work. In Chapter 7 we summarise the thesis and outline possible future work.

Chapter 2

Nanomechanical Systems

In this chapter the mechanics of resonant systems are presented. In the linear response regime the nanomechanical resonator behaves as a harmonic oscillator, so in the first part of this chapter an overview of harmonic oscillators is presented. We will then move on to look at the vibrational modes of two nanomechanical devices discussed in this work, the torsional resonator and the stressed membrane. Having introduced several common nanomechanical structures the dissipation mechanisms that can affect their operation are described before reviewing previous work on dissipation in nanomechanical systems.

2.1 Mechanics of Resonant Systems

Mechanical resonant systems are simple harmonic oscillators that can be modelled as systems composed of a mass, m , and a spring of constant, k . If we displace the mass from rest by a distance x the spring exerts a restoring force, $F = -kx$. In the linear regime this restoring force is proportional to the displacement and the system will behave as a simple harmonic oscillator with the mass oscillating about the rest position with resonant frequency $\omega_0 = \sqrt{\frac{k}{m}}$. The equation of motion for an undriven simple harmonic oscillator is [20, 22–24]:

$$m\ddot{x}(t) + kx(t) = 0 \tag{2.1}$$

Once in motion the undamped system will continue to oscillate indefinitely, a more realistic description is that of the damped driven harmonic oscillator. The damping term is dependent on the velocity of the resonator, and proportional to the damping coefficient, γ . For a resonator driven by a sinusoidal force of magnitude F_d at frequency ω_d the equation of motion becomes:

$$\begin{aligned} m\ddot{x}(t) + m\gamma\dot{x}(t) + kx(t) &= F_d e^{i\omega_d t} \\ \ddot{x}(t) + \gamma\dot{x}(t) + \omega_0^2 x(t) &= \frac{F_d e^{i\omega_d t}}{m} \end{aligned} \quad (2.2)$$

which we first solve for the undriven case, *i.e.* $F_d = 0$, using the initial solution $x(t) = \Re[x_0 e^{i\omega t}]$ which allows the equation to be reduced to $-\omega^2 + i\gamma\omega + \omega_0^2 = 0$, of which the roots are:

$$\omega_{\pm} = i\frac{\gamma}{2} \pm \sqrt{1 - \frac{\gamma^2}{4\omega_0^2}} \quad (2.3)$$

For a system with small damping the quality factor is defined as $Q = \frac{\omega_0}{\gamma}$, which allows the solution for the displacement of the system to be rewritten as:

$$x(t) = \Re[x_0 e^{i\omega_0 t/2Q} (e^{\pm i\omega'_0 t})] = x_0 e^{i\omega_0 t/2Q} \cos(\omega'_0 t) \quad (2.4)$$

where the damped resonant frequency, ω'_0 , is related to the undamped frequency via:

$$\omega'_0 = \omega_0 \sqrt{1 - \frac{1}{4Q^2}} \quad (2.5)$$

The quality factor is the ability of a mechanical system to store energy. For an underdamped system where $Q \gg 1$ the system approximates to a simple harmonic oscillator, with $\omega'_0 \approx \omega_0$. An overdamped system ($Q \approx 1$) has a resonant frequency that will be lower than for the undamped case, with an amplitude of oscillation that decreases rapidly over several cycles once the driving force is removed. The time taken for the system to damp to $1/e$ of the initial amplitude is known as the damping time, τ , related to the damping by $\tau = 2/\gamma$. In the case of small damping, where $\gamma \ll \omega_0$, the quality factor can be approximated by $Q = \omega_0/\gamma = \omega_0\tau/2$ [20, 22, 24].

Having solved the system in the absence of a driving force ($F_d = 0$) we now look at the behaviour of the system under the influence of a driving force ($F_d \neq 0$). In this case the solution of equation 2.2 is composed of two parts, a transient response (equation 2.4) and a steady state solution for the system (with motion at frequency ω_d). For time scales longer than the damping time, τ , the solution will be a sinusoidal displacement at ω_d . This results in a steady state solution of the form $\Re[Re^{i\omega_d t}]$, with amplitude, R , found using the transfer function [23]:

$$R = \frac{F_d/m}{(\omega_0^2 - \omega_d^2) + \frac{i\omega_0\omega_d}{Q}} \quad (2.6)$$

which can be written in the form $R = R_0 e^{-i\phi}$, with amplitude R_0 and phase angle ϕ , with:

$$R_0(\omega_d) = \frac{F_d/m}{\sqrt{(\omega_0^2 - \omega_d^2)^2 + \frac{\omega_0^2\omega_d^2}{Q^2}}} \quad (2.7)$$

and

$$\phi(\omega_d) = \begin{cases} \arctan\left(\frac{\omega_0\omega_d}{Q(\omega_0^2 - \omega_d^2)}\right) & \text{for } \omega_d \leq \omega_0 \\ \pi + \arctan\left(\frac{\omega_0\omega_d}{Q(\omega_0^2 - \omega_d^2)}\right) & \text{for } \omega_d > \omega_0 \end{cases} \quad (2.8)$$

From which we see that on resonance ($\omega_d = \omega_0$) the amplitude of oscillation is equal to $QF_d/m\omega_0^2$, with displacement proportional to quality factor. The frequency response takes the form of a Lorentzian, with a peak centred at ω_0 . A plot showing the amplitude and phase of a resonator as the drive frequency passes through resonance is shown in figure 2.1.

The quality factor relates to the full-width at half maximum (FWHM), $\Delta\omega$ by $Q = \omega_0/\Delta\omega$. As the drive frequency passes through ω_0 there is a phase shift of π , resulting in a phase difference of $\pi/2$ between the drive and response on resonance [20, 22–24].

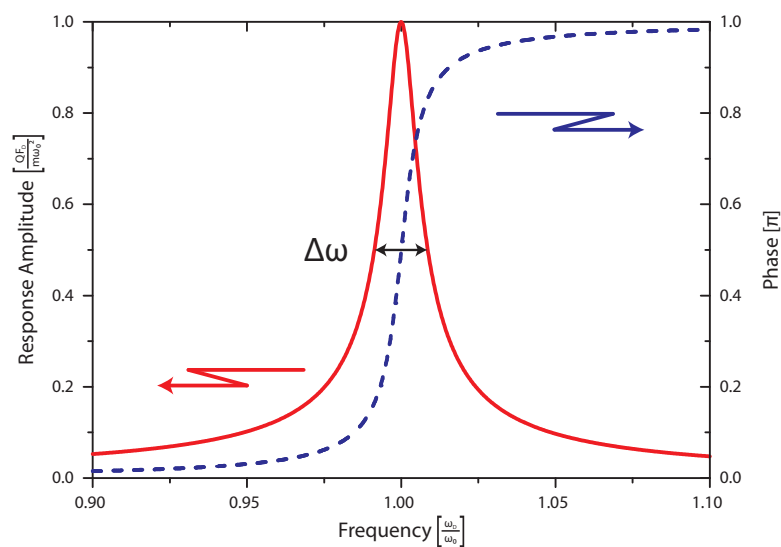


Figure 2.1: Response of a driven oscillator showing the amplitude response (red) and the phase (blue) as the drive frequency is swept through resonance.

2.2 Frequency Calculations

Nanomechanical resonators come in a range of geometries, as determined by the application for which they are intended. The focus of this work is on high-stress silicon nitride so in the following section we will introduce two of the nanomechanical structures that were fabricated from silicon nitride. Given that the aim of this work is to detect nanomechanical motion using interferometric techniques the focus is on devices that have vibrational modes capable of producing out of plane motion.

2.2.1 Torsional Resonators

Doubly-clamped nanomechanical devices will exhibit two modes of oscillation, flexural and torsional. In a flexural mode the beam experiences a bending force, while in a torsional mode a torque is experienced, with rotation about the centre axis of the rod. For torsional modes the displacement (z) is now measured in terms of a rotation angle (θ), while the spring constant (k) and mass (m) are replaced by the torsion constant (κ)

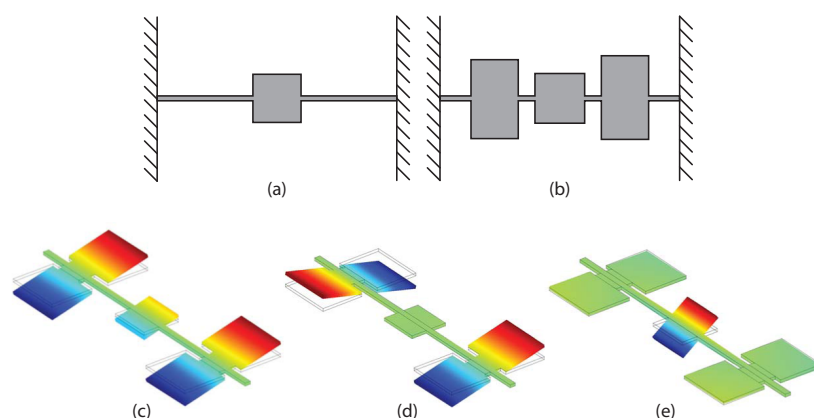


Figure 2.2: The typical device geometry of the (a) one-paddle and (b) three-paddle torsional resonators discussed in this section. Finite element models of the (c) first, (d) second and (e) third torsion mode of a three-paddle resonator. The colour scale in (c)-(e) indicates the amplitude of the z -displacement. Finite element models reproduced from [25].

and inertia (I) respectively. For this system the natural frequency becomes $\omega_0 = \sqrt{\kappa/I}$ [22].

For a bar of constant rectangular cross section (width w , thickness t) and length l the torsional constant is:

$$\kappa = \frac{\beta w t^3 E}{2l(1 + \nu)} \quad (2.9)$$

where β is a geometric factor (~ 0.2), E the Young's modulus and ν the Poisson ration. As the torsion rod dimensions decrease so too does κ , leading to an increase in the angle of rotation, θ , observed for an applied torque. The out-of plane displacement due to an angle θ applied to a beam of width w is $z = w\theta/2$, so in order to increase the magnitude of z it is common to include one or more paddles in the design [22, 25]. In this section we introduce two classes of torsional resonator: one-paddle and three-paddle types, the geometry for which is shown in figures 2.2(a) and (b) respectively.

A one-paddle torsional resonator has only one torsional mode, in which the central paddle rotates about the central torsion beam. A three-paddle torsional resonator however has three unique torsional modes for which finite element models (in order of increasing frequency) are shown in figures 2.2(c)-(e). The lowest frequency mode (figure 2.2(c)) has all three paddles rotating in-phase, in the second mode (figure 2.2(d)) the outer paddles oscillate out of phase with one another while the central paddle is stationary and for mode three (figure 2.2(e)) only the smaller central paddle is in motion.

The inhomogeneous cross section of these resonators complicates finding an expression for the torsional frequencies. As such a numerical technique known as Finite Element Modelling (FEM) is often employed to solve the wave equation numerically. This breaks the structure broken down into a mesh composed of smaller subdomains. The FEM solver (a package such as COMSOL) then finds a solution to the governing equation for each of these subdomains which are then combined by ensuring continuity at the boundaries between domains to give a solution for the complete system [26].

An example of nanoscale torsional resonators are those fabricated by Davis *et al.* [25, 27] where a three-paddle nanotorsional resonator was fabricated to allow the magnetic properties of nanoscale magnetic elements to be studied. Resonators were fabricated from commercially available low-stress silicon nitride membranes using focussed-ion-beam milling. Patterning the resonator with a permalloy film allowed the resonator to be actuated using a magnetic field and the amplitude of oscillation monitored. The torque constant of these devices was found to be $\sim 10^8 \mu_B$, 3 orders of magnitude lower than previous torque magnetometers.

The frequency responses of the first (3.35 MHz) and third (21.05 MHz) torsional modes of a nanotorsional resonator actuated magnetically are shown in figure 2.3(a) and (b). The resonator is coated with a 10 nm thick layer of permalloy that in the presence of an external magnetic field will produce a torque on the resonator. The first mode demonstrates a reduced Q (Q=800) when compared to the third mode (Q=2000), where the stationary outer paddles are able to act as counterweights, isolating the central

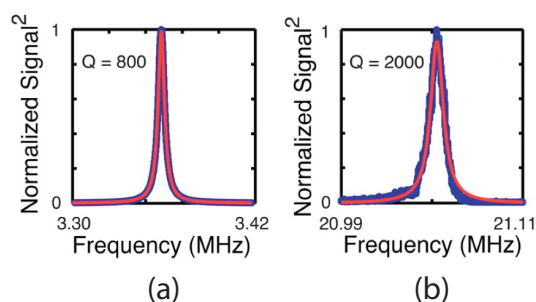


Figure 2.3: Frequency responses of the (a) first and (b) third torsion modes of a three paddle torsional resonator that is actuated magnetically. Figures reproduced from [25].

paddle from the supporting structure and minimizing energy loss.

In the work of Davis *et al.* [25, 27] the resonators studied are fabricated from low-stress silicon nitride as their fabrication techniques are not compatible with high-stress silicon nitride. In Chapter 4 a method for fabricating torsional resonators from high-stress silicon nitride will be presented. High-stress silicon nitride increases the mechanical stability of the device along with the ability to store energy. This may be of interest for the third torsion mode of a three paddle resonator as the increased mechanical stability and ability to store energy coupled to the isolation of the central paddle from the supporting structure may lead to an increased quality factor in this torsional mode.

2.2.2 Membranes

Membranes are thin sheets clamped around their perimeter that resonate in the out of plane direction. The two-dimensional nature of these structures requires that two modal numbers be used to describe the shape and frequency of the membrane vibrational modes. In order to predict the resonant frequency of these membrane it is necessary to solve the wave equation [26]:

$$\frac{\partial^2 z}{\partial t^2} - c^2 \nabla^2 z = 0 \quad (2.10)$$

where z is a function that describes the displacement of the device and the speed of

sound in the membrane is $c = \sqrt{T/\mu}$, where T is the tension per unit length and μ is the mass per unit length or area [26].

In solving the wave equation it is important that a suitable coordinate system be chosen for the membrane geometry. A rectangular membrane lends itself to a cartesian description of the form, $z(x, y, t)$, while a circular membrane is better described using a polar system of coordinates, $z(r, \theta, t)$. For a membrane of thickness h , density ρ , and initial stress σ the tension per unit length and mass per unit area are $T = \sigma h$ and $\mu = \rho h$ respectively.

Rectangular Membrane

Let us first consider the case of a rectangular membrane with sides of length a and b in the x and y directions respectively. In cartesian coordinates equation 2.10 becomes:

$$\frac{\partial^2 z}{\partial t^2} - c^2 \left(\frac{\partial^2 z}{\partial x^2} + \frac{\partial^2 z}{\partial y^2} \right) = 0 \quad (2.11)$$

To solve the wave equation boundary conditions are required, which for a rectangular membrane fixed around the perimeter are [26]:

$$z(0, y, t) = z(a, y, t) = z(x, 0, t) = z(x, b, t) = 0 \quad (2.12)$$

The general solution ($z(x, y, t)$) needs to not only satisfy these boundary conditions, but also be separable, with spatial (Z) and temporal $e^{i\omega t}$ components, $z(x, y, t) = Z(x, y)e^{i\omega t}$, which when substituted into the wave equation yields the Helmholtz equation:

$$\frac{\partial^2 Z}{\partial y^2} + \frac{\partial^2 Z}{\partial x^2} - \frac{\omega^2}{c^2} Z = 0 \quad (2.13)$$

with general solution:

$$\begin{aligned} Z(x, y) = & A_1 \cos(\alpha x) \cos(\beta y) + A_2 \cos(\alpha x) \sin(\beta y) + \\ & A_3 \sin(\alpha x) \cos(\beta y) + A_4 \sin(\alpha x) \sin(\beta y) \end{aligned} \quad (2.14)$$

Making use of the boundary conditions allows an expression for the $(n, m)^{th}$ mode of a rectangular membrane to be obtained [26]:

$$Z(x, y) = A_4 \sin(\alpha x) \sin(\beta y) \quad (2.15)$$

where:

$$\alpha = \frac{m\pi}{a} \quad \text{and} \quad \beta = \frac{n\pi}{b} \quad (2.16)$$

The first 9 modes of a square membrane are shown in figure 2.4, along with the node structure from which it can be seen that within the membrane there are $n - 1$ and $m - 1$ nodal lines lying within the membrane.

Inserting Z into equation 2.13 also yields an expression for the eigenfrequencies:

$$\omega_{n,m} = \pi c \sqrt{\frac{m^2}{a^2} + \frac{n^2}{b^2}} \quad (2.17)$$

which for a square ($a = b$) membrane shows a frequency that is proportional to $\sqrt{m^2 + n^2}$ [26].

Circular Membrane

The wave equation for a circular membrane of radius a described using polar coordinates, with a solution of the form $z(r, \phi, t)$ is:

$$\frac{\partial^2 z}{\partial t^2} - c^2 \left(\frac{\partial^2 z}{\partial r^2} + \frac{1}{r} \frac{\partial z}{\partial r} + \frac{1}{r^2} \frac{\partial^2 z}{\partial \phi^2} \right) = 0 \quad (2.18)$$

As before the displacement around the edge of the membrane must be equal to zero, *i.e.* $z(a, \phi, t) = 0$. The symmetry of the system means that only one boundary condition can be defined in this way. A second boundary condition arises from the fact that the displacement at all points of the membrane must be finite [26].

A separable solution, $z(r, \phi, t) = W(r, \phi)e^{i\omega t}$ is used which when substituted into the wave equation yields:

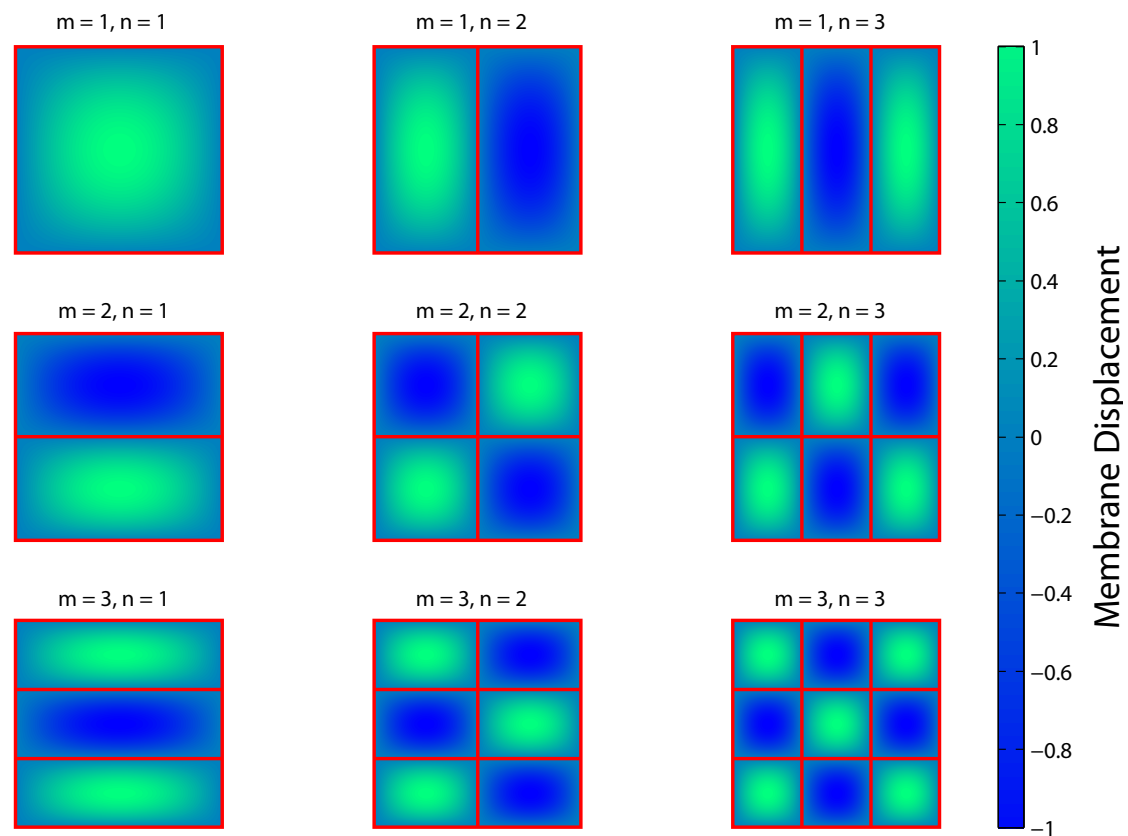


Figure 2.4: Mode shapes of the first 9 modes of a rectangular membrane. The displacement, z , of each mode has been scaled to lie in the range $-1 \leq z \leq 1$, and the red lines indicate the positions of the nodal lines within the membrane.

$$W + \frac{c^2}{\omega^2} \left(\frac{\partial^2 W}{\partial r^2} + \frac{1}{r} \frac{\partial W}{\partial r} + \frac{1}{r^2} \frac{\partial^2 W}{\partial \phi^2} \right) = 0 \quad (2.19)$$

A solution for the spatial component, W , is required that should be separable into radial ($\Phi(\phi)$) and azimuthal components ($R(r)$) of the form $W(r, \phi) = R(r)\Phi(\phi)$. When this is substituted we are left with:

$$\frac{\omega^2}{c^2} + \left(\frac{1}{R} \frac{\partial^2 R}{\partial r^2} + \frac{1}{rR} \frac{\partial R}{\partial r} + \frac{1}{r^2 \Phi} \frac{\partial^2 \Phi}{\partial \phi^2} \right) = 0 \quad (2.20)$$

the circular, periodic nature of the membrane allows a solution for Φ to be written as $\Phi(\phi) = e^{im\phi}$, which when inserted into the wave equation (and substituting $\gamma = \omega/c$) results in the Bessel differential equation:

$$\frac{\partial^2 R}{\partial r^2} + \frac{1}{r} \frac{\partial R}{\partial r} + R \left(\gamma^2 - \frac{m^2}{r^2} \right) = 0 \quad (2.21)$$

for which the solution is:

$$R(r) = DJ_n(\gamma r) + EY_n(\gamma r) \quad (2.22)$$

where D and E are constants of integration and J_n and Y_n are Bessel functions (of order n) of the 1st and 2nd kinds respectively. The symmetry of the Bessel functions, $J_n = J_{-n}$ and $Y_n = Y_{-n}$ means we need only consider solutions where $n = 0, 1, 2, \dots$. We are also able to ignore the Bessel functions of the 2nd kind as Y_n has a logarithmic singularity at $r = 0$ and we require that the displacement of the membrane be finite at all points. As such we set the constant of integration, E to zero, which yields a solution for the azimuthal component of the form [26]:

$$R(r) = D_{n,m} J_n(\gamma r) \quad (2.23)$$

In order to satisfy the boundary condition $R(a) = 0$, the m^{th} root of the Bessel function must lie on the boundary of the membrane and we define a scaling factor for the radial component of $\zeta_{n,m} = \omega_{n,m}a/c$ where $\zeta_{n,m}$ is the m^{th} root of the n^{th} Bessel

function of the 1st kind [26]. Rearranging this gives an expression for the eigenfrequency of the $(n, m)^{th}$ mode of a circular membrane of radius a :

$$\omega_{n,m} = \frac{\zeta_{n,m}c}{a} \quad (2.24)$$

This scaling also determines the mode shape of the membrane. Earlier we introduced the constant $\gamma = \omega/c$, which using equation 2.24 can be rewritten as $\gamma = \zeta_{n,m}/a$, which allows an expression for the mode shape of a circular membrane to be written as:

$$\begin{aligned} W(r, \phi) &= D_{n,m} J_n(\gamma r) e^{in\phi} \\ &= D_{n,m} J_n\left(\frac{\zeta_{n,m}r}{a}\right) e^{in\phi} \end{aligned} \quad (2.25)$$

with $J_n(\gamma r)$ describing the azimuthal and $e^{in\phi}$ the radial profile, with $n = 0, 1, 2, \dots$ and $m = 1, 2, 3, \dots$. The first nine mode shapes for a circular membrane are shown in figure 2.5.

In figure 2.5 we see the effect of the mode number on the mode shape. The number of azimuthal node lines is controlled by the index m , which must take a positive value greater than or equal to 1. As this increases, so too does the number of radial node lines, whose locations are defined by the roots of the Bessel function of the 1st kind. The location of the azimuthal lines are described by index n which takes an integer value (that can include 0).

2.3 Dissipation in Nanomechanical Devices

In the earlier discussion on the behaviour of a driven harmonic oscillator (section 2.1) we introduced the quality factor, a measure of a mechanical systems ability to store energy. The dissipation is the inverse of the quality factor ($1/Q$) and is a measure of the rate at which the resonator loses energy. It can be defined as the ratio between the energy lost per cycle (ΔU) and the energy within the system (U):

$$\frac{1}{Q} = \frac{1}{2\pi} \frac{\Delta U}{U} \quad (2.26)$$

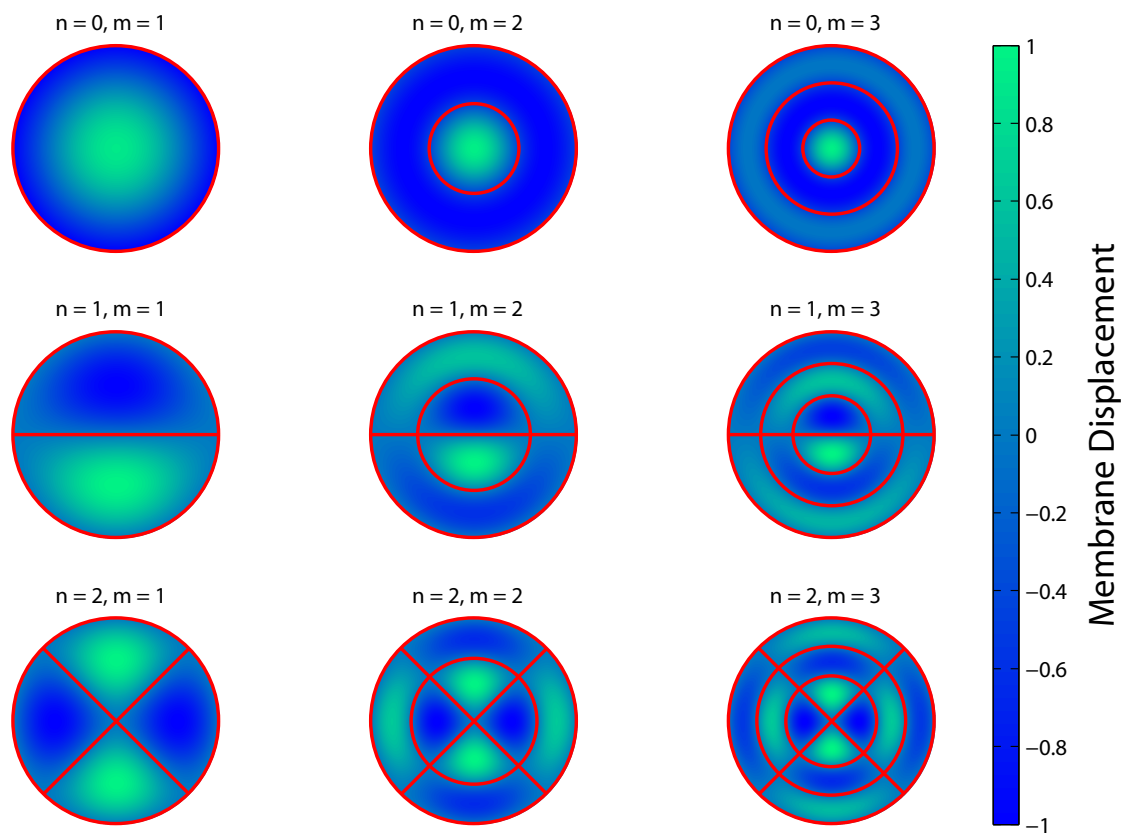


Figure 2.5: Mode shapes of the first 9 modes of a circular membrane. The displacement, z , of each mode has been scaled to lie in the range $-1 \leq z \leq 1$, and the red lines indicate the positions of the nodal lines within the membrane.

Dissipation mechanisms within a mechanical device can be classified as either intrinsic (caused by processes within the structure) or extrinsic (due to the interaction of the resonator with its surroundings). For a resonator subject to several damping mechanisms (i, j, k, \dots) the overall dissipation in the system is the sum of the dissipation due to the individual components ($Q_i^{-1}, Q_j^{-1}, Q_k^{-1}, \dots$):

$$\frac{1}{Q} = \frac{1}{Q_i} + \frac{1}{Q_j} + \frac{1}{Q_k} + \dots \quad (2.27)$$

In the following sections the main dissipation mechanisms in nanomechanical systems are introduced.

2.3.1 Extrinsic Mechanisms

Extrinsic losses arise from the interaction of a resonator with the surrounding environment. As the mechanical device is losing energy directly to its surroundings it is often possible to control and reduce the amount of energy dissipated.

Gas Damping

For a resonator oscillating in an atmosphere of gas molecules energy will be lost through collisions with individual molecules. The type of gas damping that occurs is controlled by the pressure of gas present. The *molecular* regime is observed in a low pressure environment where the mean-free path of a gas molecule is far larger than the device dimensions. In this case the energy lost through gas collisions is given by:

$$\frac{1}{Q_{gas}} = \frac{pA}{m_{eff}\omega_0 v} \quad (2.28)$$

where p is the pressure around the resonator, A and m_{eff} are the surface area and effective mass of the resonator respectively, and $v = \sqrt{k_B T/m}$ is the thermal velocity of the gas molecules (with mass m) [8]. As the pressure surrounding the resonator increases the damping moves from the molecular to the viscous damping regime where $Q_{gas}^{-1} \propto \sqrt{p}$.

At a low pressure the dissipation due to gas damping will vary linearly with pressure, up to a crossover pressure (where the mean free path of the molecules is equal to the sound wavelength in the gas) above which there is a $p^{1/2}$ dependence. To minimize the effects of gas damping experiments are normally carried out under vacuum.

Clamping Losses

Energy can be lost through acoustic waves propagating into the the substrate. For a doubly-clamped beam it has been shown that dissipation due to clamping losses is related to the length of the beam, l and the thickness, t by [28]:

$$\frac{1}{Q_{cl}} \propto \frac{t^4}{l^5} \quad (2.29)$$

from which it is clear that the dissipation in a doubly-clamped beam due to clamping losses will increase with aspect ratio (t/l), so as the frequency of a device increases so too will the dissipation due to clamping losses [28]. It is interesting to note that as clamping loss is a temperature independent process it will impose an ultimate limit on the quality factor of a resonator at low temperatures.

In membranes the energy lost into the supporting structure has been shown to be strongly influenced by mode shape. In work on rectangular and circular membranes carried out on membranes made of high-stress silicon nitride [29–31], classes of high-Q modes have been observed. The square membrane modes of index $(n, n)|_{n>1}$ and the circular membrane modes of index $(n, 1)|_{n>1}$ show increased quality factors compared to nearby modes. These high-Q modes are composed of nodes intersecting the perimeter at equally spaced points. In this configuration the equivalent segments of the membrane are able to destructively interfere, cancelling out the elastic waves that are radiated into the supporting structure thereby reducing clamping losses.

Transducer Damping

The act of measuring the nanomechanical displacements of a device will influence the motion, damping the resonator. In an optical detection scheme this damping can arise

in two ways: through heating of the resonator by the optical spot and through optical forces associated with the optical cavity acting upon the resonator (which are discussed in Chapter 3), but in order to minimize these optical effects the smallest possible optical power should be used.

2.3.2 Intrinsic Mechanisms

Intrinsic dissipation mechanisms are specific to the material from which the resonator is fabricated and as such are difficult to influence.

Thermoelastic Damping

The motion of a nanomechanical resonator will introduce temperature gradients across the resonator, and consequently there will be a flow of heat from hot to cold regions. In order to relax back to an equilibrium temperature the resonator will couple to thermal modes of the surrounding environment. This results in a temperature dependent dissipation process, the effects of which can be eliminated by carrying out measurements at low temperatures ($T < 2$ K) [20].

Surface Effects

As the dimensions of nanomechanical devices decrease there is a corresponding increase in the surface area to volume ratio of the devices along with a decrease of quality factors [8]. This suggests that losses due to surface effects caused by dangling bonds, oxide layers or water layers that are able to behave as two-level systems at low-temperatures. These losses can be reduced (but not eliminated) using surface treatments such as annealing and passivation using thiol monolayers [20].

Two-Level Systems

Two-level systems (TLS) refer to the way in which dissipation due to defects within solids are described using a double well potential [20, 22]. These defects arise from dislocations,

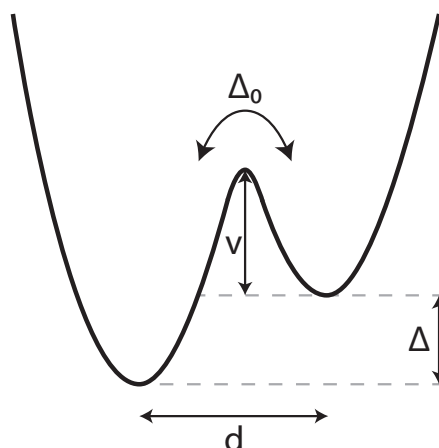


Figure 2.6: The double well potential used to describe defects in a solid at low temperatures when only the lowest energy levels are occupied. Δ is the asymmetry between two wells separated by a distance d . The barrier between the wells has height v and requires a tunnelling energy of Δ_0 to cross. At low temperatures only the lowest two eigenmodes of the wells will be occupied.

contaminants and dangling bonds and have the biggest influence on the dissipation at low temperatures, where the lowest eigenstates of the double well potential are occupied.

The double well potential is shown in figure 2.6 and is described in terms of a potential, Δ , characterising the asymmetry between the wells and the tunnelling energy, Δ_0 . In the Standard Tunnelling Model (STM) it is assumed that these TLS have a broad distribution of energies and relaxation times able to couple to their environment and lose energy [20]. This coupling occurs by either resonant or relaxation absorption. For a mechanical resonator vibrating at a frequency of ω the behaviour of the TLS will depend on the ratio of $\frac{\hbar\omega}{k_B T}$. When $\frac{\hbar\omega}{k_B T} \geq 1$ a transition from the ground to the excited state of the TLS will occur, with phonons being resonantly absorbed by TLS with the correct energy splittings.

For $\frac{\hbar\omega}{k_B T} \ll 1$ the TLS are likely to be in their ground state and the resonant absorption (and contribution to damping) should be minimal, however in a number of

measurements made in this regime a temperature dependent dissipation and frequency shift has been observed [20, 21, 32, 33]. In this regime the anelasticity of the system allows the out of phase strain field to couple to the TLS, modifying Δ or Δ_0 . In order for these TLS to relax back into equilibrium they are able to absorb and emit phonons, resulting in dissipation and a shift in the resonant frequency.

The STM has been used to analyse dissipation in a number of nanomechanical systems with varying success, however as it was developed to describe the behaviour of bulk amorphous solids it does not take into account the dimensionality present in nanomechanical devices. It also cannot differentiate between TLS present on the surface or within the bulk, it is therefore necessary to know where the TLS lie within the device.

2.4 Review of Measurements in Silicon Nitride Systems

Silicon nitride is an amorphous solid grown on silicon substrates by chemical vapor deposition. It has been widely used in micro-mechanical systems and is the material from which a large number of AFM cantilevers are fabricated. Through careful control of the deposition parameters it is possible to modify the intrinsic stress within the silicon nitride layer. This pre-stressing has led to the fabrication of a number of devices with quality factors in excess of 10^6 [29–31, 33, 34]. In the following section previous work on dissipation in mechanical systems of high-stress silicon nitride are reviewed.

2.4.1 Dissipation in Doubly-Clamped Beams

The doubly clamped beam is the simplest form of device that can be fabricated from high-stress silicon nitride. A recent study by Unterreithmeier *et al.* [35] measured the dissipation in a family of doubly clamped beams of silicon nitride with length $35/n \mu\text{m}$ (where $n = 1, \dots, 7$), width 200 nm and thickness 100 nm, an example of which are shown in figure 2.7(a). Devices were actuated using the gradient field technique (introduced in Section 1.2.2), with motion detected via optical interferometry. Harmonics with frequencies of up to 80 MHz were detected, the results of which are shown in figure

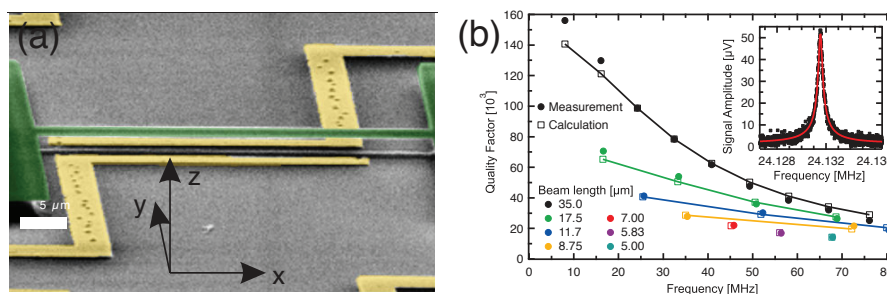


Figure 2.7: (a) SEM image of a typical high-stress silicon nitride doubly-clamped beam along with the electrodes used to dielectrically actuate the resonator. (b) Mechanical quality factor as a function of frequency for the harmonics of a family of high-stress silicon nitride doubly clamped beams (width 200 nm, thickness 100 nm and length $35/n$ μm (where $n = 1, \dots, 7$)) with frequencies below 80 MHz. Figures reproduced from [35].

2.7(b).

As the mode number increases there is a decrease in quality factor, and as the resonator length decreases so too does the quality factor of the lowest mode. This behaviour can be understood in terms of the way in which energy dissipates in an anelastic solid. As the beam oscillates under the influence of a periodic external force the stress and strain fields induced within the resonator are not in phase. This is described using a complex Young's modulus, $E = E_1 + iE_2$ where E_2 is the loss modulus. In this case some of the energy supplied to the resonator via the stress field is unable to couple to the strain field which results in this energy being converted to heat and lost.

The quality factor is related to the energy stored within the beam, $U_{n,m}$ (dominated by the displacement induced elongation energy in a stressed beam) and the energy lost in an oscillation cycle, $\Delta U_{n,m}$ (proportional to the bending energy) through $Q = 2\pi U_{n,m}/\Delta U_{n,m}$ [35]. In a stressed beam it is the elongation energy that is more strongly influenced by the stress than the the bending energy. This stronger relation between stress and elongation energy predicts a near linear increase in quality factor with stress [35].

This influence of bending loss on quality factor is also evident in the modal dependence of the quality factor. As the number of nodes within a doubly-clamped beam increases, so too does the bending energy, while the beam elongation will remain roughly constant, leading to a decrease in the quality factor. A decrease in overall beam length has a similar influence on the quality factor, as the length of the beam decreases, so too does the elongation energy, while the bending energy remains roughly constant [35].

2.4.2 Dissipation in Membranes

Nanomechanical devices fabricated from high-stress silicon nitride ($\sigma = 1.0 - 1.2$ GPa) grown by low-pressure chemical vapor deposition (LPCVD) were studied by Southworth *et al.* [33]. Using standard nanofabrication processes (which are described in section 4.5.1) square membranes with sides of length $255 \mu\text{m}$ along with $\sim 5 \mu\text{m}$ long cantilevers with thicknesses of 30 nm were fabricated and their motion detected using the optical system described in section 3.1.3. The dissipation at a range of temperatures was measured and is shown in figure 2.9 alongside comparable data for single crystal silicon and $a\text{-SiO}_2$. A plateau region in the dissipation of values between $1.5 \times 10^{-4} \leq Q^{-1} \leq 1.5 \times 10^{-3}$ (as indicated by the blue line and bar in figure 2.9) is expected for amorphous solids at temperatures between 0.1 and 10 K , however in the measurements made by Southworth *et al.* high-stress silicon nitride showed a dissipation 3 orders of magnitude less than that of $a\text{-SiO}_2$. Comparison with the dissipation seen in cantilevers (where the initial stress has been relieved) reveals a dissipation closer to that expected for $a\text{-SiO}_2$ (although still around an order of magnitude lower than expected) suggesting that this decrease in dissipation is due to the increased stress.

For a glass in this plateau region (occurring between 0.1 and 10 K) the dissipation can be described using the standard tunnelling model which models the effect of defects within the solid such as dislocations, contaminations or dangling bonds upon the dissipation. Using this model the dissipation of the solid in the plateau is described by:

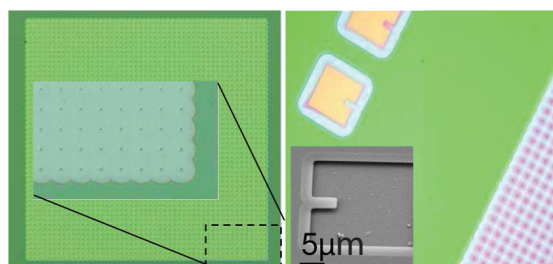


Figure 2.8: High-stress silicon nitride membranes and cantilevers measured in the work by Southworth *et al.*. Figure reproduced from [33].

$$\frac{1}{Q} = \frac{\pi}{2} C = \frac{\pi \bar{P} \gamma^2}{2 \rho c^2} \quad (2.30)$$

where \bar{P} is the spectral density of the tunnelling states, γ is the coupling energy of the tunnelling states, ρ the density of the material and c is the speed of sound. The difference in dissipation between the stressed (membrane) and unstressed (cantilever) silicon nitride is believed to be due to a modification of either the spectral density or coupling energy of the states by the stress. The tunnelling states are expected to reside on internal surfaces within the solid and it appears that the stress within the nitride introduced a strain that was sufficient to alter the asymmetry of the tunnelling states, decreasing dissipation [33].

In addition to studying material loss of high-stress silicon nitride work has also been done to study the modal dependence of energy loss in high-stress membranes [29–31] at room temperature. Wilson-Rae *et al.* [29] studied the modal dependence in high-stress silicon nitride membranes with both rectangular (sides of length $253.2 \mu\text{m}$) and circular (diameters from 14.5 to $400 \mu\text{m}$) geometries.

As mentioned earlier the clamping loss within a membrane is strongly influenced by mode shape, with classes of high-Q modes identified for rectangular ($L = 253.2 \mu\text{m}$) and circular membranes ($((m, n)|_{m, n > 1}$ with $m \sim n$ for a square [31] and $(n, 1)|_{n > 1}$ for a circular membrane [29, 30]). The common feature of these high-Q modes is their symmetry, with nodes intersecting the perimeter at evenly spaced points, resulting in

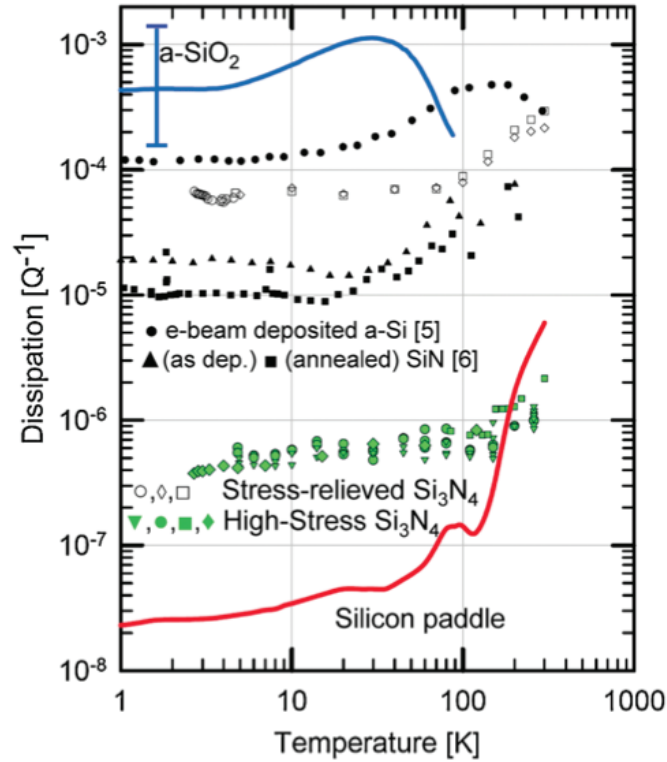


Figure 2.9: Temperature dependent dissipation measurements for high-stress silicon nitride membranes and stress relieved silicon nitride cantilevers. Also presented is comparable dissipation data for single crystal silicon and a -SiO₂. Figure reproduced from [33].

the membrane being divided into segments of equal size for which the elastic waves produced within the segments are able to destructively interfere which limits the energy lost into the supporting structure.

The dissipation measured as a function of frequency at room temperature for both membrane geometries is shown by the red plots in figure 2.10. For the rectangular membrane ($L = 253.2 \mu\text{m}$) quality factors of $\sim 5 \times 10^5 - 1 \times 10^6$ were measured, while for the circular ($D = 14.5 \mu\text{m}$) membrane quality factors of $\sim 1 \times 10^4 - 1 \times 10^5$ were observed.

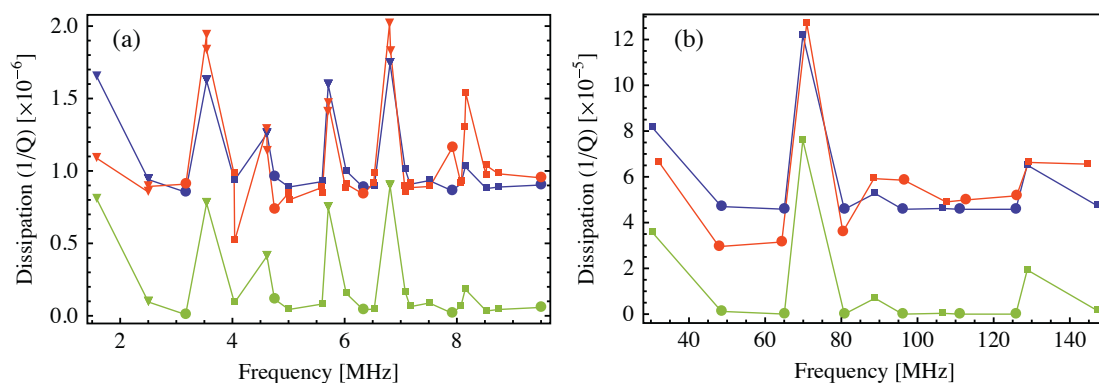


Figure 2.10: (a) Dissipation as a function of frequency at room temperature for a square membrane with sides of length $253.2 \mu\text{m}$ and thickness 12.5 nm . (b) Idem for a $14.5 \mu\text{m}$ diameter, 110 nm thick high-stress silicon nitride drum resonator. In both graphs the measured data (with an error of 10%) is shown in red, a least squares fit to theoretical model in blue and the dissipation without the offset due to clamping losses is shown in green. Figure reproduced from [29].

The dissipation dependence within the membrane was modelled as the sum of two dissipation contributions, a frequency dependent contribution due to clamping loss and a frequency independent component due to material losses within the membrane. In calculating the losses due to the supporting structure the membrane was assumed to be in the “high-stress” regime, where $t^2/D^2 \ll \sigma/E_R \ll 1$ and energy loss through the supporting structure was evaluated by looking at the overlap in frequency between the membrane and the plane wave eigenmodes (longitudinal, transverse in-plane and surface waves) within the support structure. Using this approach Wilson-Rae *et al.* were able to predict the existence of the high-Q modes observed, as shown by the least squares fit indicated by the green plots in figure 2.10, where the intrinsic dissipation $1/Q_{int}$ has been left as a fit parameter [29]. Fitting to this model allowed Wilson-Rae *et al.* to extract values for the intrinsic dissipation of 8.5×10^{-7} and 4.6×10^{-5} for the square and $14.5 \mu\text{m}$ diameter drum respectively. The difference in magnitudes of these quality factors is most likely due to the dimensions of the membranes, as the square membrane

was far larger than the circular membrane.

Measurements made by Wilson-Rae *et al.* suggest that the size of a membrane can have a large influence upon dissipation. To investigate this further Adiga *et al.* [30] at Cornell (again working with Wilson-Rae of TUM) performed further room temperature measurements on a number of circular membranes of high-stress silicon nitride with diameters ranging from 50 μm up to 400 μm . These measurements were performed under vacuum (3×10^{-7} Torr) and were designed to investigate whether the dissipation trends seen in other work [29, 31] were frequency or mode shape dependent. Measurements of a 400 μm ($t = 27$ nm) diameter membrane are shown in figure 2.11(a), where the modes have been grouped into radial families (same m index). The mode frequencies follow equation 2.24, which indicates that the membrane is stress dominated, with a phase velocity of ~ 540 ms^{-1} . As the number of azimuthal node lines increases the resonators display a decrease in dissipation, tending towards a dissipation floor of $\sim 5 \times 10^{-7}$ and a decreased dependence of the dissipation on the mode shape.

Similar behaviour is observed for the purely radial modes ($m = 1, 2, 3, \dots, n = 0$) for which the dissipation tends towards a dissipation floor of $\sim 2 \times 10^{-6}$. For higher order radial modes ($m \geq 3$) the modal dependence of the dissipation was also seen to drop off rapidly as the number of azimuthal node lines increase.

In figure 2.11(b) the effect of membrane size is explored, with dissipation as a function of frequency for membranes of 50, 150, 300, and 400 μm in diameter plotted. The dissipation of the fundamental modes of the membranes ($n = 0, m = 1$) show a dissipation which appears to be independent of mode diameter. As mode numbers increase the resonators tend towards a dissipation floor dependent on both size and frequency with fQ and D/Q both constant. The solid line in figure 2.11(b) indicates an fQ floor corresponding to 10 THz, to which the higher order modes appear to tend.

Another interesting feature of figure 2.11(b) is the behaviour of the membranes as the number of radial nodes increase. For a larger membrane ($d = 400$ μm) the dissipation shows a strong modal dependence, with dissipation decreasing as the number of

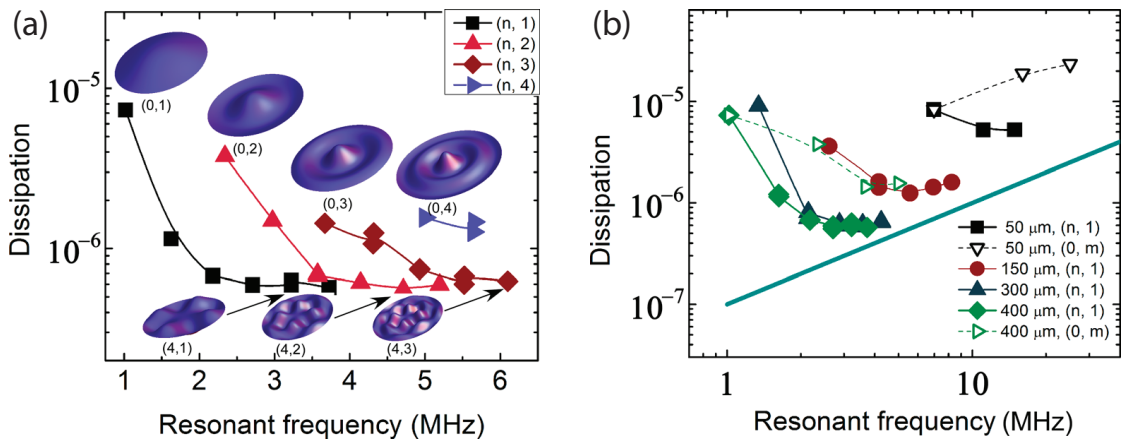


Figure 2.11: (a) Modal dependence on dissipation for 400 μm diameter circular membranes of 27 nm thick high-stress silicon nitride at room temperature for radial mode families. The lines are spline fits used as guides to the eye. (b) Dissipation and resonant frequency for a range of different diameter circular membranes at room temperature. The straight line indicates a dissipation floor corresponding to an fQ product of 10 THz. Figures reproduced from [30].

azimuthal nodes increase. For the smaller membrane ($d = 50 \mu\text{m}$) the opposite is true, with the dissipation increasing with the number of azimuthal nodes, suggesting that there is a dissipation floor for higher order azimuthal modes that is strongly dependent on membrane diameter. In the work of Yu *et al.* [31] the losses were attributed to the local curvature of the membrane, a smaller membrane would experience an increased curvature, leading to an increase in the dissipation. This was also observed by Unterreithmeier *et al.* [35] in measurements of doubly-clamped beams of high-stress silicon nitride where quality factor decreased with beam length.

Measurements of commercially available 50 nm thick membranes of high-stress silicon nitride ($\sigma \sim 0.9 \text{ GPa}$) at room temperature were made by Yu *et al.*. Measurements of membranes of size $0.5 \text{ mm} \times 0.5 \text{ mm}$ and $1.0 \text{ mm} \times 1.0 \text{ mm}$ were made for which the same class of high-Q modes were observed with symmetric material loss limited modes and asymmetric radiation loss limited modes.

Having identified the high-Q modes within the membrane Yu *et al.* then deposited a 50 nm thick film of Al onto the membrane. Figure 2.12(a) shows the dissipation measured before (green circles) and after (blue squares) the Al film was deposited. This resulted in a decrease in not only the resonant frequency of the modes ($f_{1,1}$ decreased from 410 to 260 kHz) but also the maximum Q of the membrane from $\sim 5 \times 10^7$ to 2×10^5 . Using data from the pure silicon nitride measurements the modes that were material loss limited (indicated by filled markers in figure 2.12(a)) were identified.

The membrane can be modelled as an anelastic material dissipating energy under cyclic loading. When oscillating, the stress and strain within the membrane are out of phase with one another and the energy supplied by the stress will convert to heat and be lost. In Yu's model the membrane is analysed as a plate acting under the influence of an in-plane force, with mode shape approximated as the product of two stressed beam functions. This gives a mode shape nearly sinusoidal in nature with a correction at the membrane edge to satisfy the boundary conditions.

The anelasticity of the plate is described in terms of oscillating strains introduced

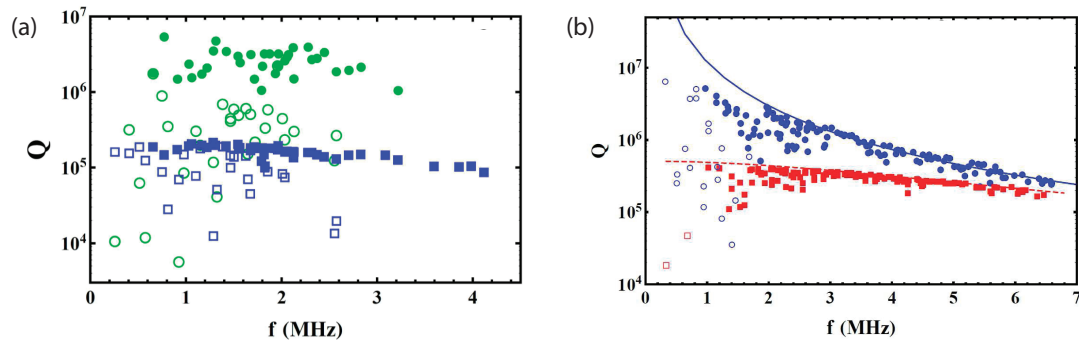


Figure 2.12: (a) Measured quality factors at room temperature for a $1.0 \text{ mm} \times 1.0 \text{ mm}$ high-stress square silicon nitride membrane before (green circles) and after (blue squares) a 50 nm thick layer of Al is deposited. Radiation loss limited modes are indicated by open markers, while filled markers indicate the material loss limited modes. (b) Measured quality factors at room temperature for a membrane completely covered with Al (red) and with Al only in the centre of the membrane (blue). Open markers indicate asymmetric modes (where one mode index is less than or equal to 2) and the line shows the calculated quality factor for each geometry. Measurements made at 300 K. Figures reproduced from [31].

by the plate motion, which make it possible to determine a quality factor for each of the vibrational modes of the membrane. Taking a complex Young's modulus, $E = E_1 + iE_2$, where the losses in the membrane are described by the loss modulus, E_2 , an effective value for the loss modulus of the SiN/Al bilayer of $E_2 = 0.55$ GPa was determined by a least squares fit. The value obtained is in good agreement with typical values obtained for thin-film polycrystalline Al.

The strain induced within the membrane (and consequently the energy loss per cycle) is proportional to the curvature of the membrane to which there are two contributors, the edge of the membrane and the region in the vicinity of membrane antinodes. If the dominant contribution comes from the edge curvature there should be a flat Q dependence with frequency, if on the other hand the curvature around antinodes were dominant then as the frequency (and the number of antinodes) increases there should be an associated decrease in Q. A large membrane displays a fairly flat Q-dependence with increasing frequency, indicating that the dominant loss contribution arises from bending at the edge of the membrane. As membrane dimensions decrease however the antinode contribution increases and a frequency dependent Q-factor is seen (as in the work by Adiga *et al.* [30]).

Yu *et al.* were able to increase the quality factor of a $1 \text{ mm} \times 1 \text{ mm}$ membrane through selective application of an Al film to the membrane. An Al film was applied, with a $50 \text{ }\mu\text{m}$ wide uncoated border around the membrane edge. Figure 2.12(b) shows the measured quality factors for a completely coated (red) and partially coated (blue) membrane.

The solid line in figure 2.12 was obtained by assigning a finite loss to the Al coated region and zero to the uncoated region around the perimeter. A least square fit yields a loss modulus of $E_2 = 0.3$ GPa, which when used to predict the behaviour of the fully coated membrane gives the red dashed line which shows good agreement with the measured quality factors of the higher modes. This ability to tune the membrane through the selective application of metallic layers is of great interest in optomechanics and may also provide a route to achieve ground-state cooling of MHz mechanical resonators, where

the highest Q-factors possible are desirable.

2.5 Summary

In this chapter we have introduced the fundamentals of nanomechanics. In addition to looking at the dynamics of resonant systems we have introduced two nanomechanical geometries, the torsional resonator and the stressed membrane, looking at their mechanical modes of oscillation. In reviewing recent studies of dissipation in high-stress silicon nitride mechanical systems we have seen that the addition of stress results in far higher quality factors than are observed in low-stress counterparts.

Chapter 3

Optical Detection of Nanomechanical Motion

Nanomechanical systems have displacements of order 1 nm in magnitude, as we shall see later this makes the wavelength of light an ideal tool for their measurement. This chapter will describe how optical techniques can be used in the measurement of micro- and nanomechanical systems as well as reviewing previous work by other groups that informed the decision to design and construct a low-finesse Fabry-Perot fibre interferometer.

Before we begin it is useful to define what is meant when we describe a system as free-space as opposed to fibre based; Free-space systems rely on separate optical components (beam-splitters, objective lenses, mirrors) precisely aligned and susceptible to perturbations of the optical path. A fibre-based system relaxes these requirements and makes it possible to guide the beam to and from the mechanical element in a single fibre optic without worrying about the misalignment of optical components or changes in path lengths. This is particularly advantageous when the mechanical device is located in the cryogenic and UHV environment found at the bottom of a dilution refrigerator. Many of the interferometers discussed in this chapter use a fibre to direct light to the device, however in this thesis when we say an interferometer is fibre based we require that a fibre coupler has been used in place of a beam splitter.

We start by describing and analysing the operating principles of the two main types of interferometer used in the optical measurement of nanomechanical devices, the Michelson and Fabry-Perot interferometers, before expanding the Fabry-Perot to include multiple layers and looking at how we can design devices with as large a responsivity as possible. Several systems used in the study of nanomechanical devices are then reviewed and the ways in which the sensitivity and operating modes have been modified to allow a wider range of devices to be measured will be discussed.

3.1 Optical Interferometry

An interferometer measures changes in path length by interfering two or more coherent beams of light. As the phase of the interfering beams varies a series of interference fringes are formed. In work by Karabacak *et al.* [36] interferometers used to detect nanomechanical motion are classified in two ways, the Michelson interferometer, shown in figure 3.1(a), which interferes light reflected from the resonator with a reference beam and the Fabry-Perot type, shown in figure 3.1(b), where a cavity (of which the NEMS is part) is formed. Mechanical motion modulates the reflectivity of this cavity, with the displacement measured by monitoring variations in the reflected optical power.

For an interferometer the contrast between adjacent fringes, known as the visibility is defined in terms of the maximum (I_{max}) and minimum (I_{min}) detected intensity as

$$V = \frac{I_{max} - I_{min}}{I_{max} + I_{min}} \quad (3.1)$$

the fringe visibility of the interferometer, which takes a value between 0 and 1, provides a measure of how sensitive the interferometer is to changes in the path lengths [37].

In order to produce fringes the interfering light must have a spatial coherence, with a phase correlation existing between the interfering beams. There are two types of spatial coherence, *longitudinal coherence*, which relates to the spectral purity of a source and *lateral coherence*, related to the size of the source [37].

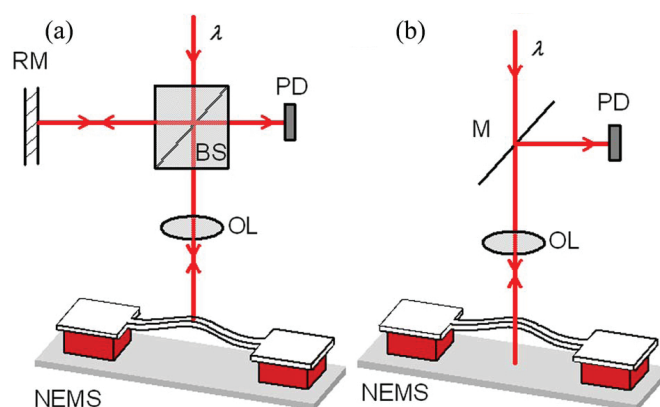


Figure 3.1: Diagram showing the two most common interferometric schemes employed in the optical detection of nanomechanical motion. (a) A Michelson interferometer and (b) A Fabry-Perot interferometer. Figure reproduced from [36].

In interferometry the most important type of coherence is longitudinal coherence, for which the coherence length, l_c , for a source of wavelength λ is related to the spectral width ($\delta\lambda$) by [37]

$$l_c = \frac{\lambda^2}{\delta\lambda} \quad (3.2)$$

As the spectral purity of a source increases so too does the coherence length. As an example a highly monochromatic source such as a HeNe laser will have a coherence length of 30 cm¹, while for a broadband source such as an LED this will be $\sim 50 \mu\text{m}$ ².

The strength of interference between two coherent beams (E_1 and E_2) of light is then proportional to the correlation function

$$|\gamma_{12}| = \begin{cases} 1 - \frac{\Delta l}{l_c} & \text{for } \Delta l < l_c \\ 0 & \text{otherwise} \end{cases} \quad (3.3)$$

where Δl is the difference between the path lengths [37]. From these relations three

¹Typical coherence length specified for a Thorlabs 633 nm HeNe laser.

²For a typical red LED (Thorlabs part no. LED631E) where $\lambda = 633 \text{ nm}$, $\delta\lambda = 10 \text{ nm}$ and $l_c = 40 \mu\text{m}$.

regimes³ can be identified:

1. **Complete incoherence** where $l > l_c$, $|\gamma_{12}| = 0$ and $V = 0$; Path difference is greater than the coherence length meaning beams are incoherent and amplitudes of beams sum incoherently - no fringes visible.
2. **Partial coherence** where $0 < l < l_c$, $0 < |\gamma_{12}| < 1$ and $0 < V < 1$; Path difference less than coherence length, meaning beams will interfere - fringes visible. Contrast decreases as path difference increases.
3. **Complete coherence** where $l = 0$, $|\gamma_{12}| = 1$ and $V = 1$; No path difference, so interfering light is completely in phase.

The regime within which an interferometer operates is where the light is partially coherent and as the path difference increases there is a decrease in the fringe contrast to the point where $\Delta l = l_c$ and interference fringes are no longer visible *i.e.* $V = 0$. In the following sections we will see how the property of coherence influences the operation of an interferometer.

3.1.1 Michelson Interferometry

The Michelson interferometer, shown in figure 3.2, is a simple and versatile arrangement first introduced by Albert Michelson in 1881 [37]. Figure 3.2 shows the typical Michelson arrangement. Light from a collimated optical source is split between the two arms by a beam splitter. In the reference arm mirror M_1 is positioned at a fixed distance, z_1 . The measurement arm contains a second mirror, M_2 , the position of which, z_2 , can be varied. The reflected light in both arms is recombined at the beam splitter where, provided it is coherent, constructive or destructive interference can occur.

The behaviour of the interferometer can be described mathematically by looking at the electric fields (the magnitude of which is the square root of the optical intensity) of

³Visibility calculated for the case where the interfering beams have equal amplitude. See section 3.1.1.

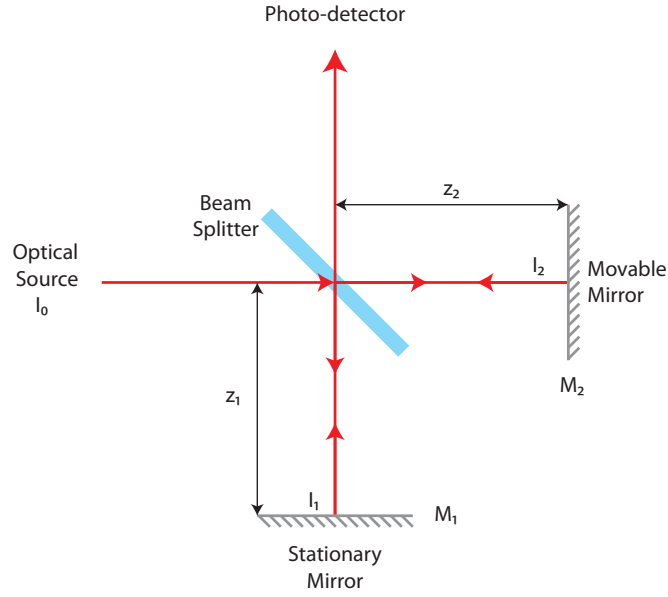


Figure 3.2: The optical arrangement of a typical Michelson interferometer.

the light in both arms. If light of intensity I_0 is injected into the interferometer then the E-field will be $E_0 = \sqrt{I_0}e^{i\omega t}$ with light returning from each arm of the interferometer given by:

$$\begin{aligned} E_1 &= \sqrt{I_1}e^{i(\omega t - 2kz_1)} \\ E_2 &= \sqrt{I_2}e^{i(\omega t - 2kz_2)} \end{aligned} \quad (3.4)$$

where $k = 2\pi/\lambda$ is the wavenumber and $I_1 + I_2 = I_0$. Upon recombining at the beam splitter (where the beam is again split) the intensity at the photodetector, I_{PD} , is

$$\begin{aligned} I_{PD} &= \frac{1}{2}|E_1 + E_2|^2 \\ &= \frac{1}{2} [I_1 + I_2 + \sqrt{I_1 I_2} (e^{i(2k(z_1 - z_2))} + e^{-i(2k(z_1 - z_2))})] \\ &= \frac{1}{2} [I_1 + I_2 + 2\sqrt{I_1 I_2} \cos(2k(z_1 - z_2))] \\ &= \frac{I_1 + I_2}{2} \left[1 + 2\frac{\sqrt{I_1 I_2}}{I_1 + I_2} \cos(2k(z_1 - z_2)) \right] \end{aligned} \quad (3.5)$$

From this we see that the intensity of light at the photodetector is dependent on the difference in path length between the reference and measurement arms of the interferometer, $\Delta Z = z_1 - z_2$, which will introduce a phase difference between the two beams

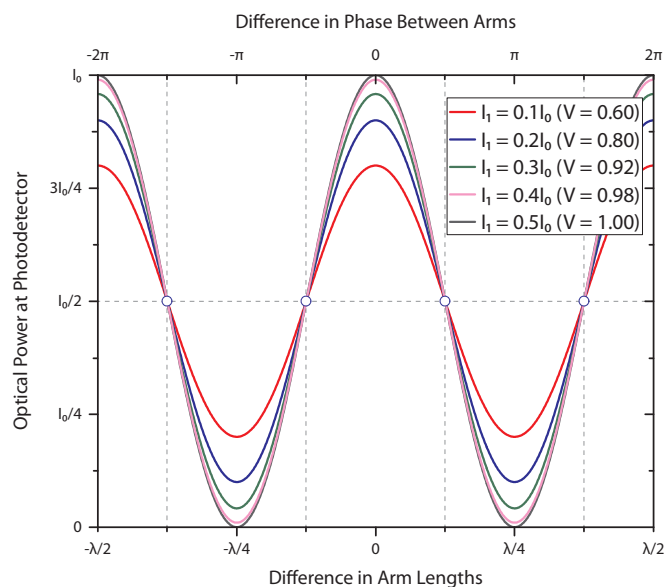


Figure 3.3: Optical intensity at photodetector for a Michelson interferometer as a function of difference in arm length. The amount of light in each arm is varied between plots, with $I_1 + I_2 = I_0$. The blue circles indicate the positions of highest sensitivity for the interferometer.

of interfering light, $\phi = 2k\Delta Z$. Figure 3.3 shows the reflected optical power for several amplitudes of light in each arm as the difference in path length is varied.

In equation 3.5 the response of the interferometer has two parts, an incoherent contribution equal to one half the sum of intensities in the two arms $((I_1 + I_2)/2)$ and a coherent contribution where light in the two arms interferes $(2\sqrt{I_1 I_2} \cos \phi)$. The strength of the interference is influenced by $|\gamma_{12}|$, which allows the intensity at the photodetector to be rewritten as [37]:

$$I_{PD} = \frac{I_1 + I_2}{2} \left[1 + 2|\gamma_{12}| \frac{\sqrt{I_1 I_2}}{I_1 + I_2} \cos(2k\Delta z) \right] \quad (3.6)$$

The fringe visibility of the interferometer, defined in equation 3.1, is a measure of the sensitivity of the interferometer to changes in the arm lengths. Equation 3.6 allows

expressions for I_{max} and I_{min} to be written:

$$\begin{aligned} I_{max} &= \frac{I_1+I_2}{2} \left[1 + 2|\gamma_{12}| \frac{\sqrt{I_1 I_2}}{I_1+I_2} \right] \\ I_{min} &= \frac{I_1+I_2}{2} \left[1 - 2|\gamma_{12}| \frac{\sqrt{I_1 I_2}}{I_1+I_2} \right] \end{aligned} \quad (3.7)$$

from which we can rewrite the visibility as

$$V = \frac{2|\gamma_{12}|\sqrt{I_1 I_2}}{I_1 + I_2} \quad (3.8)$$

recalling from equation 3.3 that as the difference in path length increases we see a decrease in the degree of coherence between the two arms and consequently a decrease in fringe contrast. Using equation 3.8 the optical intensity at the photodetector (equation 3.6) can be rewritten as

$$I_{PD} = \frac{I_0}{2} (1 + V \cos(2k\Delta Z)) \quad (3.9)$$

Having described the detected optical intensity at the photodetector we turn our attention to the conversion of this from a change in optical power to a displacement. The *responsivity* (\mathfrak{R}) of the interferometer is the rate of change of I_{PD} with arm length *i.e.* the gradient of the curve in figure 3.3 [38]. Differentiating equation 3.9 gives

$$\mathfrak{R} = -kV I_0 \sin(2k\Delta Z) \quad (3.10)$$

From which it is clear that the responsivity is dependent on three factors, (i) the intensity of light injected into the interferometer, I_0 , (ii) the visibility of the fringes, V and (iii) the initial path difference from which the displacement is measured, ΔZ . Increasing the total optical power injected into the system leads to a linear increase in responsivity. Similarly the arrangement where $I_1 = I_2$ with the interferometer arms as close in length as possible should be used to give the largest possible visibility, $V = 1$.

If the displacement to be measured oscillates about an equilibrium position, ΔZ , with an amplitude of z_0 , then for maximum responsivity ΔZ should be chosen such that the interferometer lies where the gradient of the response curve in figure 3.3 is at a maximum

($\sin 2k\Delta Z = 0$), as indicated by the blue circles. This corresponds to a difference in arm length of $\Delta Z = \pm(2m + 1)\lambda/8$ (with $m = 0, 1, 2, \dots$). At this position and for small displacements (where $\sin z_0 \sim z_0$) the change in optical power due to the motion of the resonator will be linear with oscillation amplitude (z_0), and the responsivity of the system is then

$$\mathfrak{R} = kVI_0 \quad (3.11)$$

To ensure that the interferometer has maximum responsivity path-stabilized Michelson interferometry is often used. The reference mirror is mounted upon a piezoelectric actuator connected to a PID loop. The response of the mechanical resonator produces a high frequency (> 5 kHz) modulation of the signal at the photodetector, by monitoring the low frequency components using the PID loop z_1 can be controlled via the piezoelectric actuator to hold the responsivity of the interferometer at a maximum [39].

A path-stabilised Michelson interferometer was used by Kouh *et al.* [38] in the measurement of doubly-clamped beams of silicon with a 40 nm thick layer of Cr to allow electrostatic actuation of the devices. The experimental setup used in the measurements is shown in figure 3.4.

Light from a HeNe laser (with $\lambda = 632$ nm), was passed through a beamsplitter and focussed down onto the device using a 50x objective lens with a numerical aperture of 0.5 to produce a spot with a FWHM diameter of ~ 1 μm . In order to explore the suitability of a Michelson interferometer in the detection of nanomechanical motion a range of devices with identical lengths and thicknesses, $l = 6.4$ μm and $t = 219$ nm but varying widths, $w = 1200, 600, 250$ and 170 nm were measured. The substrate behind the nanomechanical resonator introduces a cavity, formed between the device and substrate. As such the responsivity of the interferometer, \mathfrak{R}_{m+c} , will be the sum of the Michelson responsivity, \mathfrak{R}_m and the cavity responsivity \mathfrak{R}_c [38].

The responsivity of the Michelson interferometer, \mathfrak{R}_m , was calculated by subtracting the cavity responsivity (measured separately) from the total responsivity for the inter-

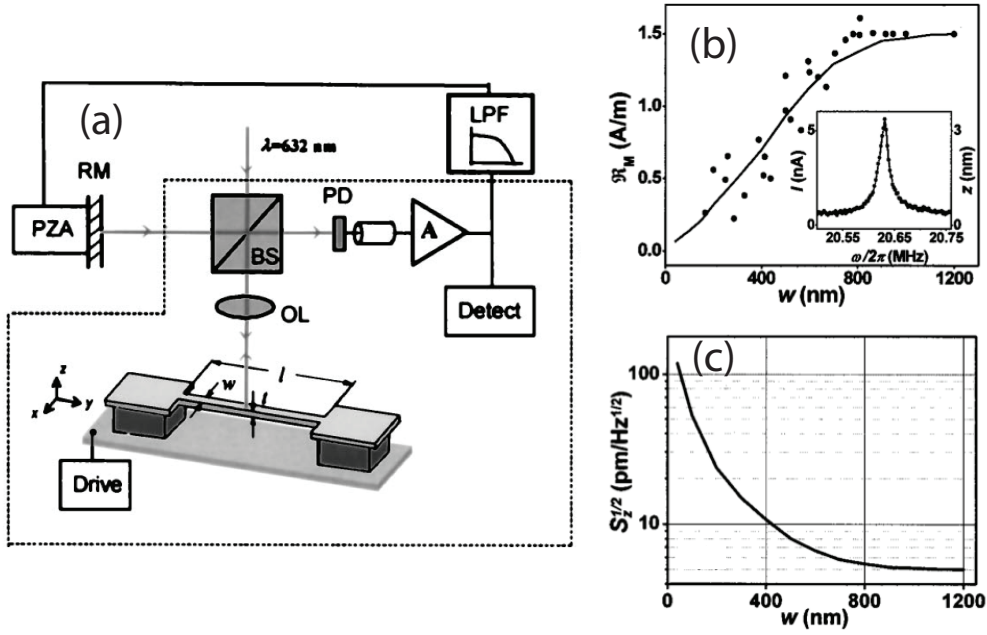


Figure 3.4: (a) Optical setup of the path-stabilized Michelson interferometer used by Kouh *et al.* in the measurement of doubly clamped silicon beams. The interferometer comprises a beam splitter (BS), objective lens (OL), reference mirror (RM) and a photodetector (PD). (b) Displacement responsivity, \mathfrak{R}_m measured (points) and modelled (line) as a function of device width, with an inset showing the frequency response for a $l \times w \times t = 8.5 \times 0.9 \times 0.219 \mu\text{m}^3$ doubly clamped beam. (c) Displacement sensitivity per unit bandwidth, $\sqrt{S_z}$, as a function of device width. Figures reproduced from [38]

ferometer, the results for which are shown in figure 3.4(b). This subtraction is equivalent to the removal of the substrate from behind the device and allowed a numerical model to be used to generate the solid line in figure 3.4(b).

There was a decrease in \mathfrak{R}_m with device width due to a decrease in the amount of light reflected from the device, leading to an increased mismatch in the optical power in each arm, degrading the visibility and consequently the responsivity of the interferometer. The plateau visible for larger widths occurs when the optical spot diameter is smaller than the device width, at this point any increase in the width of the device does not

affect the amount of light reflected from the device and consequently the responsivity will remain constant.

In figure 3.4(c) we see the effect of device width on the sensitivity per unit bandwidth of the interferometer, defined by the relation

$$S_z \approx \frac{\sqrt{S_I}}{\mathfrak{R}_m(w)} \quad (3.12)$$

where $\sqrt{S_I}$ is the dominant noise source within the interferometer, which in this case is the current noise within the amplifier, $\sqrt{S_I} = 7 \text{ pA}/\sqrt{\text{Hz}}$, resulting in a decrease in interferometer sensitivity with responsivity [38].

The work by Kouh *et al.* illustrates that as device dimensions decrease so too does the ability of a Michelson arrangement to measure these displacements. In the same work by Kouh *et al.* [38] measurements were also made using a cavity arrangement which showed that smaller devices were able to better couple to the optical field within a cavity. This degradation in sensitivity and increase in cavity effects with device size makes the Michelson arrangement poorly suited to the measurement of nanomechanical devices and led to the decision to use an optical cavity to detect mechanical displacements.

While the Michelson interferometer may not be suited to measurements of high-aspect ratio nanomechanical structures where a length scale of the devices under study are smaller than the wavelength of the light, they have been successfully applied to the measurement of nanomechanical membranes with large ($> 10 \mu\text{m}$) lateral dimensions and thicknesses on the nanometre scale. Of particular interest are the measurements made by Yu *et al.* [31] of dissipation in a high-stress silicon nitride membrane that were introduced in Chapter 2.

3.1.2 Fabry-Perot Interferometry

One of the best known optical cavities is the Fabry-Perot interferometer which is made up of two plane parallel plates between which the optical cavity is formed. While the Michelson interferometer only interferes two beams of light, the Fabry-Perot interferes the multiple reflections that occur within a cavity. A standing wave is set up within the

cavity which results in a reflectivity that is strongly dependent upon the ratio of cavity length to wavelength [37].

As with the Michelson interferometer we will begin by analysing the behaviour of the cavity mathematically, calculating the reflectivity, $R = I_r/I_0$ for the arrangement shown in figure 3.5.

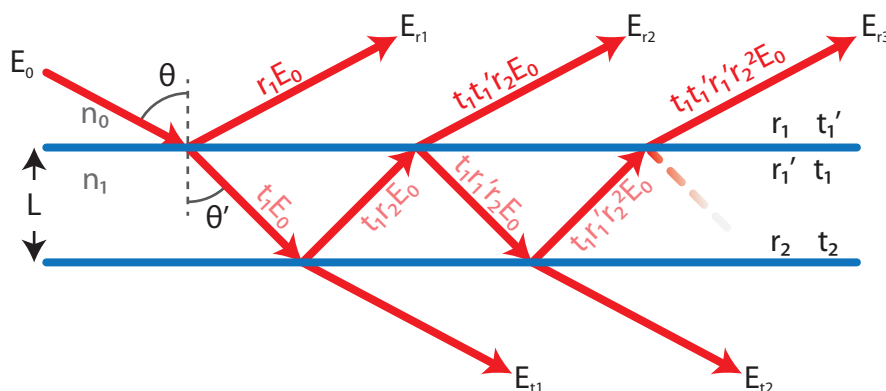


Figure 3.5: Multiply reflected rays beams in a cavity formed between two surfaces of different refractive indices. Figure adapted from [37].

Light incident upon the interface between two media of different refractive indices will undergo reflection and transmission, the magnitude of which is defined by the reflection and transmission coefficients (r and t respectively). Using these coefficients it is possible to quantify the successive reflections taking place within a cavity [37]:

$$\begin{aligned}
 E_{r1} &= E_0 r_1 e^{i\omega t} \\
 E_{r2} &= E_0 t_1 t_1' r_2 e^{i(\omega t - \delta)} \\
 E_{r3} &= E_0 t_1 t_1' r_1' r_2^2 e^{i(\omega t - \delta)}
 \end{aligned} \tag{3.13}$$

where $\delta = 2kn_1L \cos \theta'$ is the phase difference between successive reflections. A general form for the m^{th} (for $m \geq 2$) reflection can then be written as

$$E_{rm} = E_0 t_1 t_1' r_1^{m-2} r_2^{m-1} e^{i(\omega t - (m-1)\delta)} \tag{3.14}$$

The total reflected light is the sum of the reflected beams which using this general form can be written as [37, 40]:

$$\begin{aligned} E_r &= E_0 e^{i\omega t} \left[r_1 + t_1 t_1' r_2 e^{-i\delta} \sum_{m=2}^{\infty} (r_1' r_2 e^{-i\delta})^{m-2} \right] \\ &= E_0 e^{i\omega t} \left[r_1 + \frac{t_1 t_1' r_2 e^{-i\delta}}{1 - r_1' r_2 e^{-i\delta}} \right] \end{aligned} \quad (3.15)$$

and using Stokes' relations, $r_1 = -r_1'$ and $t_1 t_1' = 1 - r_1^2$ [37] simplified to

$$E_r = E_0 e^{i\omega t} \left[\frac{r_1 + r_2 e^{-i\delta}}{1 + r_1 r_2 e^{-i\delta}} \right] \quad (3.16)$$

The reflected irradiance of the cavity is the square of the E-field amplitude and from this we obtain an expression for the reflectivity of the cavity:

$$\frac{I_r}{I_0} = \frac{|E_r|^2}{|E_0|^2} = \frac{(r_1^2 + r_2^2) + 2r_1 r_2 \cos \delta}{(1 + r_1^2 r_2^2) + 2r_1 r_2 \cos \delta} \quad (3.17)$$

from which we see that the reflected optical power is dependent on the cavity length, contained within δ . A mechanical resonator can be used to modulate the cavity length and the motion detected via the change in the reflected optical power. Figure 3.6 shows equation 3.17 evaluated as a function of cavity length for $r_2 = 0.8$ with r_1 varied from 0.2 to 0.8. Two figures of merit for the Fabry-Perot cavity are also shown, the fringe visibility (defined using equation 3.1) and the cavity finesse, \mathcal{F} :

$$\mathcal{F} = \frac{\Delta\lambda}{\delta\lambda} \quad (3.18)$$

which relates the spacing between ($\Delta\lambda$), and the full width half maximum, ($\delta\lambda$), of peaks in the transmission spectrum⁴ and is a measure of both resolving power and how well the cavity is able to store the injected optical power. As the finesse increases the sharp peaks typical of a Fabry-Perot cavity begin to appear, as can be seen from the plot for $r_1 = 0.8$ in figure 3.6.

⁴The transmission of the cavity, $T = 1 - R$

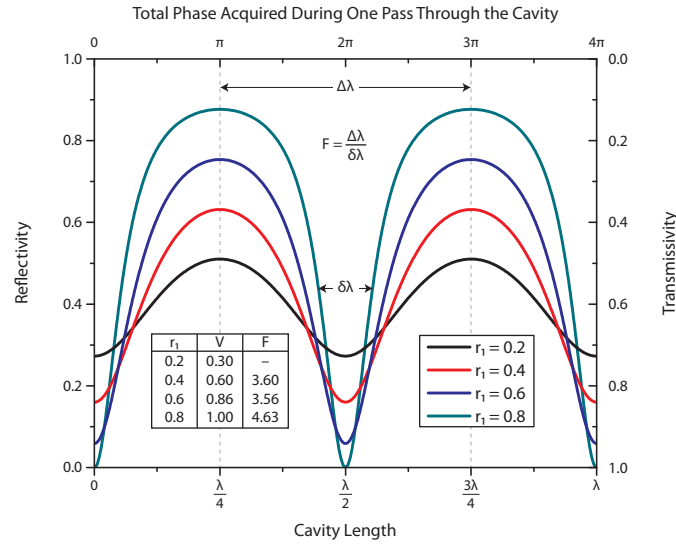


Figure 3.6: Simulation of the reflectivity of a Fabry-Perot cavity as a function of cavity length. The value of r_2 is fixed at 0.8, while r_1 takes a range of values.

When detecting a mechanical displacement that modifies the overall cavity length a larger Finesse allows a smaller change in cavity length to be detected, with the maximum gradient of the curves in figure 3.6 increasing with r_1 .

The plot of $r_1 = 0.2$ shows the response of a low-finesse cavity, which more closely resembles the two-beam interference seen in a Michelson interferometer. For the interface between glass ($n = 1.5$) and air ($n = 1.0$) there will be a reflectivity of $R = 0.04$, by including only the contributions from I_{r1} and I_{r2} we can approximate the cavity as a two-beam interference. This is a reasonable approximation to make as the low reflectivity at interface 1 means that after just one pass through the cavity 96 % of the light will exit and higher order reflections can be ignored.

The response of a two-beam system is of the form $R = R_0 + R_{sig} \cos 2\delta$ [41, 42]. This is shown in figure 3.7 and is analogous to the Michelson interferometer introduced in section 3.1.1 with the 4 % of light reflected at the fibre interface providing a reference beam that interferes with the light reflected from the mechanical element.

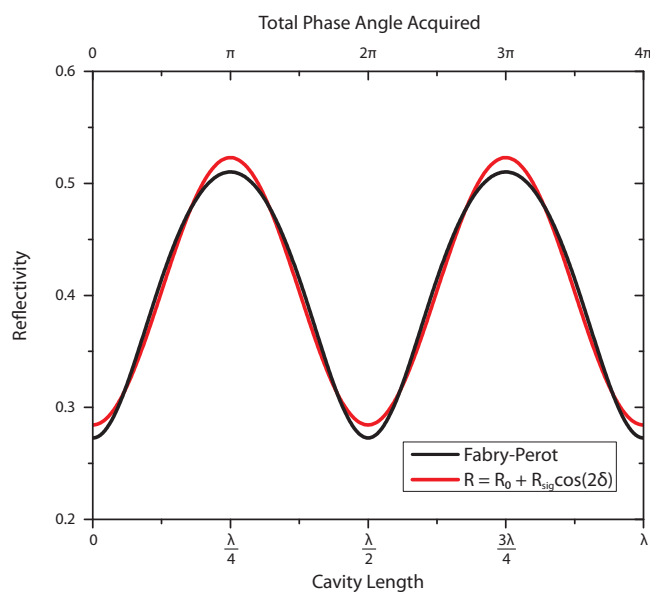


Figure 3.7: Comparison of the reflectivity curve for $r_1 = 0.2$ and $r_2 = 0.8$, and an approximation to it by the function $R_0 + R_{sig} \cos 2\delta$.

As in the case of the Michelson interferometer in order to detect changes in the path length introduced by the mechanical motion the light must be coherent and able to interfere. At a minimum this requires that the coherence length be at least twice the cavity length, however the initial path difference will decrease the correlation function, $|\gamma_{12}|$, and consequently the fringe visibility.

Having introduced the Fabry-Perot interferometer in both the high- and low-finesse configurations we now turn our attention to how micro- and nano-mechanical resonators can be incorporated into the cavity. There are three common ways in which this is achieved, with a cavity formed between (i) the fibre and the top surface of a non-transparent mechanical element, (ii) the fibre and the substrate with a semi-transparent mechanical element positioned within the cavity, or (iii) within the layers of the mechanical resonator itself, which will now be discussed.

Multi-Layer Film Theory

In a nanomechanical resonator the separation between the mechanical element and the substrate upon which the resonator is fabricated can be used to form an optical cavity. As the resonator-substrate separation varies, so too does the reflected optical power. This decrease in overall cavity length makes it possible to use light with a far shorter coherence length, l_c , reducing interference between defects within the optical system and allowing the cavity length to be well defined within the device itself.

For a resonator designed to act as an optical cavity it is important that the substrate be designed to give a resonator with maximum responsivity. For several layers of varying refractive index a beam of light propagating through the device will experience successive reflections and transmissions at the layer boundaries, the interference of which can be described by a transfer matrix for the system which is defined using multi-layer film theory.

Using the method described in [37] it is possible to use matrix algebra to calculate the reflectivity of a multi-layer film stack. In this analysis it is assumed that the films are both isotropic and homogeneous and that the beam size is large compared to any lateral displacements (allowing the multiple reflections to be recaptured). To ensure path differences are less than the coherence length of the light we also require that the thickness of the individual layers be of the same order as the wavelength of the light, ensuring that interfering beams are coherent.

A ray of light with wavelength λ incident at an angle of θ upon a medium of thickness t and refractive index n will experience a phase shift, δ , after passing through the layer of:

$$\delta = \frac{2\pi}{\lambda} n t \cos \theta \quad (3.19)$$

For coherent light the successive reflections occurring at the interfaces between different media can be summed coherently using a transfer matrix. The system studied in this work for which we will calculate the reflectivity is shown in figure 3.8.

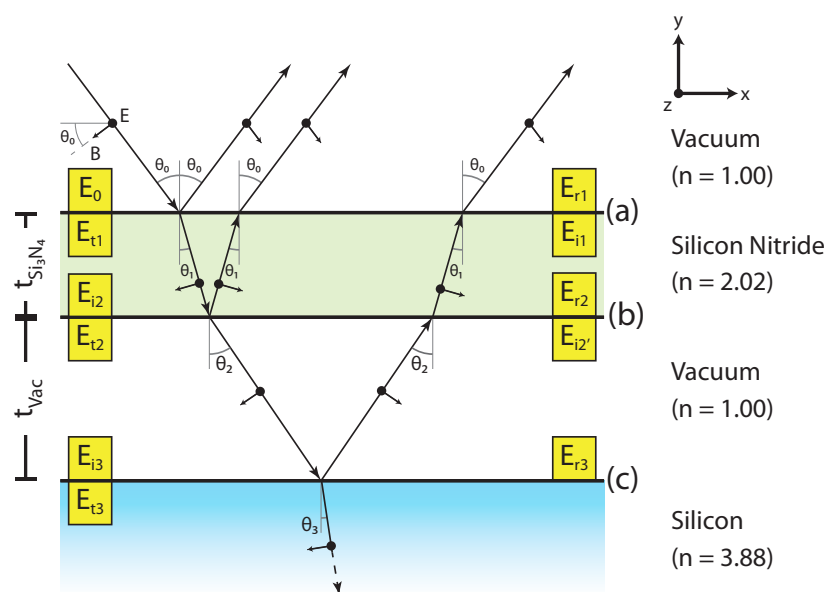


Figure 3.8: Diagram used in the multi-layer film theory calculation described in this section. Diagram adapted from [37], with values for refractive indices obtained from [43]

The magnitude of the \mathbf{E} - and \mathbf{B} -fields on either side of an interface (the yellow boxes in figure 3.8) must be equal to ensure continuous tangential components across the boundary. Using the relation $B = \frac{E}{\nu} = \left(\frac{n}{c}\right) E = n\sqrt{\epsilon_0\mu_0}E$ we can relate the \mathbf{E} - and \mathbf{B} -fields to one another via the wave speed, ν , and refractive index of the media. This allows the fields at one boundary to be related to the next by the relation:

$$\begin{aligned} \begin{bmatrix} E_a \\ B_a \end{bmatrix} &= \begin{bmatrix} \cos \delta & \frac{i \sin \delta}{\gamma} \\ i\gamma \sin \delta & \cos \delta \end{bmatrix} \begin{bmatrix} E_b \\ B_b \end{bmatrix} \\ &= \mathfrak{M} \begin{bmatrix} E_b \\ B_b \end{bmatrix} \end{aligned} \quad (3.20)$$

where \mathfrak{M} is referred to as the transfer matrix and $\gamma = n\sqrt{\epsilon_0\mu_0} \cos \theta_0$. The overall transfer matrix for the system is then the product of the transfer matrices of the individual layers

$$\begin{bmatrix} E_a \\ B_a \end{bmatrix} = \mathfrak{M}_1 \mathfrak{M}_2 \mathfrak{M}_3 \dots \mathfrak{M}_N \begin{bmatrix} E_N \\ B_N \end{bmatrix} \quad (3.21)$$

$$\begin{bmatrix} E_a \\ B_a \end{bmatrix} = \mathfrak{M}_{stack} \begin{bmatrix} E_N \\ B_N \end{bmatrix}$$

with the matrix elements of the transfer matrix describing the entire system labeled as:

$$\mathfrak{M}_{stack} = \begin{bmatrix} m_{11} & m_{12} \\ m_{21} & m_{22} \end{bmatrix} \quad (3.22)$$

which can then be used to calculate a value for the reflection coefficient, $r = E_{r1}/E_0$, of

$$r = \frac{\gamma_0 m_{11} + \gamma_0 \gamma_s m_{12} - m_{21} - \gamma_s m_{22}}{\gamma_0 m_{11} + \gamma_0 \gamma_s m_{12} + m_{21} + \gamma_s m_{22}} \quad (3.23)$$

To maximize the interferometer responsivity the resonator is designed to give a large change in reflectivity on resonance. By varying the thickness of the layers making up the resonator and evaluating equation 3.23 we can determine a range of thicknesses where we expect a large change in the reflected optical signal when the NEMS resonator is displaced.

Taking values for the refractive indices of silicon nitride as $n = 2.022$ and silicon as $n = 3.882$ [43] the reflectivity for a range of vacuum and silicon nitride thicknesses for light (with $\lambda = 633$ nm) normal to the sample were calculated. Figure 3.9 shows calculated reflectances for a range of film thicknesses, with the box indicating the starting point for determining the thickness of dielectric layers to be deposited.

The reflectivity of four nitride thicknesses as a function of the vacuum gap thickness are shown in figure 3.10. In order that the interferometer have maximum responsivity a target nitride thickness after processing of 130 nm with a vacuum gap of 570 nm was chosen. This allowed some tolerance in processing parameters while still giving a fairly

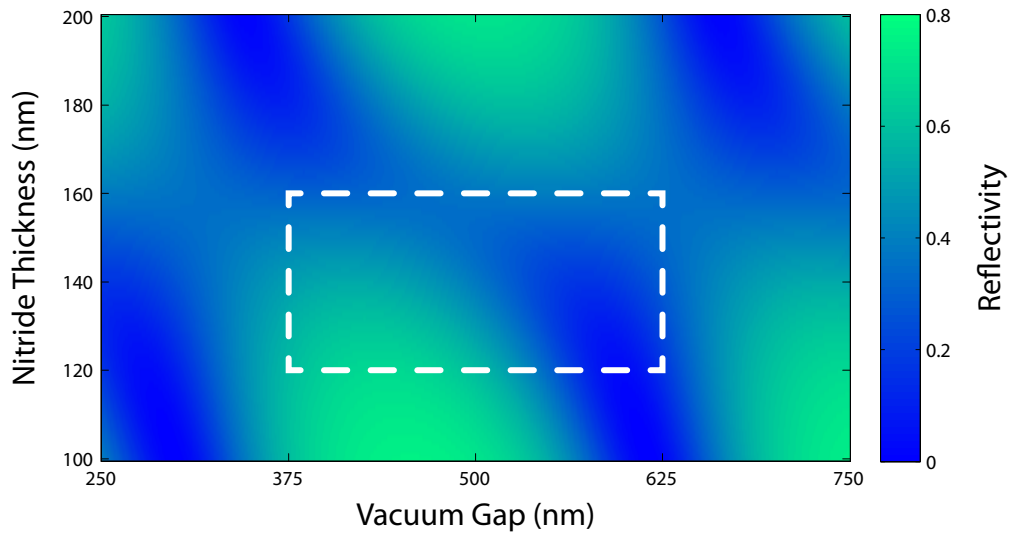


Figure 3.9: Plot of the calculated reflectance at normal incidence of the multi-layer film structure for a range of nitride and vacuum thicknesses at a wavelength of 633 nm. The region enclosed by the dashed lines is the target range of film thicknesses.

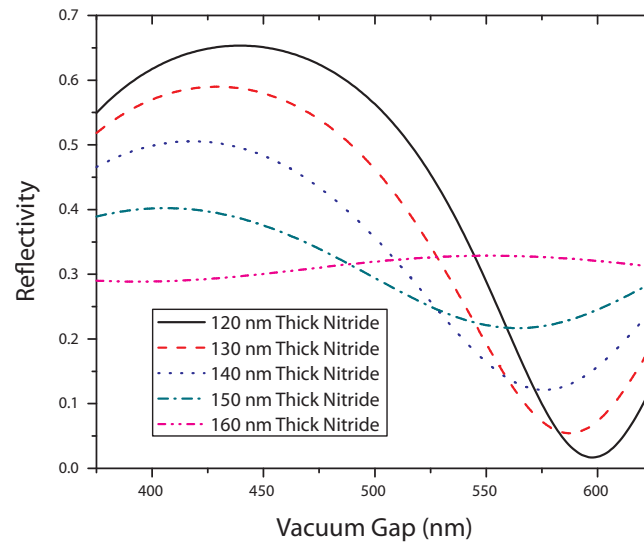


Figure 3.10: Calculated reflectance at normal incidence of the multi-layer film structure as a function of vacuum gap for several nitride thicknesses at a wavelength of 633 nm.

high sensitivity, with an expected reflectance after processing of 0.3 – 0.4. Full details of the processing parameters and the substrates purchased are given in Chapter 4.

3.1.3 Review of Previous Work Using a Cavity to Detect Nanomechanical Motion

We now turn our attention to work previously carried out to detect mechanical motion using an optical cavity, these will be divided into high- and low-finesse systems.

High-Finesse Cavities Used in the Detection of Mechanical Motion

In the previous section it was shown that as the value of r_1 increased so too did the finesse of the cavity. Experimentally this has been achieved by evaporating a thin layer of gold onto the bare end of a fibre, as in the case of several micro- and nano-mechanical systems [44–46], producing a higher finesse cavity with an increased responsivity.

Favero *et al.* [44] used this approach to optically cool a silicon micromirror. Light from a diode laser ($\lambda = 1.3 \mu\text{m}$) was coupled into one input of a 2×2 single mode fibre coupler and directed to a cavity formed between the end of the fibre and a square silicon micromirror ($2.4 \times 2.4 \times 0.1 \mu\text{m}^3$) mounted on a cantilever. Light emerging from the fibre (the polished face of which was coated with 32 nm of gold) was collimated and focussed onto the mirror by a pair of lenses to produce a cavity with $\mathcal{F} = 5.85$.

Measurements made at a pressure of 10^{-5} mbar and a temperature of 300 K are shown in figure 3.11. Using an optical power of $P_1 = 18.5 \mu\text{W}$ a quality factor of $Q = 1059$ was measured that was unrelated to the detuning of the cavity. For higher optical powers ($P_2 = 320 \mu\text{W}$ and $P_3 = 530 \mu\text{W}$) the power spectrum was found to depend strongly on the cavity detuning, with the quality factor ranging from 20 to 1100.

For a tuned cavity a standing wave will form, with a node at both of the interfaces, in this case the net flow of optical power into or out of the cavity is 0. If the cavity length is changed (detuned), power will flow into or out of the mechanical element. The direction of this power flow is defined by the direction in which the cavity is detuned,

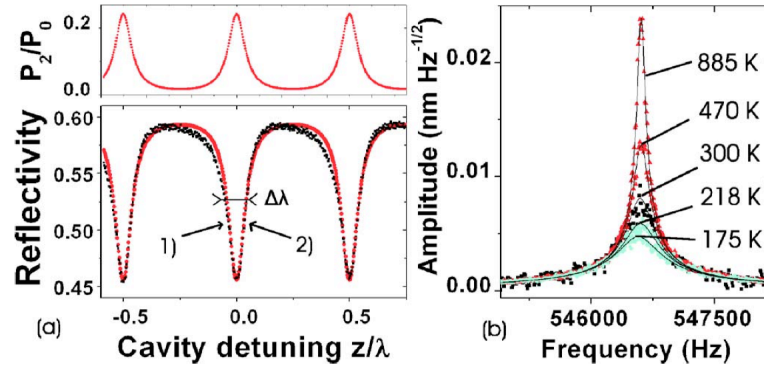


Figure 3.11: The lower plot in (a) shows the measured (black) and the modeled (red) reflectivity from the cavity, along with markers indicating negative detuning (position 1) and positive detuning (position 2). The upper plot shows a simulation of reflectivity of the cavity. (b) shows measurements of the thermal noise of the cantilever at negative detuning (175 and 218 K) and positive tuning (470 and 885 K). The measurement at 300 K was made using a low optical power. Figure reproduced from [44].

for red detuning (position 1) power flows out of the resonator, resulting in cooling, while for blue detuning (position 2) power flows into the resonator leading to heating (or amplification) [47].

An effective temperature calculated from the Brownian motion of the cantilever showed these detuning effects. For negative detuning (position 1 in figure 3.11(a)), the cantilever was seen to cool, with effective temperatures of 218 K (P_2) and 175 K (P_3). When positively detuned (position 2), heating was seen, with effective temperatures of 470 K (P_2) and 885 K (P_3).

This effective temperature change arises from the fact that an optical field incident on a surface exerts a radiation pressure. For a low optical power this pressure is small enough to be ignored, but as the optical power increases, so too does the magnitude of this force. The optical field circulating within a high-finesse cavity is reinforced by the multiple reflections, amplifying the force experienced by the micromirror. Detuning to a position where the cavity lies on a slope of the reflectivity allows this force to modify

the damping of the mirror, leading to the changes seen in the effective temperature of the cantilever.

In a similar experiment Vogel *et al.* were able to optically tune the spring constant of an AFM cantilever [46]. This is similar to the measurements made by Favero *et al.*, but in this instance the cantilever is actively driven on resonance and the photoinduced damping of the resonator analysed in terms of a change in the effective spring constant of the system. A similar damping effect was also seen in work carried out on doubly-clamped beams of high-stress silicon nitride measured by Unterreithmeier *et al.* [48] that will be discussed in the following section.

Mulhern *et al.* [49] constructed a fibre displacement sensor where, to avoid the complication of thermally evaporating gold onto the fibre a layered compound such as NbSe₂ or TiS₂ was attached to the tip. These crystal layers are then cleaved by repeatedly touching them to adhesive tape until laser light penetrates the layers, which allowed sharp (if somewhat asymmetrical) fringes to be obtained.

Low-Finesse Cavities Used in the Detection of Mechanical Motion

One of the first uses of a fibre interferometer in the study of nanomechanics is the system used by Azak *et al.* [16], the experimental setup shown in figure 3.12 was used to measure the motion of doubly-clamped beams of silicon coated with a 10 nm thick optically transparent layer of aluminium for electrostatic actuation. The cavity is formed between the fibre and substrate, with the NEMS positioned between the two as shown on the right hand side of figure 3.12.

Light from a diode laser ($\lambda = 658$ nm) was coupled into port 1 of a single mode fibre coupler. This optical power was equally split across ports 3 and 4 of the coupler, with a photodetector at port 3 monitoring the light incident on the sample. Light was directed to the NEMS by the bare fibre at port 4 which was placed within 10 μm of the surface (approximately 2 core diameters). Light incident on the nanomechanical beam and the substrate was reflected and recaptured by the fibre. The motion of the mechanical

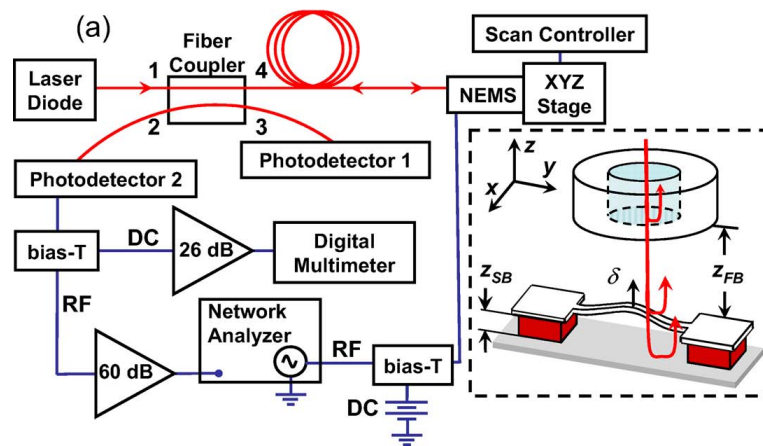


Figure 3.12: Experimental setup used by Azak *et al.*. 658 nm wavelength light from a diode laser is coupled into a 3 dB coupler at port 1. The light is equally split across ports 3 and 4. Light exiting port 3 is monitored via photodetector 1, allowing the sample irradiance to be measured. Light exiting the bare fibre at port 4 is incident on the nanomechanical device. Light reflected by the resonator is recaptured by the fibre and the intensity of reflected light monitored using photodetector 2 at coupler port 2. Image reproduced from [16]

element within the cavity modulated the reflectivity, which was monitored at port 2 using photodetector 2. A bare fibre minimizes the overall length of the optical cavity, however the small separation between sample and fibre can lead to a contamination of the tip if care is not taken when positioning the sample.

In figure 3.13(a) we see images of the nanomechanical resonators obtained using a scanning electron microscope and (b) by moving the substrate relative to the fibre while recording the reflected dc light level. The blurring of the image is due to the spreading of the light as it leaves the fibre. The beam profile was measured using a knife edge technique [50], where the fibre was scanned across a photodiode patterned with Cr and the fibre to sample separation (Z_{FB}) varied, the results of which are shown in figure 3.13(c). The diameter of the fibre core was measured to be $5.14 \mu\text{m}$, with the spreading of the beam described by a Gaussian function with a Rayleigh range, $Z_0 = 33.85 \mu\text{m}$. Given that the features lay well within $2Z_0$ (the distance over which a gaussian beam is considered collimated [37]) and should have a uniform reflectivity the contrast seen in figure 3.13(b) is attributed to the diffraction of light from the NEMS [16].

Measurements of the frequency response of a $l \times w \times t = 8 \times 0.36 \times 0.23 \mu\text{m}^3$ doubly clamped beam are shown in figures 3.13(d) and (e). The resonant frequency was measured to be $f_0 \sim 35.5 \text{ MHz}$, with a quality factor, $Q \sim 175$. The effect of varying the optical power from 0.25 to 1.25 mW on the displacement signal amplitude is shown in figure 3.13(d). The amplitude was seen to scale linearly with optical power, with no discernable effect on the quality factor or resonant frequency of the device. It should be noted however that these measurements were made at atmospheric pressure, so gas damping would be the dominant dissipation mechanism and as such optical damping will have little effect upon the resonator.

The effect of the fibre separation distance, Z_{FB} , on the displacement signal at $P = 0.75 \text{ mW}$ is shown in figure 3.13(e). As Z_{FB} was increased the amount of light recaptured by the fibre (and consequently the detected signal) decreased. From this it is clear that for a bare fibre interferometer to successfully measure the displacement

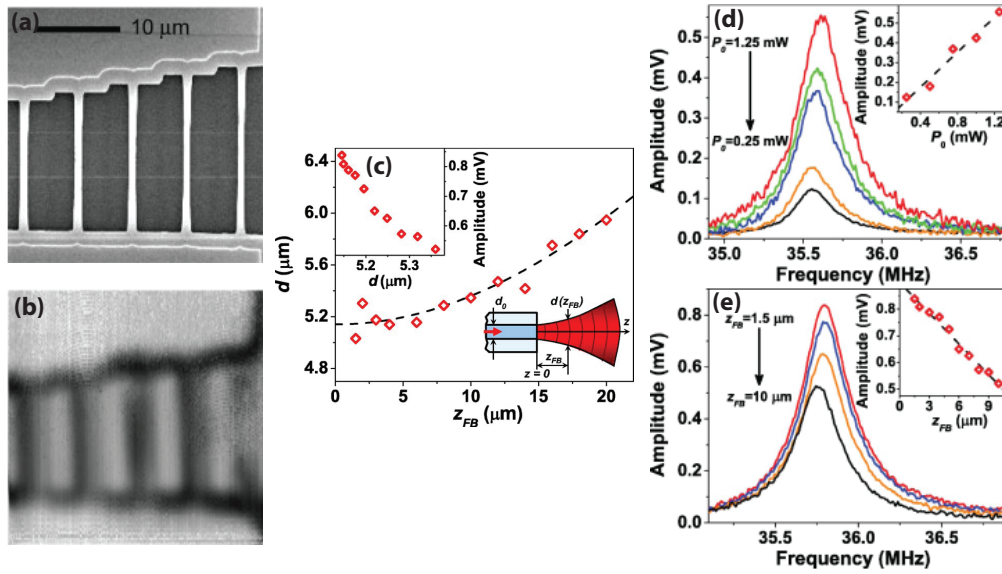


Figure 3.13: Experimental results obtained by Azak *et al.*. Images of the sample taken using (a) a Scanning Electron Microscope and (b) the interferometer are shown. (c) shows the spot size produced by the fibre measured as a function of the fibre to sample separation, z_{FB} , along with a fit to a Gaussian function. (d) and (e) Shows the frequency response of a doubly clamped silicon beam as a function of optical power and fibre sample separation (Z_{FB}) respectively. Figures reproduced from [16]

of a nanomechanical resonator it is essential that the resonator be within several core diameters of the fibre ($Z_{FB} \lesssim 10 \mu\text{m}$).

In the work of Azak *et al.* the fibre tip could become contaminated if it came into contact with the surface. To minimize the risk of this occurring the fibre-sample separation can be increased by inserting a pair of aspheric lenses into the cavity (in the same manner as Favero *et al.* [44]). This approach was employed by Southworth *et al.* [33] where the commercially available attoCFM II confocal microscope produced by Attocube Systems [51] was used in the measurement of high-stress silicon nitride membranes (discussed in Chapter 2). The design of this system is shown in figure 3.14(a), and is described in the work carried out by Hoegle *et al.* [52] in collaboration with Attocube Systems.

Light is coupled into one port of a fibre directional coupler and directed to a pair of aspheric lenses housed within a titanium assembly. The collimating lens has a focal length of 5.00 mm with numerical aperture 0.15, chosen to match the numerical aperture of the fibre (0.13), ensuring that light exiting the fibre is captured and collimated by the lens. The collimated light is then focussed down onto the sample surface by a lens with a shorter focal length (1.5 mm) and higher numerical aperture (0.55), allowing a smaller lens-sample separation and an increased light capturing ability. The use of aspheric lenses reduces spherical aberrations in the beam, but will introduce chromatic aberrations into the system, with light of different wavelengths being brought to a focus at different focal lengths. For an interferometer where only one wavelength of light is used this can be accounted for by adjusting the vertical position of the sample. Light reflected from the sample passes back through the lenses where it is recaptured by the single-mode fibre and the intensity monitored using a photodetector [52].

Figure 3.14(b) shows the reflected optical power as the cavity length (fibre-sample separation) is varied through the focal point of the system. The graphs illustrate the response for incoherent (top) and coherent (bottom) light. In the coherent case the fringes expected from the interference of coherent light (as predicted by equation 3.17)

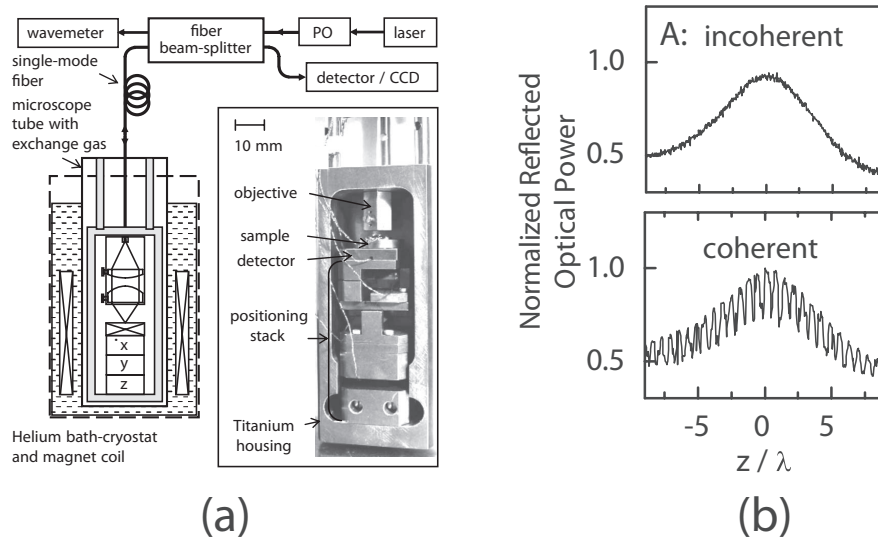


Figure 3.14: (a) Optical arrangement of a low temperature confocal microscope similar to that used by Southworth *et al.* in their measurement of high-stress silicon nitride NEMS devices. Light from a tunable laser is coupled into one port of a single mode fibre coupler that directs half the light to the sample where it is collimated and focussed onto the sample by a pair of aspheric lenses. Light reflected from the sample passes back through the lenses and is recaptured by the fibre coupler that directs it to a photodetector used to monitor the reflected optical intensity. (b) Normalized reflected optical power from a GaAs heterostructure as the sample is swept in the z -axis through the focal point of the optics for incoherent (top) and coherent (bottom) light. Figure reproduced from [52].

are visible, while for incoherent light the fringes are no longer present. For a confocal microscope the fringes are not desirable as the detected optical power should vary smoothly through the focus. When used as an interferometer a degree of coherence is required to increase the responsivity of the interferometer. For maximum stability the cavity length should be minimized as far as possible [52].

The insertion of aspheric lenses into the optics makes it possible to increase the separation between the sample and optics, from $\sim 10 \mu\text{m}$ in the case of the bare fibre to several millimetres, as well as leading to an increase in the ability of the optics to recapture the light reflected from the sample when compared to a bare fibre arrangement.

One of the key limitations in any transduction scheme used to detect nanomechanical motion arises from the large frequency range over which the vibrational modes lie, requiring detection electronics with large bandwidths which will introduce noise into the system. A well defined component at a lower frequency for which the detection electronics have been specifically engineered can be produced using a technique known as downconversion. When a modulation, f_{LO} , and an rf signal, f_{rf} , are mixed the output will have both sum and difference components, $f_{rf} \pm f_{LO}$. This technique has been used in several nanomechanical experiments where piezoresistive [53] and magnetomotive [54] detection was used. Stroboscopic downconversion was used to optically detect nanomechanical motion in doubly clamped beams of stressed silicon nitride by Unterreithmeier *et al.* [15, 17], the experimental setup of which is shown in figure 3.15, with the beams actuated using the gradient field method discussed in section 1.2.2.

A free-space Fabry-Perot arrangement was used, with light directed to the nanomechanical resonator by a single mode fibre, the face of which also formed one interface of the cavity. A diode laser gated at f_{rf} , produced a modulation of the incident optical power. This optical modulation frequency was also mixed with the output of a network analyzer, $f_{LO} = 0.9 \text{ MHz}$, and the difference component used to drive the nanomechanical device. Light incident upon the photodetector contained both the sum and difference components of the drive frequency and the optical modulation, $f_{rf} \pm (f_{rf} - f_{LO})$. Measuring the response at f_{LO} using a network analyzer allowed Unterreithmeier *et al.* to

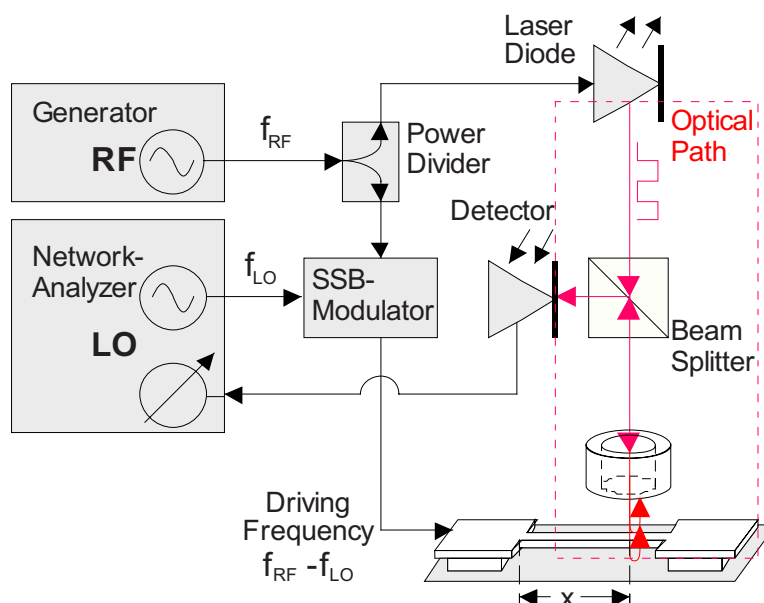


Figure 3.15: Experimental setup used by Unterreithmeier *et al.* for stroboscopic down-conversion. A diode laser is modulated at f_{rf} and passed through a beam splitter and on to the NEMS by way of a single mode fibre. The NEMS is driven at a drive frequency of $f_{rf} - f_{LO}$. The light reflected from the NEMS will contain both sum and difference components, by monitoring the difference component (at f_{LO}) using a network analyzer the frequency response is obtained. Figure reproduced from [15].

measure harmonics of the beam up to 60 MHz using a photodetector and amplifier for which the maximum bandwidth was 10 MHz. The fixed detection frequency meant that any amplification electronics and filters need only operate at f_{LO} allowing the bandwidth to be tightened and the noise within the system to be reduced.

Measurements made on the second harmonic of a $l \times w \times t = 35 \times 0.25 \times 0.1 \mu\text{m}^3$ doubly clamped beam are shown in figure 3.16(a), with (b) showing the effect of mode number on frequency (left axis) and quality factor (right axis), the line is a linear fit of frequency to mode number, indicating that the beam is behaving as a string under tension as opposed to a stiff beam. By scanning the spot along the length of the beam

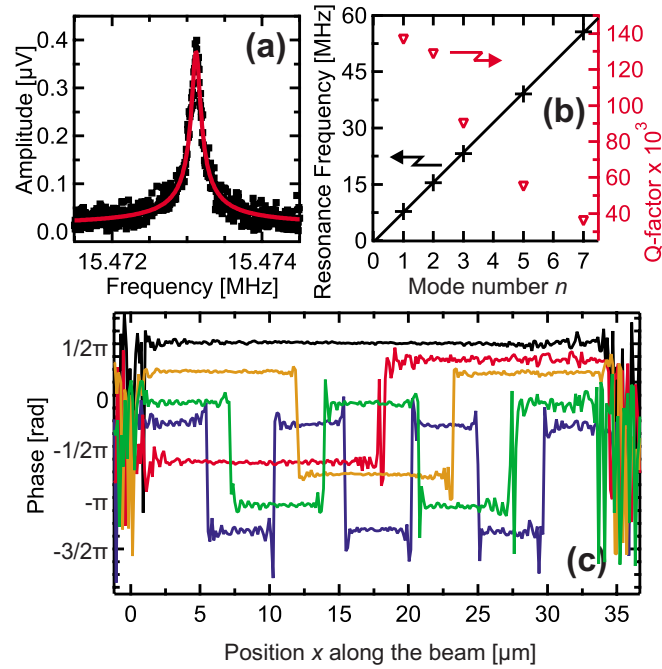


Figure 3.16: Experimental results obtained by Unterreithmeier *et al.*. (a) Shows the frequency response of the second harmonic of a $35 \mu\text{m}$ long doubly clamped beam. (b) Shows the relation between resonant frequency and quality factor as the mode number is increased. (c) Shows the phase of the detected signal as a function of position along the doubly-clamped beam, as a node is passed through the phase changes by π . Figure reproduced from [15].

it was possible to confirm the mode under study by monitoring the phase, as shown in figure 3.16(c). On passing through a node on the beam a π phase shift was observed, arising from the fact that on either side of a node the direction of beam displacement will change.

In another set of measurements Unterreithmeier *et al.* [48] formed not only the cavity, but also the photodetector within the resonator itself. Measurements were made of doubly-clamped beams of high-stress silicon nitride fabricated on an n-doped silicon substrate ($\approx 10 \Omega\text{cm}$) coated with a 400 nm thick layer of silicon dioxide. A hole etched

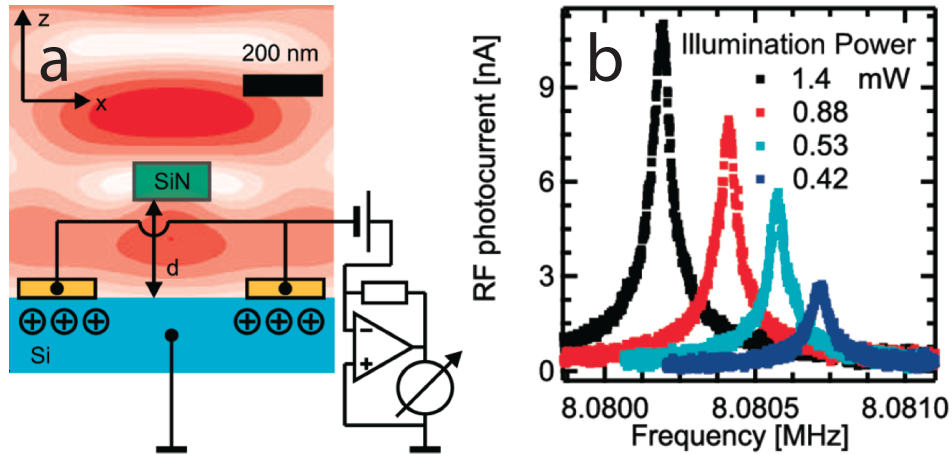


Figure 3.17: Experimental setup of the on-chip detection scheme used by Unterreithmeier *et al.*. (b) Shows a schematic arrangement of the detector configuration, along with the optical intensity in the near-field of the resonator. (d) The response of the NEMS as a function of optical power incident upon the sample. Figure reproduced from [48].

through the silicon dioxide allowed metal electrodes to be deposited in direct contact with the silicon to form a Schottky diode that when biased would act as a photodiode. A schematic of this arrangement is shown in figure 3.17(a) along with a simulation of the resulting optical field in the vicinity of the NEMS. Biasing the electrodes relative to the substrate produced a photocurrent which the movement of the resonator modulated. This arrangement is of particular interest, as by integrating the photodetector into the NEMS itself the optics required could be reduced to only an optical source. A fibre was used to direct light from either a diode laser (DL, $\lambda = 670$ nm) or a superluminescent diode (LED, $\lambda = 750$ nm) to the sample within a vacuum chamber ($P \leq 10^{-4}$ mbar) at room temperature.

The resonator responses shown in figure 3.17(b) are for a range of illumination powers and while larger optical powers led to an increase in the measured photocurrent, there was an associated decrease in resonant frequency with optical power, indicating a damping of the resonator. At higher intensities the non-uniform optical field damps

the resonator, shifting the resonant frequency to a lower value. This force arises from the non-uniform E-field in the vicinity of the nanomechanical device produced by the incident light. Interestingly the mechanism behind the damping force that arises from the optical E-field is identical to the way in which the resonator is actuated using the gradient field technique to generate a time varying non-uniform E-field (as introduced in section 1.2.2).

3.2 Design Decisions Based on Previous Work

Based on the previous work carried out on optically detecting nanomechanical motion it was decided to design and construct a cavity based interferometer. The Michelson interferometer was discounted as the decrease in responsivity and increase in cavity effects with device dimensions, combined with the geometry of the nanomechanical structures makes a cavity based interferometer the logical choice.

A fibre was chosen to allow access to the IVC of a dilution refrigerator, with the cryostat having previously been used successfully as a low temperature AFM [55] with light directed to the mixing chamber by means of a single mode fibre directional coupler.

A low-finesse cavity should minimize the magnitude of the optomechanical force acting upon the device. A silicon nitride structure substrate will give a maximum reflectivity of around 0.4 with the untreated fibre face providing a reflectivity of 0.04 which would result in (for the case of a cavity between the fibre and the sample) a finesse of 2.4. In other nanomechanical and optomechanical measurements high-finesse cavities ($\mathcal{F} > 5.5$) were used to optically cool mechanical systems which would influence the mechanical behaviour as seen in the work by Unterrerrithmeier *et al.* [48]. This led to the decision not to treat the tip of the fibre to increase the finesse.

For the highest stability the coherence length of the light can be decreased and the cavity formed within the nanomechanical resonator. A diode laser that could be operated above (to produce coherent light) and below (to produce incoherent light) the lasing threshold was chosen as the optical source for nanomechanical measurements. A

HeNe laser was also available should a longer coherence length be required for two-beam measurements.

3.3 Summary

In this chapter, two of the most commonly used optical arrangements for detecting nanomechanical displacements, the Michelson interferometer and the Fabry-Perot interferometer have been introduced and their operation described. Using multi-layer film theory appropriate substrate film thicknesses were calculated such that the nanomechanical device would have maximum responsivity. A number of optical arrangements used in the study of nanomechanical systems were then reviewed and based on these findings a number of design decisions for the interferometer were made.

Chapter 4

Device Design and Fabrication

This chapter will look at how devices were fabricated from high-stress silicon nitride. In Chapter 2, we saw how devices made from high-stress silicon nitride [18, 20, 29, 30, 33–35] have demonstrated very high quality factors. This is attributed to the high stress of the silicon nitride giving the device a high mechanical stability, which results in high mechanical quality factors [34, 35].

High-stress silicon nitride has been studied extensively at Cornell University [29, 30, 33, 34]. With this in mind the Cornell Nanoscale Science and Technology Facility (CNF) was chosen as the supplier of high-stress silicon nitride grown using LPCVD¹ similar to that studied in [33] with an intrinsic tensile stress of ~ 1.2 GPa.

This chapter will begin by giving a brief overview of the techniques used in the fabrication of these devices, before looking at the substrate from which the devices are fabricated, before moving on to look at the design and fabrication of metallic alignment marks. These are used to aid with the electron-beam lithography steps and to assist with locating devices when using the interferometer. Fabrication methods for two nanomechanical devices, membranes and torsional resonators are then discussed.

Detailed recipes containing processing parameter for all the procedures discussed in this chapter can be found in appendix A.

¹Low-Pressure Chemical Vapour Deposition

4.1 Lithographic Techniques

Lithography is a process whereby a pattern is transferred onto the surface of a wafer. Two types of lithography were used in the course of this work, optical and electron-beam. Both of these techniques transfer the pattern to a radiation sensitive resist. For the sake of clarity and to avoid repetition later in the chapter, the following section gives a brief overview and description of these techniques.

The first step in both techniques is to apply a thin layer of a radiation sensitive resist to the substrate. The resist is supplied in a solvent that is dispensed onto the surface of the substrate. Spinning the substrate at high speed (several thousand rpm) will produce centrifugal forces that cause the resist to flow to the edges of the substrate. Excess resist is expelled from the sample, leaving a uniform film of resist on the substrate. Varying the spin parameters (speed and time) and/or the concentration of resist in the solvent (*i.e.* the viscosity of the resist) allows the resist thickness to be controlled. The solvent remaining in the resist is driven off by baking the resist using either a hot plate or convection oven.

Resists are classified as either positive or negative tone, based on the behaviour of the resist once exposed. For a positive resist, the exposed region becomes soluble in the developer, and will be removed, while for a negative resist the exposed region becomes insoluble in the developer and will remain [56, 57].

Photolithography

Photolithography uses a photomask made of a glass substrate patterned with chrome to block UV radiation to specific regions of a substrate. All areas of the substrate are exposed to the radiation in one go, so the process is ideal for patterning large areas quickly.

In this work the photomask used was patterned using a laser-write system. The manufacturer of the mask² was able to work to a minimum feature size of 5 μm , which

²JD Photo-Tools

placed a lower limit on attainable feature size. The mask is placed in direct contact with the resist and a mercury lamp used to expose the mask and substrate to UV radiation. Light is able to pass through the regions of the photomask where the chrome has been removed, exposing the underlying resist which is then developed [56].

Electron-Beam Lithography

Electron-beam lithography uses a beam of electrons to expose the resist, this allows the patterning of features with smaller dimensions than those achievable with optical lithography. The pattern is defined using a set of deflection coils in the electron column to raster the electron-beam over the surface of the substrate. This serial process, where the pattern is “drawn” onto the resist means exposure times can range from several minutes to several hours for patterns with large exposed areas [56, 57].

The substrate is coated with an electron-sensitive polymer, poly-methyl methacrylate (PMMA). When exposed to a beam of electrons in a scanning electron microscope, breaks in the long polymer chains are caused, resulting in shorter polymer sections that are more soluble in the developer.

The dose (D) specifies the amount of charge absorbed by a specific area of the resist and has units μCcm^{-2} . It is defined in terms of the beam current (I), dwell time (t) and pixel size (l). The beam current is fixed at the start of the exposure, so the dose is controlled by varying the time the beam dwells on each pixel. The dose can be calculated from:

$$D = \frac{It}{l^2} \quad (4.1)$$

For the 495 k PMMA used in this work the manufacturers suggested doses lie in the range $50 - 500 \mu\text{Ccm}^{-2}$. This value is heavily influenced by the substrate on which the exposure is performed due to the fact that the forward scattered electrons do very little damage to the polymer. It is instead the backscattered electrons that cause the majority of the scissions within the polymer.

A by product of the scattering of electrons is the proximity effect. The backscattered

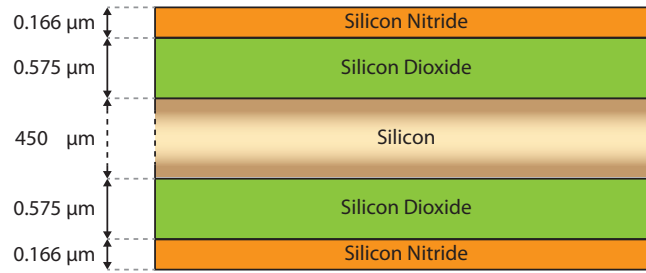


Figure 4.1: Schematic of the multi-layer structure of the substrate from which the nanomechanical devices are fabricated. Figure not to scale.

electrons expose a region larger than the spot size of the electron beam. This effect is cumulative, so must be accounted for when writing patterns with features in close proximity through careful design of the pattern or by tailoring the doses for different regions [57].

4.2 Substrate

The samples were fabricated from 450 μm thick p-type silicon coated on both sides with a 575 nm thick layer of silicon dioxide and a 166 nm thick layer of stoichiometric silicon nitride with an in-built tensile stress of ~ 1.2 GPa. This was supplied in the form of 100 mm diameter wafers. A diagram showing the structure of the substrate is shown in figure 4.1.

The film thicknesses were chosen by applying the multi-layer film calculations discussed in section 3.1.2. The fabrication process requires that the sacrificial layer of silicon dioxide be removed using a wet etch in hydrofluoric acid. As silicon nitride etches slowly in 49 % hydrofluoric acid (~ 15 nm/min compared to ~ 2300 nm/min for thermal oxide [58]) it was necessary to increase the thickness of the nitride layer to allow for this thinning. The wet etch was predicted to take between 3 and 6 minutes, depending on the device being fabricated, resulting in the thickness of the nitride layer being reduced by between 45 and 90 nm. The target nitride thickness was 90 nm, so it was requested

that silicon nitride of thickness 170 nm was deposited on 570 nm of silicon dioxide by CNF to account for this. Upon receipt of the substrates the film thickness was measured using a reflectometer³, giving the dimensions shown in figure 4.1.

4.3 Optical Mask Design

Alignment marks were defined on the substrate using optical lithography and the thermal evaporation of gold. The optical mask shown in figure 4.2(a) was designed to include the following features:

- Global marks for aligning the electron-beam lithography coordinate system to that of the sample, allowing any slight rotation of the sample to be accounted for.
- Local marks⁴ for precise alignment of features written by electron-beam lithography to a 500 μm write field.
- Metallic contacts for attaching a surface mount ruthenium oxide resistor to the sample to act as a thermometer.
- A border defining the area accessible by the nanopositioning stages.

The *global marks*, figure 4.2(b), consist of a cross, with arms of length 250 μm , and width 50 μm . During electron-beam lithography these marks are used to globally align the sample to the coordinate systems of both the scanning electron microscope and the lithography system. This allows any rotation and scaling between these systems to be accounted for.

Once globally aligned, *local marks* are used to precisely position lithographic features within a write field. These marks are placed at the four corners of a device field, allowing

³Ocean Optics USB4000-UV-VIS with a Hammamatsu L10290 High Power UV-Vis Fibre Light Source

⁴Referred to as *chip marks* in the electron-beam lithography software, (ECP package from Xenos GMBH)

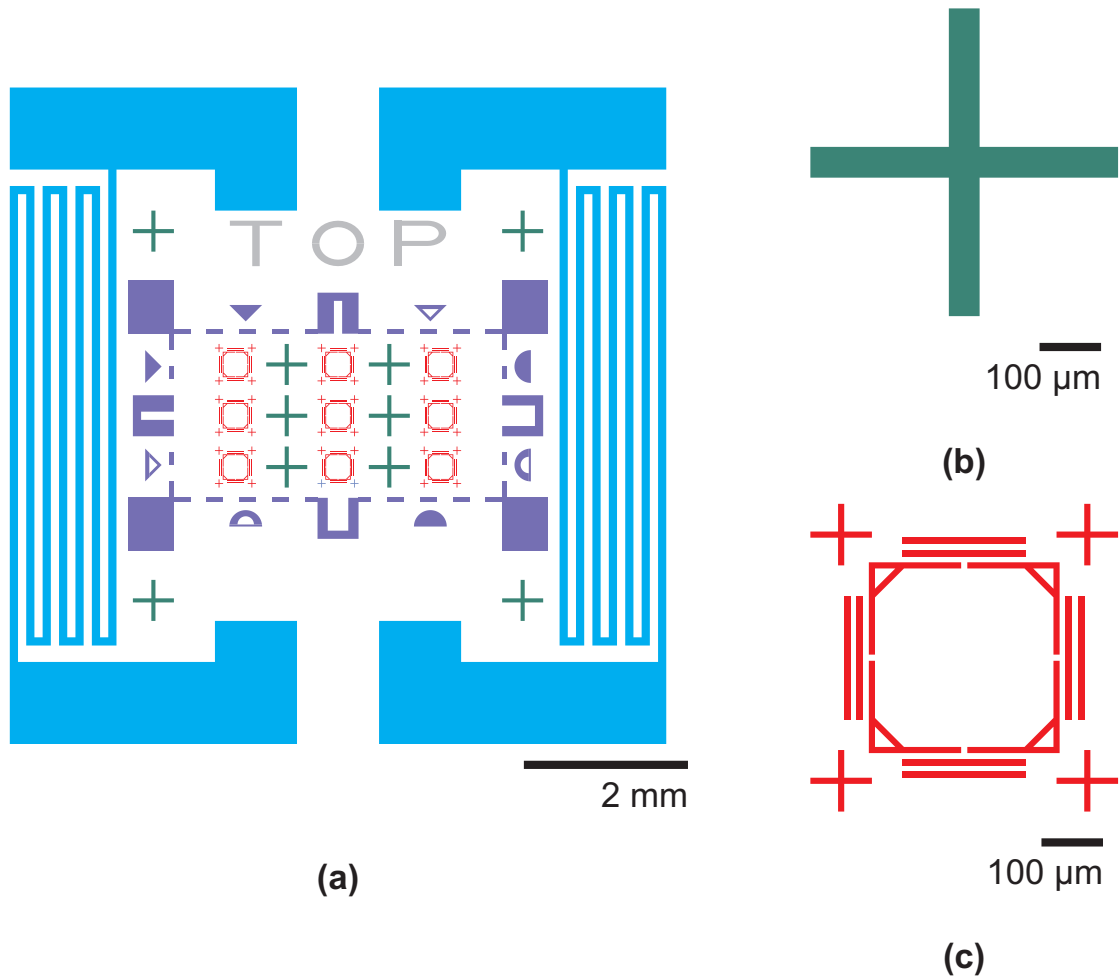


Figure 4.2: Schematic showing the optical mask designed as part of this work. (a) Shows the complete mask including global marks (green), local marks and device fields (orange), thermometry contacts (blue) and scan area border (purple). (b) Shows a global mark used for sample alignment, while (c) shows a device field, surrounded by four local marks, used for precise alignment during electron-beam lithography.

patterning to an accuracy ⁵ better than 50 nm within the box bounding the device field to be achieved.

For the thermometry contacts, it was decided to use a meandering pattern for the metallic contacts for the thermometer. This helped to thermalise the thermometer to the substrate temperature. Pads 3.5 mm by 1.0 mm were defined, spaced to allow a 2.2 k Ω surface mount ruthenium oxide resistor to be attached using conductive epoxy ⁶. These are connected to a second set of pads by a track 100 μm wide and 40 mm long. This second set of pads are used to provide an electrical connection to a resistance bridge. Unfortunately in initial tests it was found that mounting and connecting the thermometer to a resistance bridge was problematic, so in all measurements the thermometer was omitted.

The border defining the edge of the scan region, purple in figure 4.2(a) was originally intended to be used for step size calibration, and as a coarse positioning system for the stages. Upon testing this system was found to be too coarse to be practical. This led to the introduction of the location markers to be discussed in section 4.4.

4.3.1 Optical Mask Processing Steps

Processing steps for defining the pattern using the optical mask are outlined in this section. In depth processing steps can be found in Appendix A.2.

The 100 mm diameter silicon wafer, coated with silicon dioxide and silicon nitride was first scribed into squares 9.8 mm on a side before being solvent cleaned (ethyl lactate, acetone, methanol and isopropyl alcohol (IPA)), with ultrasonic agitation. Once cleaned the samples were dehydrated in a convection oven.

After cooling the samples were spin coated with a 1.4 μm thick layer of AZ5214E photoresist ⁷ and baked before being soaked in toluene to toughen the resist and avoid

⁵for a 500 μm write field

⁶Epotek H20E-PFC

⁷AZ5124E photoresist from Clariant (supplied by MicroChemicals) is an image reversal resist, which by varying the processing parameters can be used in positive or negative tone. In this work it is processed to behave as a positive resist.

overdeveloping after exposure. The resist was then exposed to UV radiation using an optical mask aligner before being developed.

Any traces of resist remaining in the exposed regions were removed in an oxygen descum step. This is important as hydrofluoric acid readily attacks photoresists and, as was seen in early tests, can cause metallic layers to lift off if the substrate is not properly descummed. To improve adhesion between the metal and the substrate a reactive ion etch in CHF_3 was used to roughen the top surface of the silicon nitride and provide a better surface for the metal to adhere to.

The pattern defined in the resist is transferred to the sample by thermally evaporating a 50 nm layer of gold. Titanium is normally used as an adhesion layer for gold, however it is also etched by hydrofluoric acid. This led to a 5 nm layer of chrome, which is only very slowly etched by hydrofluoric acid [58], being used as the adhesion layer.

Once deposited, the unwanted metal is lifted off by soaking in warm acetone or NMP-based resist stripper⁸, with ultrasonic agitation if required. This removes any gold that has a layer of resist beneath it, leaving the metal deposited in the exposed regions intact.

4.4 Location Markers

When a sample is imaged on the interferometer, a picture is built up pixel by pixel. This can make finding and positioning the optical spot on a nanomechanical device a time consuming and frustrating task. In order to simplify this a set of marks were designed to allow the location on the sample to be determined and the positioning stage step size calibrated.

Initially the location of the spot on the sample was to be determined using the border defining the scan region, however during initial tests it was found that due to the unreliability of the positioning stages over large distances this system was too coarse to be practical. Following on from this a set of markers were designed that would allow the location of the spot on the surface to be determined to within a few hundred microns.

⁸Microposit Remover 1165

The marks were designed to be imaged quickly (< 20 minutes) by the interferometer, which limited the size of one unit of the pattern to a field $\sim 50 \mu\text{m}$ on a side. For this reason, the letters and numbers were made $5 \mu\text{m}$ in width and height, giving a repeating pattern $15 \times 15 \mu\text{m}$. For a $5 \mu\text{m}$ character the minimum feature size would be less than a micron and at these dimensions optical lithography would struggle to produce these features [56], so it was decided to define the location markers using electron-beam lithography.

These marks divide the scan field accessible to the nano-positioning stages into 11 columns (labeled A to K) and 7 rows (labelled 1 to 7). Into each of these cells a repeating pattern consisting of a letter denoting the column, a number denoting the row, and two $2.55 \mu\text{m}$ squares was defined. The labelling system, and an example of the location markers is shown in figure 4.3. A similar approach was taken with the labelling of the individual device fields, which were labelled from R to Z, along with numbers indicating the position of the optical spot within the field.

Once defined the patterns are transferred onto the sample by evaporating a thin film of metal. Alternatively the marks can be defined using a reactive ion etch, this can however expose the oxide layer, which will be attacked by the hydrofluoric acid during the wet etch step. As such this method can only be used to define the marks after the wet etch has been carried out, for example in the case of torsional resonators fabricated via an intermediate membrane discussed in section 4.5.2.

4.4.1 Location Marker Processing Steps

Location markers were patterned using an electron-beam lithography system⁹. A 450 nm thick layer of poly-methyl methacrylate (PMMA), an electron sensitive resist was spun onto the substrate before being patterned with location markers in a scanning electron microscope. The global marks were used to align the location marker cells

⁹Lithography system comprised an XPG2 high-speed writer from XENOS Semiconductor Technologies GmbH mounted on a JEOL FEI Scanning Electron Microscope with a maximum acceleration voltage of 30 kV

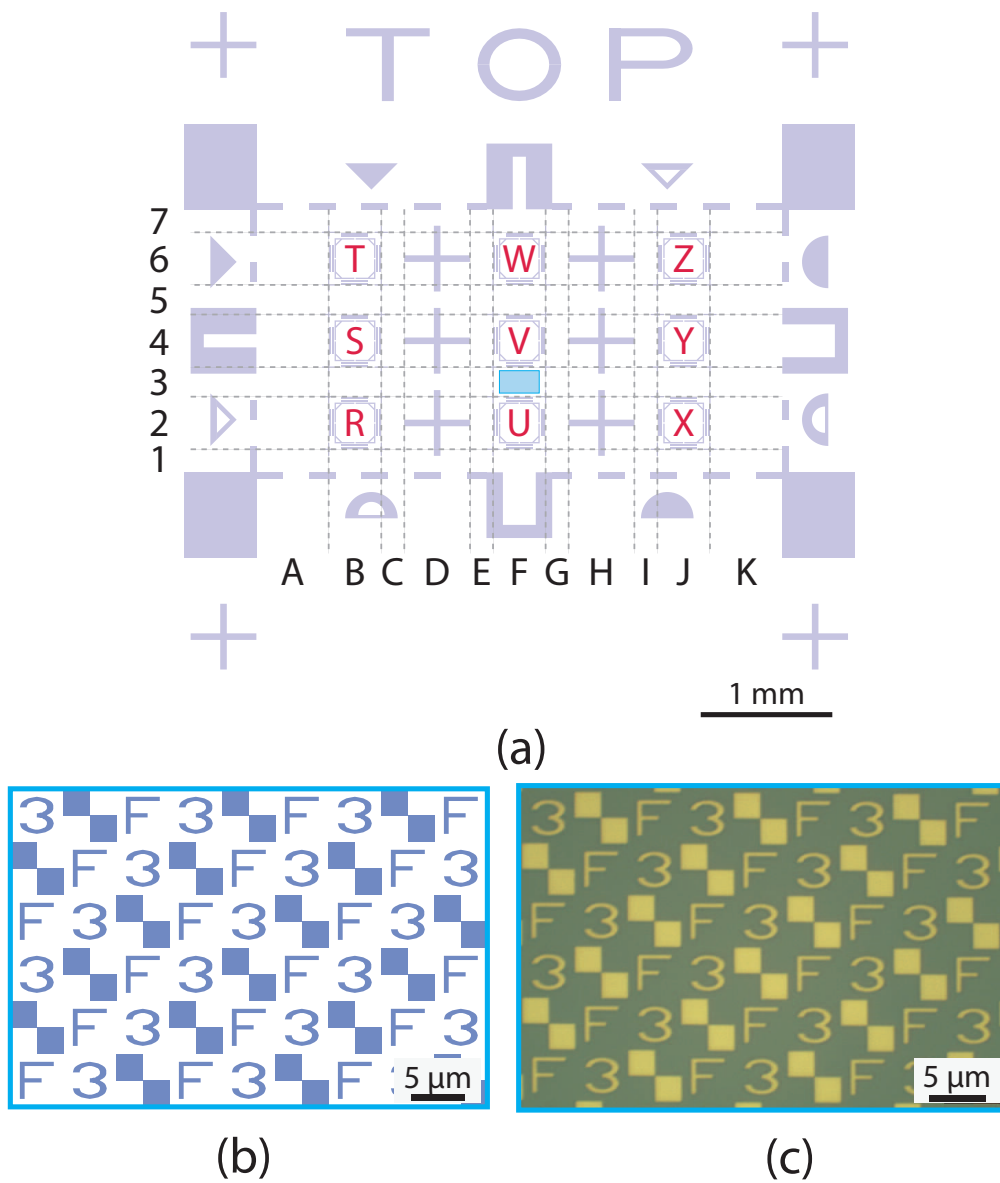


Figure 4.3: The location markers used for coarse positioning of the sample beneath the interferometer. (a) Shows a schematic showing the labeling system used to determine the sample location, the region in the blue box is enlarged in (b) where the design of the individual location markers is shown alongside an optical microscope image, (c), of a set of location markers metalised with 50 nm of gold.

to the substrate. For the device field markers, local marks were also used for precise alignment to the device fields.

After development the exposed regions are descummed and etched as discussed in section 4.4 and a 50 nm layer of gold deposited.

4.5 Nanomechanical Device Fabrication

The following sections give an overview of the processes employed to fabricate the nanomechanical devices, with step-by-step fabrication recipes (including processing parameters) given in Appendix A.4.

4.5.1 Membranes

Membranes, thin sheets of silicon nitride clamped around their perimeter were fabricated using a combination of electron-beam lithography, reactive-ion etching and wet etching. The complete process is shown in figure 4.4, and is similar to that used by Southworth *et al.* [33]. A detailed description of the processing parameters appear in Appendix A.4.1.

A silicon substrate coated with a 570 nm thick layer of thermally grown silicon dioxide and 170 nm of high stress silicon nitride is first cleaned before coating with a 450 nm thick layer of 495k PMMA, as shown in figure 4.4(a). Electron-beam lithography is used to pattern the resist with an array of circular holes of diameter $\sim 0.8 \mu\text{m}$.

For a square membrane, holes are patterned on a $5 \mu\text{m}$ pitch square array, as shown in figure 4.5(a). A circular membrane requires they be arranged radially about a central hole in rings spaced by $5 \mu\text{m}$. In order to maintain the separation of approximately $5 \mu\text{m}$ between holes, the first ring ($n = 1$) contains 6 dots (60° separation), with consecutive rings containing $n \times 6$ holes. An example of these holes patterned in PMMA can be seen in the optical microscope image in figure 4.6(a).

Once developed the PMMA is used as an etch mask and the holes transferred into

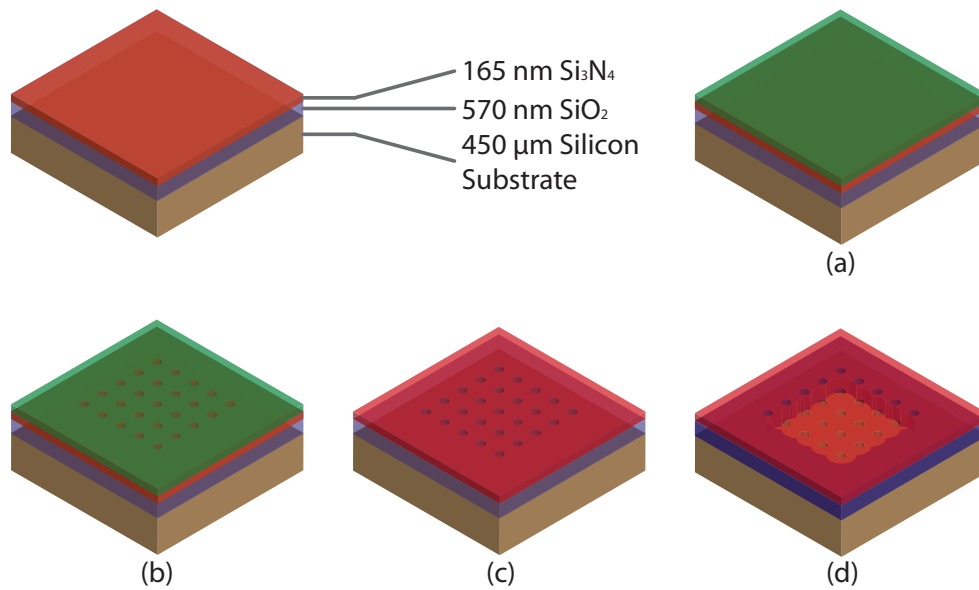


Figure 4.4: Fabrication process for silicon nitride membranes. (a) The substrate is coated with a layer of PMMA (b) into which an array of $0.8 \mu\text{m}$ holes is patterned using electron-beam lithography. (c) The exposed pattern is developed and transferred into the nitride using a CHF_3 -based reactive ion etch to expose the underlying oxide. (d) The oxide is wet etched using 49% hydrofluoric acid to produce an undercut of the silicon nitride layer and suspend the membrane.

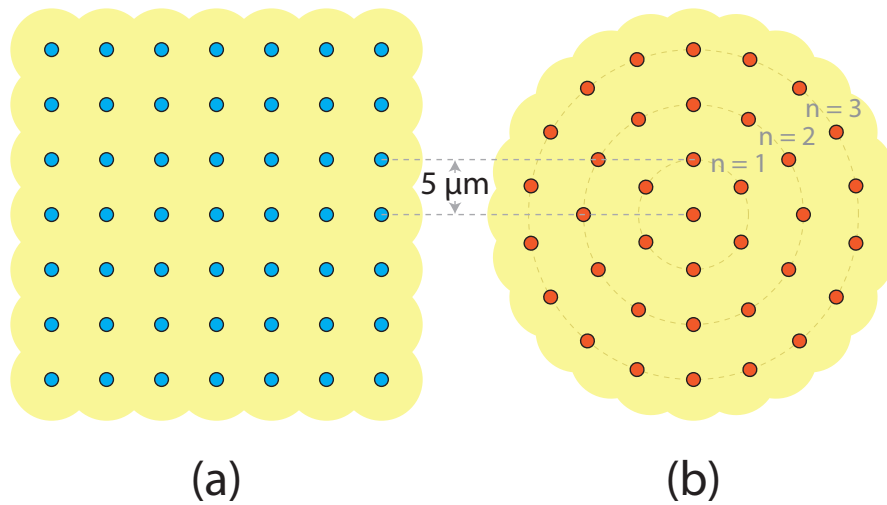


Figure 4.5: Locations of dots patterned into the PMMA for (a) a square membrane and (b) a circular membrane. The yellow region indicates the extent to which the wet etch undercuts the nitride layer to suspend the membrane.

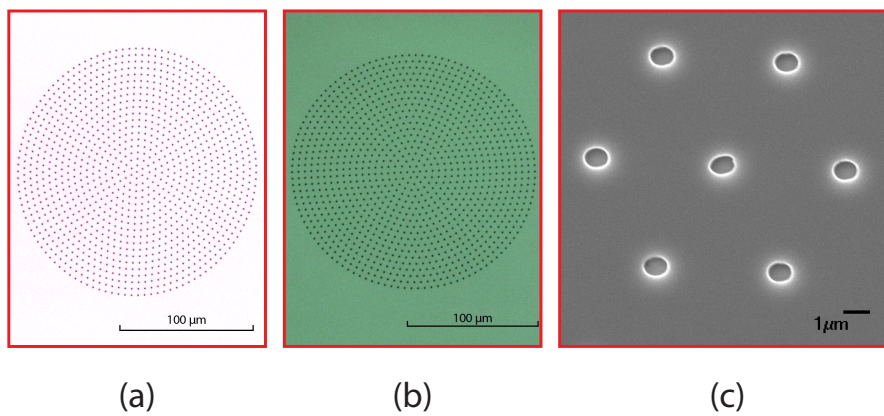


Figure 4.6: Images showing stages in the fabrication of a circular membrane, with a diameter of $200 \mu\text{m}$. (a) Shows a PMMA layer, patterned with a radial array of $\sim 0.8 \mu\text{m}$ diameter holes, in (b) this pattern of holes has been transferred into the silicon nitride layer using a reactive ion etch. (c) Shows a close up scanning electron microscope image of the holes at the centre of the membrane.

the silicon nitride using a reactive ion etch¹⁰ in CHF_3/O_2 . This etches through the silicon nitride, exposing the underlying silicon dioxide. These holes can be seen in figure 4.6(b-c) for a circular membrane.

The silicon dioxide acts as a sacrificial layer. Wet etching in concentrated hydrofluoric acid removes the oxide layer, undercutting and suspending the membrane, as shown in figure 4.4(d). In concentrated hydrofluoric acid the etch rate of silicon dioxide is ~ 1200 nm/min [58]. The holes through the silicon nitride limit the access of the acid to the oxide layer, reducing the lateral etch rate of the oxide to between 600 and 1000 nm/min. This resulted in a wet etch time of between 3 and 6 minutes. The hydrofluoric acid was measured to etch the silicon nitride layer at around 15 nm/min, which would result in a thinning of the nitride by a maximum of 90 nm, which was accounted for in the design of the multi-layer structure of the substrate as discussed in sections 3.1.2 and 4.2. Accurate thickness measurements of a suspended membrane were made by removing the membrane using a sheet of PDMS, and are discussed in section 4.5.1.

During the wet etch the silicon dioxide behind the nitride layer will have been removed and the resulting volume behind the membrane filled with a liquid. Initially this would be hydrofluoric acid, but ultimately, after the sample is rinsed, this will be replaced with water. If the membranes were dried at this stage, the surface tension of the water would be enough to pull the membrane down and cause stiction between membrane and substrate, collapsing the membrane. It is sometimes possible to overcome issues of stiction by placing the sample into a solvent (commonly methanol) with a lower surface tension than that of water and blow drying in dry nitrogen gas. While this will work for membranes up to ~ 50 μm in diameter, above this the evaporating liquid is able to stretch the membrane sufficiently that it will touch and stick to the silicon substrate. To avoid this the water is replaced with isopropyl alcohol and a critical point drier used.

Critical point drying uses liquid carbon dioxide as a transitional fluid in the drying process. The phase diagram of carbon dioxide is shown in figure 4.7. The sample (immersed in alcohol) is placed in a sealed chamber. The chamber is then filled with

¹⁰Corial 200IL RIE system

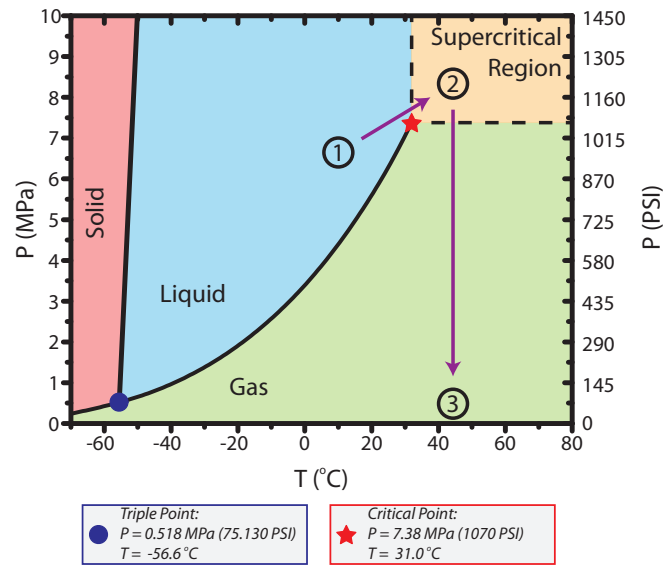


Figure 4.7: Phase diagram of carbon dioxide showing the path taken during a critical point drying process. (1) The chamber containing the sample, immersed in alcohol is purged with liquid carbon dioxide and sealed. (2) The temperature of the chamber is increased, causing the carbon dioxide to move from the liquid to the supercritical phase. (3) The pressure is isothermally reduced allowing the carbon dioxide to return to the gas phase avoiding the liquid-gas phase boundary. Data used to generate this phase diagram from [59, Chap. 6, pp 36-37].

liquid carbon dioxide at ~ 1000 PSI into which the alcohol dissolves (point 1 in figure 4.7). Fresh carbon dioxide is flowed through the chamber, removing the alcohol and leaving the sample immersed purely in liquid carbon dioxide. If the chamber is now sealed and the temperature raised the carbon dioxide will pass from the liquid to the supercritical phase (point 2 in figure 4.7). By isothermally reducing the pressure, the carbon dioxide can return from a supercritical fluid to a gas (point 3 in figure 4.7). This phase transition from supercritical to gaseous has zero surface tension and allows the membrane to dry without collapsing due to the forces associated with the surface tension [22].

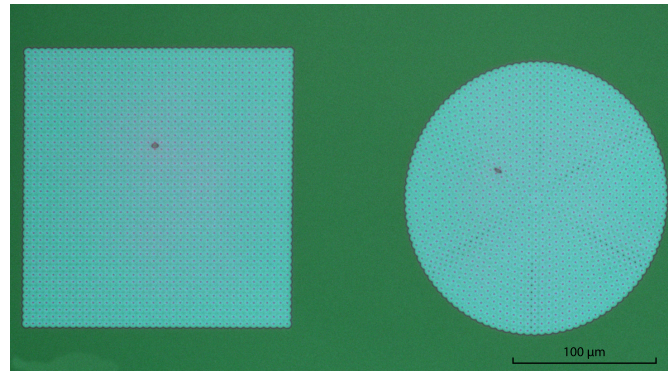


Figure 4.8: Optical image of a square membrane with sides $L = 200 \mu\text{m}$ and a circular membrane of diameter $200 \mu\text{m}$.

Critical point drying is the final stage in the fabrication process. Optical images of complete $200 \mu\text{m}$ membranes can be seen in figure 4.8. Scanning electron microscope images are not shown, as due to the dielectric nature of the silicon nitride charge will accumulate on the membrane. This charge, combined with the large dimensions causes the membrane to be attracted to and stick to the underlying substrate. For smaller devices this charging is not such an issue.

Membrane Thickness Measurements

In order to determine the final thickness of the membrane, an approach similar to that employed by Adiga *et al.* [30] was used. A sheet of polydimethylsiloxane (PDMS)¹¹ was used to peel off the membrane, allowing the back surface topography and thickness of the membrane to be measured using an AFM and a surface profiler.

PDMS is a silicone compound, widely used in nano-imprint lithography and micro- and nano-fluidics; it is a transparent, chemically inert compound, that when applied to a surface will take on the topography of the surface without leaving a chemical residue behind [60]. PDMS is supplied as a two part resin that was cured in a convection oven

¹¹Dow Corning Sylgard 184 Silicone Elastomer

at 150 °C for 2 hours to give a sheet of PDMS \sim 8 mm thick.

To promote adhesion between the PDMS and silicon nitride the surfaces can be activated using an oxygen plasma to create covalent siloxane bonds [61, 62]. If one (or both) of these activated surfaces are brought into contact, bonds will form between the silicon nitride membrane and the PDMS and upon separation the membranes will be removed with the PDMS.

This procedure was carried out by exposing the silicon nitride membrane to a 60 second oxygen plasma before placing the two surfaces together for 60 seconds before peeling them apart. This process worked to remove the silicon nitride membranes from the sample, which could then be imaged using an AFM. Images taken using this technique for a drum and rectangular membrane are shown in figures 4.9 and 4.10 respectively. It is important that only the silicon nitride surface be activated as in earlier trials with both surfaces activated the siloxane bonds on the surface of the PDMS were able to interact with the silicon in the AFM cantilever used to image the sample¹². This interaction interfered with the z-control of the microscope and prevented imaging.

The limited access offered by the holes etched through the silicon nitride means that the majority of wet etching occurs on the front surface of the membrane. On the back of the membrane a honeycomb structure formed as can be seen in figures 4.9(e) and 4.10(d) which show the topography of the back surface of the membrane and that the silicon nitride layer has thinned from a thickness of 165 nm to around 100 nm. Surface profiling¹³ carried out on several of the holes left where a membrane was removed showed a step height of 700 nm at the edge of the membrane. This change in height is composed of 575 nm of silicon dioxide and 125 nm of silicon nitride, equating to 40 nm of silicon nitride removed from the front surface, with a maximum of 25 nm removed from the back surface. The AFM images of the back of the nitride membranes reveal a change in height between etch holes of \sim 20 nm and a membrane thickness of 100-125 nm.

¹²Bruker TESP cantilever

¹³KLA Tencor Alpha-Step D-120

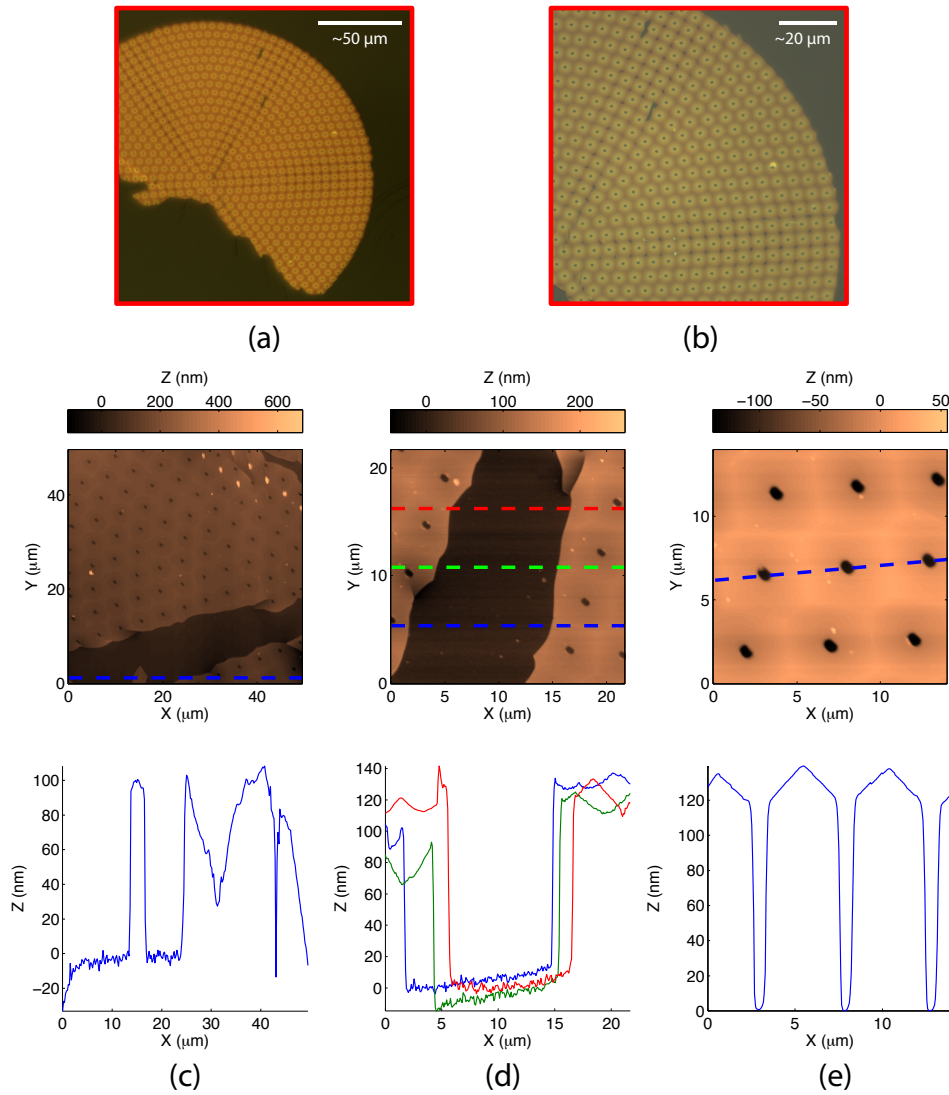


Figure 4.9: Optical and atomic force microscope images of the back surface of a silicon nitride drum membrane peeled from the substrate using a sheet of PDMS. (a) and (b) show optical images of the membrane on PDMS at (a) $50\times$ and (b) $100\times$ magnification. Images (c)-(e) show AFM images of the back surface topography, taken using a Veeco Dimension V AFM at (c) 50 , (d) 25 and (e) $16\ \mu\text{m}$ fields. The lower plots show sections through the topography at the locations indicated by the dashed lines.

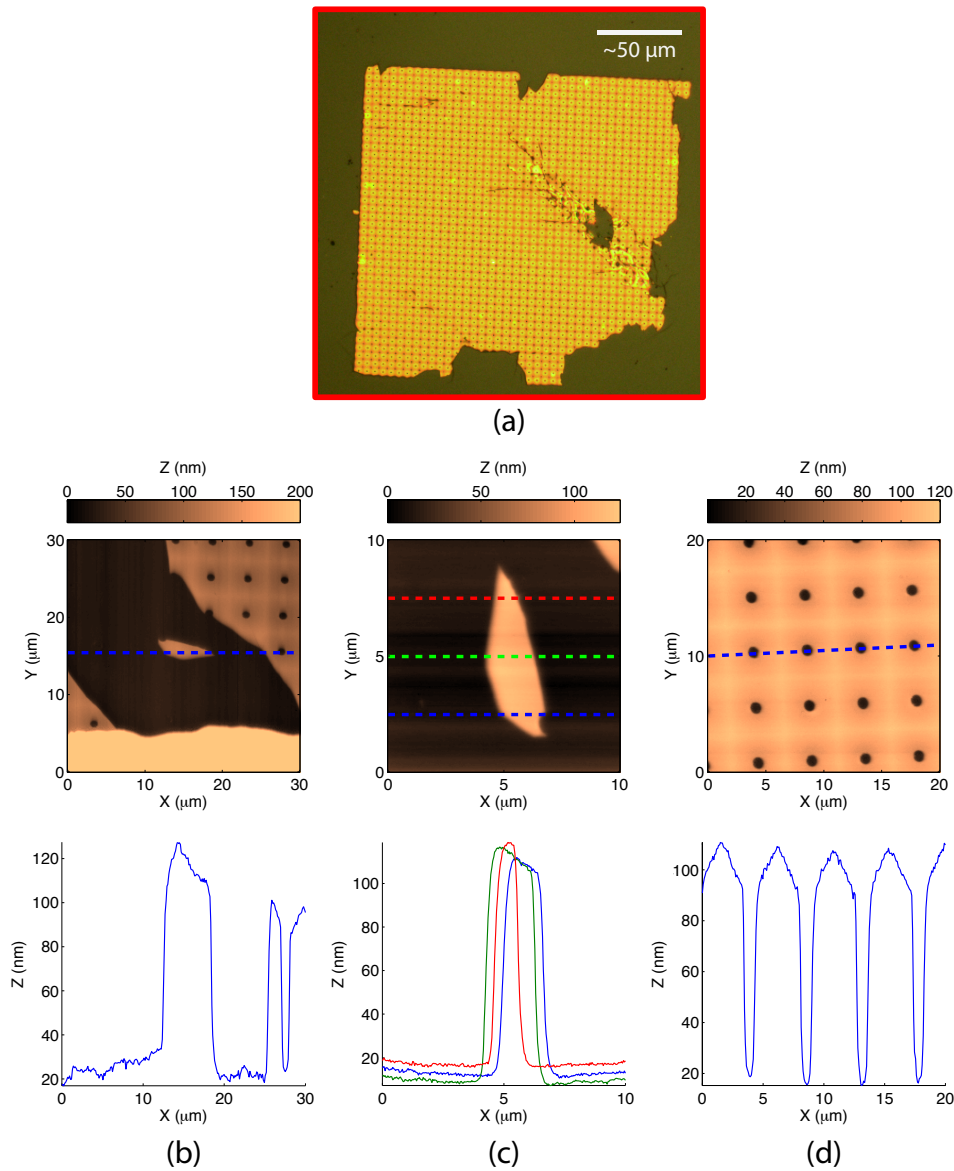


Figure 4.10: Optical and atomic force microscope images of the back surface of a rectangular silicon nitride membrane peeled from the substrate using a sheet of PDMS. (a) shows an optical microscope image of the membrane on PDMS at $20\times$ magnification. Images (b)-(d) show AFM images of the back surface topography, taken using an Asylum Research MFP-3D AFM at (b) 30, (c) 10 and (d) 20 μm fields. The lower plots show sections through the topography at the locations indicated by the dashed lines.

Direct Fabrication of Torsional Resonators

This method allows the direct fabrication of torsional resonators with only one stage of electron-beam lithography. This process is shown in figure 4.12.

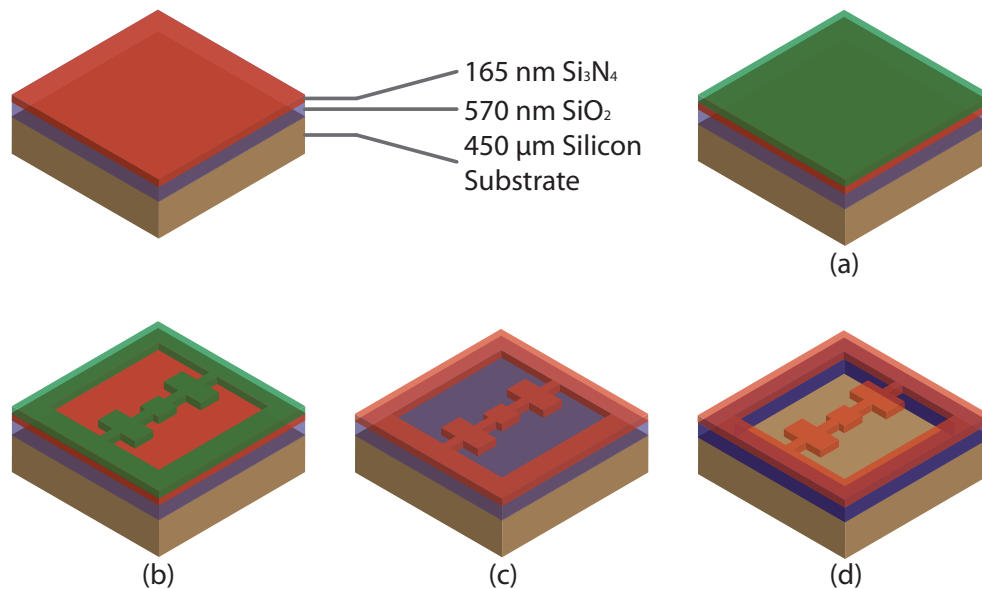


Figure 4.12: Fabrication process for high-stress silicon nitride torsional resonators using one electron-beam lithography step. (a) The substrate is first coated with a layer of PMMA. (b) Into this layer the resonator pattern is exposed using electron-beam lithography. (c) The exposed pattern is transferred into the nitride using an CHF₃ reactive ion etch to expose the underlying oxide. (d) A wet etch in 49% HF removes the silicon dioxide below the device, releasing it.

A 200 nm thick layer of electron sensitive resist, PMMA, is spun onto the substrate and patterned at 30 kV with the negative pattern of the resonator, *i.e.* after developing, a PMMA etch mask in the shape of the resonator remains on the silicon nitride. The exposure map used to pattern a PMMA etch mask is shown in figure 4.13(a), when an area is exposed part of the exposure occurs due to the incoming electrons, with a second contribution arising from the scattered electrons (the proximity effect). For a larger area

the contribution due to the proximity effect will be larger and as a result a lower dose is needed. This can be seen in the exposure map shown in figure 4.13(a) where the cutouts in the outer torsional paddle require a larger dose to ensure that the exposure is to the same extent. An AFM image of one of these PMMA masks patterned in this manner is shown in figure 4.13(b).

This pattern is then transferred into the silicon nitride using a reactive ion etch in CHF_3 , exposing the silicon dioxide layer. The exposed silicon dioxide and the region underlying the resonator can then be removed using a wet etch in 49 % hydrofluoric acid. After rinsing in water and transferring to methanol the resonator is dried using nitrogen gas. The smaller dimensions of the devices and larger areas through which the solvent can evaporate mean that stiction does not pose a problem for these devices.

Figure 4.14 shows images of a torsional resonator fabricated using this method.

Indirect Fabrication of Torsional Resonators via an Intermediate Membrane Step

In the previous section the resonator was patterned directly into the nitride and a wet etch used to remove the silicon dioxide beneath the paddles. This increases the wet etch time, which in addition to releasing the resonator also undercuts the clamping points where the resonator connects to the substrate, leading to an increase in clamping losses. To minimise these losses, torsional resonators were fabricated using the process described below and shown in figure 4.15.

The substrate was first coated with a 200 nm thick layer of PMMA electron-beam resist (figure 4.15(a)). Using a 30 kV electron beam the PMMA was then patterned with four $0.8 \mu\text{m}$ holes on a $6 \times 4 \mu\text{m}$ square (figure 4.15(b)). A CHF_3 reactive ion etch was used to etch down through the nitride, with the PMMA acting as the etch mask (figure 4.15(c)).

The holes etched through the silicon nitride provide access for 49 % hydrofluoric acid

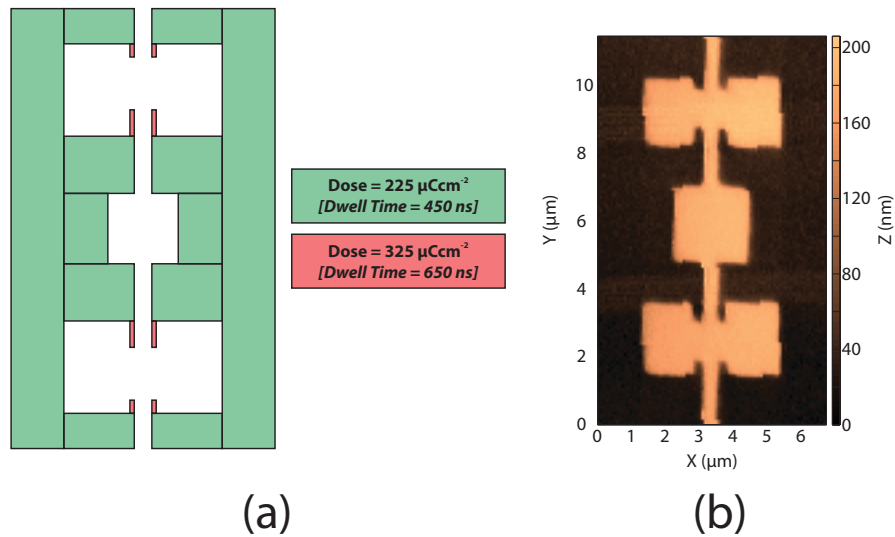


Figure 4.13: Exposure map for a torsional resonator. (a) Shows the pattern used to define a torsional resonator etch mask in PMMA. The different colours denote different doses. Larger areas (green) are written with a lower dose, and the cumulative exposure due to proximity effect ensures sufficient exposure. For the isolated regions (red) a higher dose is needed to ensure sufficient exposure occurs. (b) An AFM image taken using an Asylum Research MFP-3D AFM showing the resist profile obtained from this exposure. The higher (lighter) regions are PMMA, while the lower (darker) regions are the silicon nitride substrate.

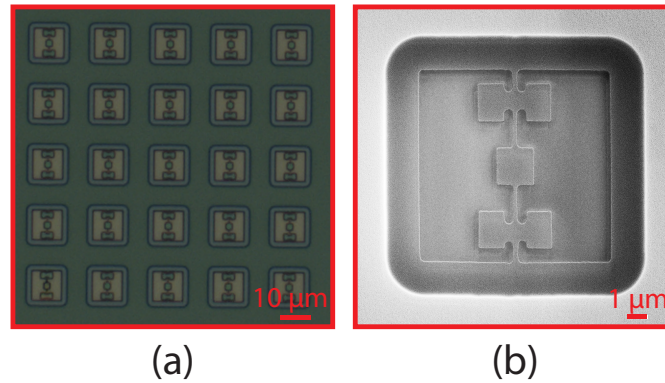


Figure 4.14: Microscope images of the final devices made using the direct method. (a) Shows an optical microscope image of an array of torsional resonators, while (b) shows an SEM image of a single resonator.

to the sacrificial layer of silicon dioxide. Once the oxide layer is removed a membrane remains onto which the resonator can be patterned (figure 4.15(d)). Due to the high-stress within the nitride stiction does not prove to be a problem, allowing the sample to be transferred to methanol after the wet etch and blow dried with nitrogen.

The membrane can now be coated with a new 200 nm thick layer of PMMA (figure 4.15(e)), which is patterned using electron-beam lithography (figure 4.15(f)). A second CHF_3 reactive ion etch then releases the resonator (figure 4.15(f)). Any residual PMMA can be removed using an O_2 barrel asher. Microscope images of torsional resonators fabricated using the indirect method are shown in figure 4.16.

Comparison of Torsional Resonator Fabrication Methods

Torsional resonators were fabricated using both the methods outlined. In figure 4.17 we reproduce the SEM images of the resonators shown earlier, with suspended regions of silicon nitride highlighted in green. From figure 4.17(a) we see a large undercut around the edge of the resonator. This suspended apron will serve to increase clamping losses within the flexural modes of the resonator. In contrast the clamping points in

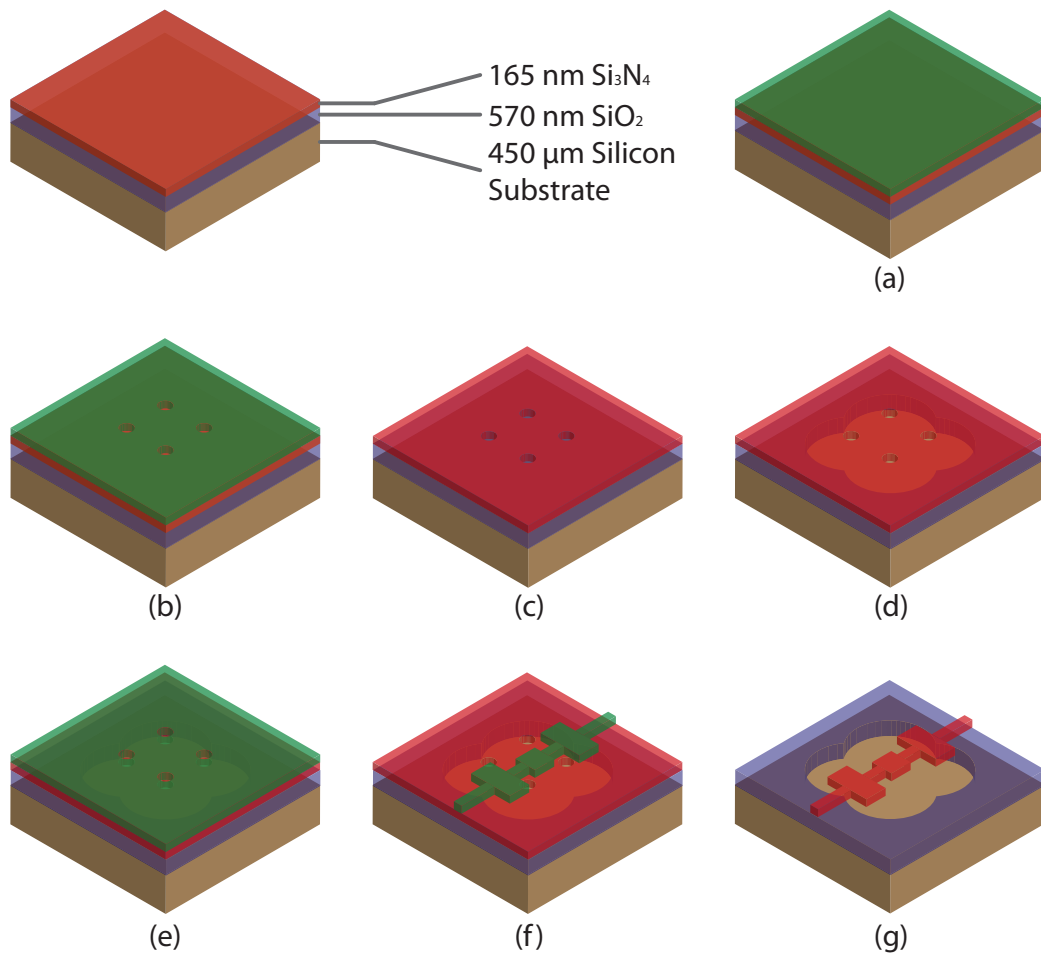


Figure 4.15: Fabrication process for high-stress silicon nitride torsional resonators using two electron-beam lithography steps. (a) The substrate is first coated with a layer of PMMA. (b) An array of $0.8 \mu\text{m}$ diameter holes are then patterned into the resist. (c) The holes are transferred into the nitride using an CHF_3 reactive ion etch to expose the underlying oxide. (d) A wet etch in 49% HF removes the silicon dioxide beneath the holes, forming a membrane. (e) This membrane is then coated with electron-beam resist. (d) This is patterned to leave an etch mask in the shape of the torsional resonator. (e) A second reactive ion etch is then used to remove the unwanted silicon nitride, leaving a suspended resonator.

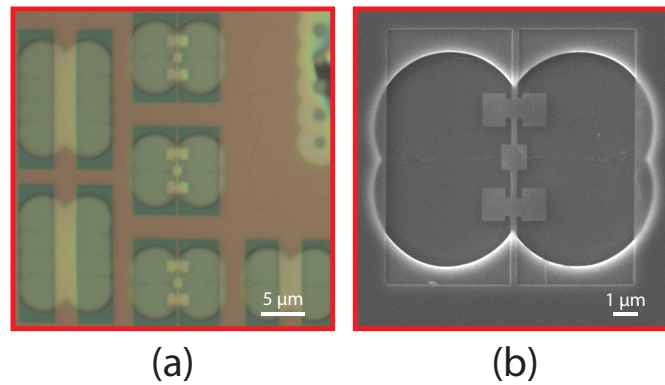


Figure 4.16: Microscope images of the final devices made using the indirect method. (a) Shows an optical microscope image at $100\times$ magnification of 3 torsional resonators (also shown are doubly clamped beams, one of length $6\ \mu\text{m}$ and two $11\ \mu\text{m}$ long), while (b) shows an SEM image of a single resonator.

figure 4.17(b) are far cleaner, only contacting the substrate at the edge of the membrane formed earlier in the process.

Another advantage of this process lies in the fact that by carrying out the wet etch step before defining the resonator it is possible to include a ferromagnetic layer in the resonator. An additional electron-beam lithography step can then be used to pattern a $1\ \mu\text{m}$ dot on the central pad of the torsional resonator. A multilayer structure of cobalt and platinum that can be magnetised in the out of plane direction [63]. By magnetising the dot in the out of plane direction it is then possible to actuate the torsional modes of the resonator by placing it near an rf coil, in a process similar to that used in references [25, 27], this is advantageous as the piezoelectric actuator will preferentially excite the flexural modes.

4.6 Summary

In this chapter the fabrication methods used in this work were introduced. We initially dealt with the design and processing of an optical mask to aid with the fabrication

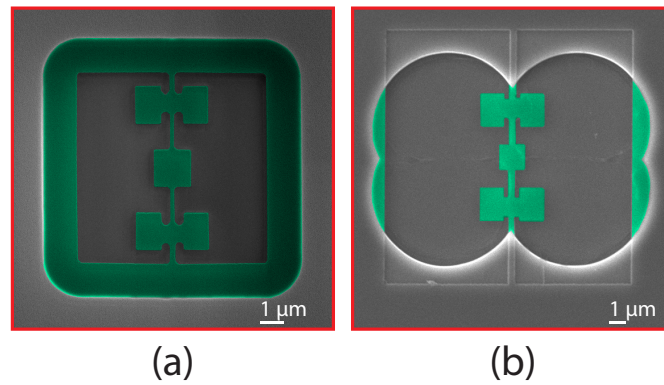


Figure 4.17: Scanning electron microscope images of torsional resonators made using the two methods discussed in this section. (a) Shows a resonator fabricated using one stage of electron-beam lithography, while (b) shows a torsional resonator fabricated with two stages of electron-beam lithography and an intermediate membrane step. Suspended regions of silicon nitride are highlighted in green.

of nanomechanical devices, before moving on to look at how a set of markers were designed to simplify the procedure of locating devices using the interferometer. The latter half of the chapter concerned itself with the fabrication of nanomechanical devices (membranes and three-paddle torsional resonators) from high-stress silicon nitride and the considerations that had to be taken into account when defining these processes. Full processing recipes can be found in Appendix A.

Chapter 5

Experimental Setup

A fibre interferometer that is mounted on a dilution refrigerator capable of measuring the motion of nanomechanical resonators to temperatures below 1 K has been designed and constructed. This system is described in this chapter, which focuses on the experimental design considerations, operating principles, control electronics and measurement techniques. A selection of preliminary measurements are presented to demonstrate the behaviour of the system.

5.1 Operating Principle

A schematic diagram showing the arrangement of the interferometer is shown in figure 5.1. The centre of the optical setup is a 3 dB single mode fibre coupler¹ with a numerical aperture of 0.12. Light is coupled into arm I1 of the fibre and equally split across the two output arms, O1 which runs to the sample at the base of the dilution refrigerator and O2 which is used to monitor the optical irradiance at the sample.

In order for fibre O1 to reach the sample space the coupler is specially manufactured so that O1 is 10 m in length (as opposed to ~ 1 m for I1, I2 and O2). Light directed to the sample space exits the fibre in a cone, which is collimated and refocussed to a spot

¹GOULD Industries

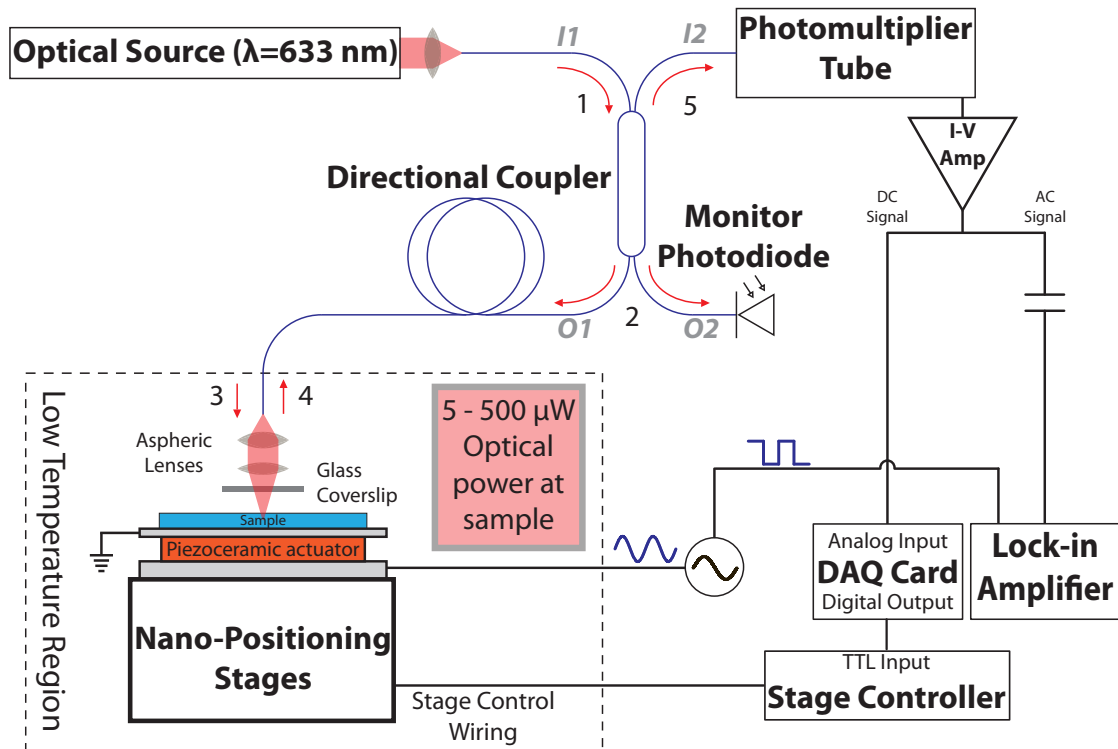


Figure 5.1: Experimental setup of the fibre interferometer. (1) Light is coupled into port I1 of a 3 dB directional coupler which splits the light equally across the two output arms. (2) The optical irradiance of the sample is monitored using the photodiode attached to port O2. (3) Light is directed to the sample by port O2 and upon exiting the fibre is collimated and focussed onto the sample using a set of aspheric lenses. (4) Light reflected from the sample passes back through the aspheric lenses and is recaptured by the fibre. (5) On passing back through the directional coupler the light is monitored by the photomultiplier on port I2, with an IV converter passing a voltage to the detection electronics.

on the sample surface using a pair of aspheric lenses. Positioning of the sample beneath the optical spot is achieved via a set of xyz-positioning stages². Actuation of the device is achieved by mounting the sample on a piezoelectric shaker.

Light reflected from the sample passes back through the aspheric lenses and is recaptured by the single mode fibre. Upon passing through the directional coupler the reflected optical power is split across arms I1 and I2. The optical power exiting I2 is monitored using a photomultiplier tube. A transimpedance amplifier is used to convert the photocurrent to a voltage, the dc component of which is monitored using a DAQ card while the ac component is detected using a lock-in amplifier synchronised to the drive frequency.

5.2 Low Temperature Considerations

The fibre interferometer was installed below the mixing chamber of a commercially available dilution refrigerator³. Figure 5.2 shows the placement of the components comprising the fibre interferometer within the cryostat.

The sample space of the dilution refrigerator is isolated from the main bath of the cryostat by an inner vacuum can. In order to achieve the lowest temperatures allowed by the system a mixture of ^3He and ^4He is condensed into the fridge using the 1K pot. Liquid ^4He is drawn into the pot via a capillary connected to the main bath by a needle valve. Pumping on this ^4He using a rotary pump allows the pot to reach a temperature of around 1K through evaporative cooling.

Incoming $^3\text{He}/^4\text{He}$ mixture is cooled by the pot and condenses through a flow impedance into the mixing chamber. Here a phase boundary forms between a ^3He rich (upper) and a ^3He poor (lower) layer. Cooling is achieved by pumping ^3He across this boundary and into the lower layer which is mainly superfluid ^4He through which the ^3He passes with very little impedance. The superfluid ^4He layer acts as a volume

²Supplied by Attocube Systems AG.

³Oxford Instruments Kelvinox 100

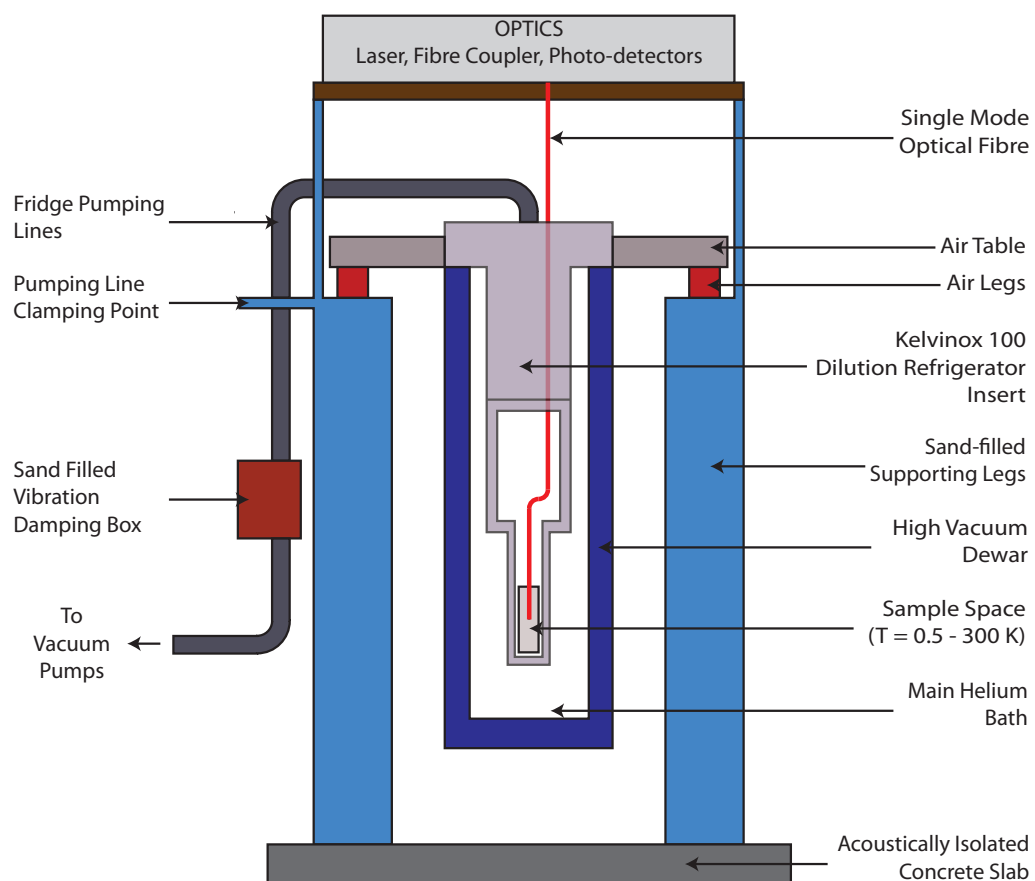


Figure 5.2: Schematic showing the positioning of the interferometer within the cryostat.

into which the ^3He is able to expand. This expansion leads to a change in entropy which in turn leads to cooling. To continually cool the fridge the removed ^3He is recondensed back into the mixing chamber by the 1K pot [64].

The dilution unit sits within the vacuum of the IVC, with the interferometer mounted below the mixing chamber. Thermal coupling to the fridge is achieved by means of three copper rods bolted directly to the mixing chamber.

The single mode fibre enters the IVC through a flange on the top plate that is sealed with wax. The fibre runs down the cryostat, with excess fibre being coiled around the still. This allows the tip of the fibre within the interferometer to be replaced without having to continually remake the wax seal to the IVC.

Unfortunately the operation of the fridge was beset by technical problems that prevented it from cooling. Over the course of this work attempts were made to identify and remedy these issues, unfortunately it was not possible to operate the fridge at a temperature below 1 K for any great length of time.

5.2.1 Wiring Considerations

Electrical signals within the experiment can be divided into three groups with different requirements:

1. ac signals applied to or received from the sample
2. dc signals used for thermometry, heaters and dc sample measurements
3. control voltages to drive the nan positioning stages.

The design of these wiring systems is discussed in the following sections. It was decided early in the design process that the fridge should be wired to allow a range of experiments to be carried out, as such extra wiring was included in the fridge.

High Frequency Wiring

Semi-rigid coaxial cables, with a cupronickel shield were used for ac signals. To allow for future experiments four lines were installed, with fixed 50Ω attenuators⁴, the values of which are shown in table 5.1. These were used to heat sink and thermally isolate the core at the 4.2 K plate, cold plate and mixing chamber. The shield of these attenuators were thermally linked to the fridge using copper speaker wire soldered in place and bolted onto the fridge with a high-pressure joint⁵.

The shields of the coaxial cables were also thermally linked to the fridge using copper speaker wire at the two intermediate stages, the 1 K pot and the still. One line was left without attenuation to allow current measurements, as in the case of a quartz tuning fork, to be made.

In order to access the vacuum space the cables are attached to a room-temperature hermetic SMA feedthrough⁶.

	Temp. (K)	Sample A		Sample B	
		Drive	Return	Drive	Return
4K Plate	4.2	20 dB	-	20 dB	3 dB
1K Pot	1.2	-	-	-	-
Still	0.7	-	-	-	-
Cold Plate	0.4	10 dB	-	10 dB	-
Mixing Chamber	0.1	13 dB	-	13 dB	3 dB

Table 5.1: Attenuation used on high frequency rf lines between the 4 K plate and the mixing chamber of the dilution unit.

⁴Mini-Circuits Precision fixed attenuators, BW-S series

⁵Suggested in email communication between Dr. Chris Mellor (University of Nottingham), Dr. Phil Meeson (Royal Holloway University) and Dr. Grégoire Ithier (Royal Holloway University)

⁶RADIALL R143753000; Farnell part no. 4195632

Low Frequency Wiring

The original low frequency wiring on the fridge was replaced to ensure adequate heat sinking at the various stages. Wiring looms⁷ composed of 12 twisted pairs of 42 SWG constantan wire woven together with nomex to form a ribbon were used. This was joined to the original wiring at the 1 K plate, and thermally grounded by winding the loom around 12 mm diameter copper posts bolted to the fridge, at the intermediate stages. The looms were secured to the copper posts with GE varnish and dental floss.

For the heaters (still and mixing chamber) the constantan was replaced with 47 gauge copper wire to minimize heating along the length of the loom. Two additional constantan wiring looms were installed for additional thermometry and sample wiring.

Stage Control Wiring

Due to the capacitance of the piezoceramic elements within the nanopositioning stages it is important to ensure the wiring to the stages has a resistance of less than 10 Ω [65]. This ensures the time constant of the stages is kept sufficiently low to prevent attenuation of the ac control voltages. To meet this requirement 34 AWG teflon coated copper wire⁸ was chosen for the stage control wiring. Teflon coated wires were required as voltages of between 20 and 70 V are applied to the stages.

The wires were thermally grounded by wrapping the wire around copper posts mounted at the 1 K, still and cold plates. Due to the large voltages carried in the wires (20-70 V at 200-500 Hz) the wires were enclosed in grounded cupronickel tubing to shield the other wiring from these large ac signals.

5.2.2 Material Selection

In order to minimize any misalignment of the optics at low temperatures the optics and sample mounting space was fabricated from grade-II titanium, the same material

⁷CMR Direct CMR/CWL-12CO

⁸Phoenix Wire, Inc.

used in the construction of the nanopositioning stages [65], avoiding differential thermal contraction between the stages and their mounts.

In order to cope with the low temperature, UHV nature of the sample environment the LT/HV version of the nanopositioning stages were used. These stages are specifically designed to operate at low temperatures and under HV conditions.

5.3 Room Temperature Optical Arrangement

The room temperature optics are composed of a light source, fibre coupler, directional coupler and the photodetectors. To avoid damage and misalignment of the room temperature optics they are mounted on a rack directly above the dilution refrigerator. This minimises the length of exposed fibre running to the dilution refrigerator and reduces the chance of damage during cryostat operation. In order to protect the fibre optic running from the rack to the cryostat it is enclosed within a length of rigid compressor tubing.

5.3.1 Optical Source

The interferometer is designed to be operated with two optical sources, both with wavelengths of 633 nm, a HeNe laser⁹ and a semiconductor diode laser¹⁰.

The light source used for the measurement depends on the length of cavity that needs to be formed. Light from a HeNe laser, with a typical coherence length of ~ 30 cm [66], is able to form a cavity between the end of the fibre and the sample itself, while a diode laser has a shorter coherence length (typically a cm), in this case the cavity forms within the sample, or between a microscope cover slip inserted after the focussing lens and the sample, as discussed in section 5.4.3.

⁹Thorlabs 2 mW HeNe laser

¹⁰Hitachi 3 mW laser diode, HL6314MG

5.3.2 Fibre Coupler

Light is coupled into arm I1 using a commercially available fibre coupling system¹¹. The coupling system is composed of an FC fibre mount, an aspheric lens, and a 6-axis adjustment system. The lens is positioned so collimated light entering the system is brought to a focus. By adjusting the x, y and tilt the fibre can be positioned to lie at the focal point of the system.

The end of fibre I1 was connectorized with an FC connector to be compatible with the coupling system. Once connectorized the fibre was polished to maximize the amount of light coupled into the system.

5.3.3 Fibre Directional Coupler

The single mode fibre coupler around which this interferometer is based is, as previously mentioned, analogous to a beam splitter in a free space arrangement. It is made up of two lengths of single mode fibre, of core diameter $\sim 5 \mu\text{m}$ and numerical aperture 0.12. These fibres are twisted together and heated such that the fibres begin to fuse. This allows the evanescent field of light in one fibre to couple into the core of the other. The degree to which the fibres fuse influences the coupling strength. A 3 dB coupler is used in this work, which splits the optical power equally across the outputs [67].

5.3.4 Photomultiplier Tube

The light leaving fibre I2 is incident on a 1P28A photomultiplier tube from Hamamatsu Photonics¹². Photomultiplier tubes are incredibly sensitive light detectors and are commonly used for single photon counting because of their large gains and low shot limited noise. They are ideally suited for interferometry thanks to their frequency response and the ease with which light exiting a fibre can be collected by the large active area of the photocathode. The 1P28A has a rise time of 2.2 ns, which corresponds to a maximum detection frequency of around 400 MHz, well in excess of our detection electronics.

¹¹Thorlabs FibrePort Coupler PAF-X-5-B

¹²Hamamatsu Photonics, 1P28A

Light incident on the photomultiplier tube strikes the photocathode, which for SbCs at a wavelength of 633 nm has a cathode radiant sensitivity of ~ 2 mA/W [68]. SbCs has a lower resistivity compared to other photocathode materials, so a larger current is able to flow through the photocathode making it suited to applications where a high light intensity is to be measured [68, 69].

Amplification of the photoelectrons occurs at 9 intermediate dynode stages between the cathode and anode. The 1P28A is driven by a voltage (V_{PMT}) of up to 1250 V, which is equally divided between the 10 stages. As the electrons pass between stages a cascade effect multiplies the number of electrons. This is what gives photomultiplier tubes gains on the order of 10^3 - 10^8 depending on the voltage applied.

Photomultiplier Tube IV Converter

The current generated by the photomultiplier tube needs to be converted to a voltage for measurement. The transimpedance amplifier shown in figure 5.3 was constructed for this purpose. It was designed by Dr. C. J. Mellor and constructed by Bob Chettle.

A low-noise FET-input operational amplifier¹³ was used for the current to voltage conversion. This amplifier is commonly used in current conversion, where a relatively large source impedance is present. A feedback resistor of 10 k Ω used with this amplifier results in a transimpedance gain of $G \approx -10 \times 10^3$ V/A.

After conversion to a voltage the signal undergoes further amplification. The dc component ($f < 1.6$ kHz) is passed through an operational amplifier¹⁴, with a further gain of 10. This gave a low-impedance output that is recorded using the analog input of a data-acquisition card.

The ac signal is passed through an OPA847 operational amplifier with a gain of 40. After the ac amplification stage, there are a set of selectable low-pass filters (< 0.7 , < 10.7 and < 27 MHz) between a pair of buffer amplifiers that ensure a 50 Ω output

¹³Texas Instruments OPA657

¹⁴Linear Technology LT1128

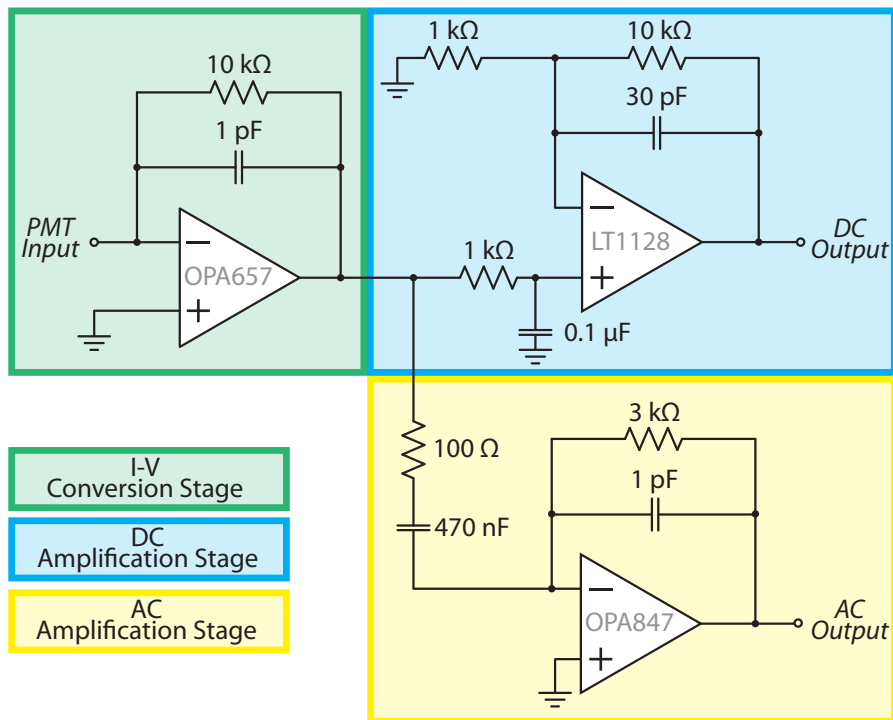


Figure 5.3: Current to voltage convertor for photomultiplier tube. This amplifier has three stages (indicated by the background colour). The current to voltage conversion (green) is carried out with a gain of $\sim -10^4$ V/A. This is followed by two amplification stages, a dc voltage amplifier (blue), with a gain of 10, and an ac amplification stage (yellow), with a gain of 30.

impedance. This output is monitored using either a network analyser¹⁵ or an RF lock-in amplifier¹⁶.

5.3.5 Photodiode

The optical irradiance at the sample can be monitored at output O2 using a photodiode¹⁷. This photodiode also optically isolates the fibre from ambient light in the lab. The index matching gel at the optical inputs help to minimize reflections at the fibre end that can interfere with light in the fibre and introduce noise to the measurements. This was seen by Breen *et al.* [70] who found that the index matching gel reduces the amount of light reflected back from the fibre termination at O2.

5.4 Low Temperature Optical Assembly

Light emerging from arm O1 of the coupler is collimated and focussed down onto the sample. This is achieved using two aspheric lenses mounted in a grade 2 titanium frame similar in design to the microscope described in [52]. The entire low temperature assembly is shown in figure 5.4.

The key requirement in the design of this section is the ability to adjust the separation between the fibre and the collimating lens while minimising stress on the single mode fibre. This was achieved by having a modular design for the optical assembly, where the fibre screwed into the collimating lens holder which could then be rotated to adjust the separation without twisting the fibre before coupling with the focussing lens mount. In the following sections the components that make up the low temperature assembly are presented.

¹⁵Agilent 8172ET

¹⁶Stanford Research Systems SR844

¹⁷ThorLabs AC110-AC

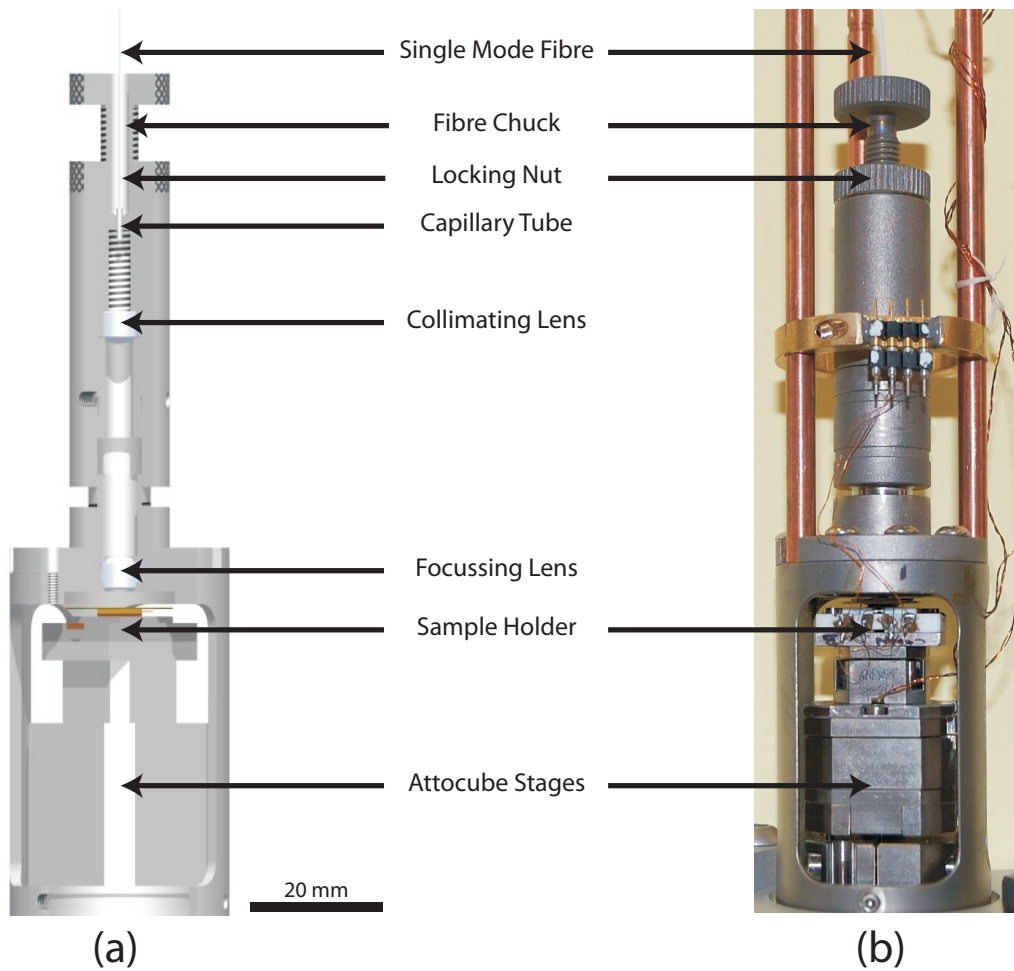


Figure 5.4: (a) Cutout of the low temperature optical assembly with the key components labeled. (b) Shows a photograph of the complete assembly with visible components labeled. Also visible in (b) are the copper posts used to thermally link to the mixing chamber, and the electrical connection block used to attach the rf lines to the sample holder.

5.4.1 Fibre Chuck

The fibre chuck consists of a threaded titanium piece with a hole running through the centre into which the fibre is secured. The core of the single mode fibre and cladding is $\sim 125 \mu\text{m}$ in diameter, so to protect the fibre and simplify mounting into the interferometer the end of the fibre is cleaved at right angles and mounted in a 1 mm outer diameter glass capillary tube [71] secured using fibre optic epoxy¹⁸, with 0.5 to 1 mm of fibre protruding from the chuck. The threaded mount allows adjustment of the separation between the fibre tip and the collimating lens. Once set the separation is fixed using a knurled locking nut.

Fibre optic epoxy was chosen to secure the fibre in the chuck as it has a low thermal decomposition temperature. If the fibre needs replacing the epoxy is removed using a blowtorch and the fibre chuck reused.

5.4.2 Collimating Lens Mount

As mentioned earlier, the single mode fibre used in the coupler has a numerical aperture (NA) of 0.12. The numerical aperture is related to the half angle of the cone, θ , by $NA = n \sin \theta$. This means that the light exiting the fibre is divergent, with a half angle of $\sim 7^\circ$. In order to collimate as much of the emerging light as possible the aspheric lens must have a numerical aperture equal to or greater than that of the fibre¹⁹. A short effective focal length minimizes the overall length of the optical assembly.

The lens is placed in a threaded tube and held in place with a retaining nut. The other end of the tube is threaded to receive the fibre chuck. Rotating the lens tube allows the the bare fibre to be brought to the focal point of the lens and a collimated beam of light produced. Once a collimated beam is achieved a locking nut secures the fibre chuck in position, fixing the fibre lens separation.

¹⁸Capillary tube removed from Thorlabs reusable Fibre-to-Fibre splice, TS125, held in place using Thorlab Fibre Epoxy F120

¹⁹LightPath Technologies 325280B, NA = 0.15; EFL = 18.4 mm

5.4.3 Focussing Lens Mount

A second aspheric lens²⁰ focuses the now collimated light onto the sample. A larger numerical aperture lens has an increased ability to capture light reflected from the sample, so a lens with a numerical aperture of 0.54 and an effective focal length of 5.50 mm was chosen. This lens sits within a mount into which the collimating lens tube and fibre chuck assembly mounts. To avoid twisting, and potentially breaking the optical fibre the collimating assembly slides into the focussing lens mount where it is held in place by three grub screws. The sample is moved to the focus by the z-positioning stage.

Cover Slip

In order to modify the cavity length it is possible to insert a microscope cover slip between the focussing lens and the sample. This introduces a reflective surface into the cavity nearer to the sample which allows light of a shorter coherence length to be used. The two cavity configurations (in addition to the cavity that can form within the NEMS itself) are shown in figure 5.5. The aspheric lenses making up the interferometer have anti-reflective coatings and as such should not introduce reflections into the interferometer.

In the absence of the microscope slide the cavity shown in figure 5.5(a) is formed between the sample and the bare fibre, for which the cavity length is ~ 65 mm. For the two-beam case of a low-finesse cavity this arrangement will require a light source with a coherence length of at least 130 mm (twice the cavity length) to ensure light reflected from the sample is coherent with the light reflected from the fibre, in this case the HeNe laser is used.

The microscope cover slip is made of BK7 glass and will introduce a 4 % reflection at the top and bottom of the coverslip. In order to minimize one of these reflections an anti-reflective coating was applied to the surface of the cover slip nearest the lens as indicated in figure 5.5(b). The anti-reflection coating is composed of silicon nitride and silicon dioxide deposited using plasma enhanced chemical vapour deposition (PECVD)

²⁰LightPath Technologies 325105B, NA = 0.54; EFL = 5.50 mm

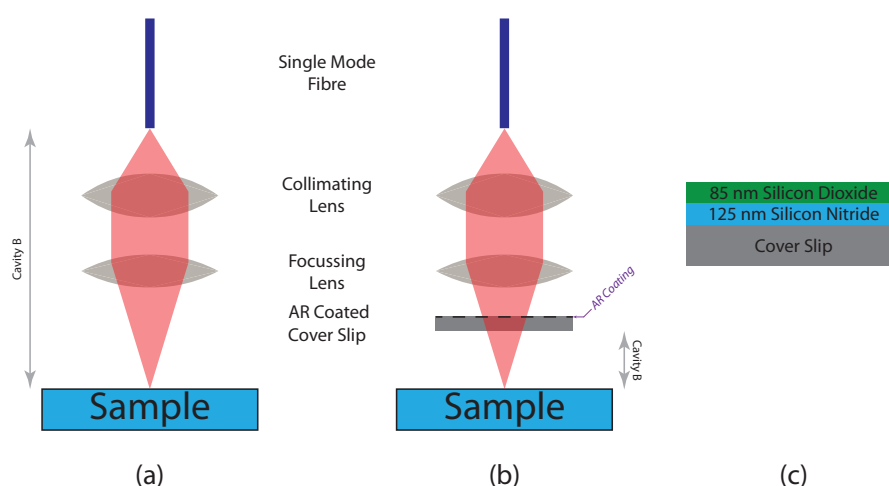


Figure 5.5: Without a microscope cover slip the cavity shown in (a) is formed within the interferometer, with a microscope coverslip inserted between the focussing lens and the sample cavity (b) is formed. (c) Shows the make-up of the anti-reflective coating applied to the cover slip to minimize reflections from the top-surface of the microscope slide.

carried out by Dr. C. J. Mellor. The composition of the anti-reflection coating is shown in figure 5.5(c), with layer thicknesses that were determined using the multi-layer film theory outlined in section 3.1.2.

With the microscope cover slip in place the cavity length reduces to the separation between the top of the sample and the bottom of the cover slip, a distance of ~ 4 mm which allows a light source with a far shorter coherence length, such as a diode laser, to be used.

For light of $\lambda = 633$ nm a change of ΔL in the cavity length, L , will alter the responsivity of the interferometer as $\mathfrak{R} \propto \cos(4\pi\Delta z/\lambda)$. For $\Delta L = 15$ nm this equates to a ~ 5 % decrease in responsivity, while 30 nm will decrease the responsivity by ~ 18 %. This change in length will have the same effect on the responsivity regardless of the overall cavity lengths, however assuming the extension and contraction of the cavity per unit length is uniform the shorter cavity should be more stable. This was seen in a set of stability measurements made by Attocube on a titanium reference cavity at

4.2 K using a Fabry-Perot interferometer [72]. The standard deviation was calculated for measurements made over a 10 hour period for three cavity lengths. As the cavity length increased so too did the standard deviation from 345 pm for a 20 mm cavity to 1035 pm for a 110 mm cavity. It is important to note that the reference cavities measured by Attocube were made from a single piece of titanium, while the cavity discussed in this work is made from several pieces of titanium and contains a set of positioning stages that are designed to be adjustable so a larger deviation in cavity length is expected. In an ideal situation the cavity length is reduced as much as possible, as in the case of the silicon nitride devices where the cavity can be formed within the sample itself ($L < 1 \mu\text{m}$).

At longer coherence lengths interferences within the fibre can become more pronounced. These arise where defects in both the core and the cladding reflect light, especially where the fibre curves. Acoustic vibrations modulate the distance between these defects and introduces noise to the detected signal. If these defects are assumed to be uniformly distributed throughout the fibre then as the coherence length of the light decreases, so too does the number of reflections from defects that are coherent to one another.

5.4.4 Nano Positioning Stage Assembly

Correctly positioning the sample below the focussing lens within the interferometer is achieved using 3 commercially available linear positioning stages supplied by Attocube Systems²¹. These stages are constructed from grade-2 titanium and are designed to provide positioning with nm precision in low temperature, UHV environments.

The positioners operate using the slip-stick principle and are composed of three parts. A base that is firmly anchored, a piezoceramic element, and a carriage connected to the piezoceramic by a set of leaf springs. The stages are controlled by applying a sawtooth voltage to the piezoceramic. As the voltage (and consequently the length) is rapidly increased the friction between the piezoceramic and the leaf springs is overcome and

²¹ANPx51/LT/HV, ANPx101/LT/HV and ANPz101/LT/HV

the stage will “slip”. The voltage is then slowly decreased, the carriage “sticks” and is drawn along with the piezoceramic.

Typically at room temperature voltages of 20-30 V are applied at a frequency of 200 Hz. As the temperature decreases, so too does the extension of the piezoceramic with applied voltage, requiring the application of higher voltages (and frequencies). Voltages, frequencies and step sizes measured at several temperatures are given in table 5.2.

Temperature (K)	Voltage (V)	Frequency (Hz)	Step Size (nm)
300	25	200	100
77	40	200	70
4.2	60	500	30

Table 5.2: Typical frequencies and voltages applied to the linear positioning stages along with step sizes for a range of temperatures

The positioning stages are mounted at the base of the dilution fridge within a cage of grade-2 titanium, the design of which is shown in the lower part of figure 5.4. The cage in which the motors are mounted serves two purposes. The first is to ensure that the alignment of the optics and sample do not change as the system is cooled, consequently grade 2 titanium was chosen, the same material as the nanopositioning stages are made of. This reduces the chances of misalignment due to differences in thermal contraction between the different sections.

The second role is to provide a firm base to anchor the positioners and allow the slip-stick motors to operate efficiently. This is achieved by mounting the stages on a titanium base plate that has a tight fit into the base of the mount, secured in place by three grub screws. To ensure sufficient thermal contact the experimental region is connected to the mixing chamber by three copper struts, tapped to screw directly into the mount and the mixing chamber. These struts are split approximately half way up and rejoined using a copper collar with a tight fit, held in place by grub screws.

5.4.5 Sample Holder

The sample holder shown in figure 5.6 was designed and constructed to allow the sample to be attached to the nanopositioning stages and inertially actuated. The base of the sample holder is made from MACOR into which a copper block and four 20 SWG wires are affixed using a non-conductive epoxy²². These copper wires act as anchoring points for drive wires to avoid stressing the piezoceramic.

The piezoelectric element is a 6 mm \times 6 mm sheet of EBL#2 piezoceramic²³. In order to obtain the frequencies required to actuate the nanomechanical devices a sheet of thickness 0.165 mm was chosen. When operated in the thickness mode this sheet has a resonant frequency of 12.0 MHz. Gold is coated on both sides of the piezoceramic to assist with electrical contacting.

The piezoceramic is affixed to the central copper block using electrically conductive silver epoxy²⁴. Once the epoxy is applied the sample holder is held in a PTFE jig and baked in a convection oven at 100°C for 2 hours. The electrical contact to the top of the sheet of piezoceramic comprises a 12 \times 12 mm sheet of 0.25 mm thick titanium, again attached using silver epoxy. The sample is affixed to the titanium top plate using a spot of superglue in one corner, this minimizes any additional stress that is applied to the sample while allowing the sample to be easily removed and the sample holder recycled.

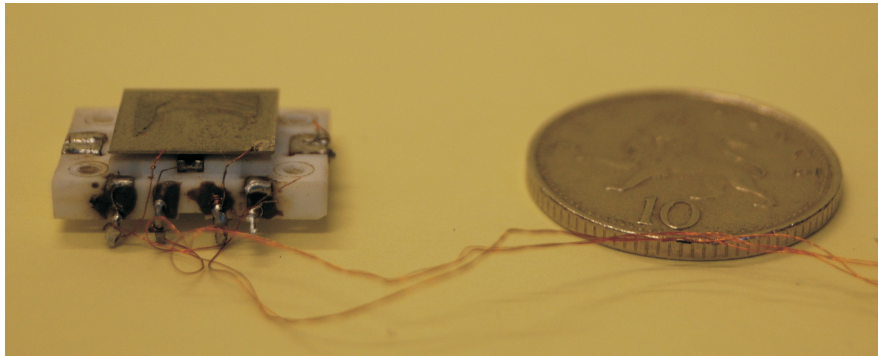
A drive voltage is applied to the central copper block, while the titanium top plate is held at ground as shown in figure 5.6(c). Both electrical connections were made using 47 swg copper wire, soldered to the thicker copper wires attached to the MACOR base as shown in figure 5.6(b).

The MACOR base acts to electrically isolate the piezoceramic sheets from the At-tocube stages. A titanium block was machined to enable the sample holder to be secured to the positioning stages.

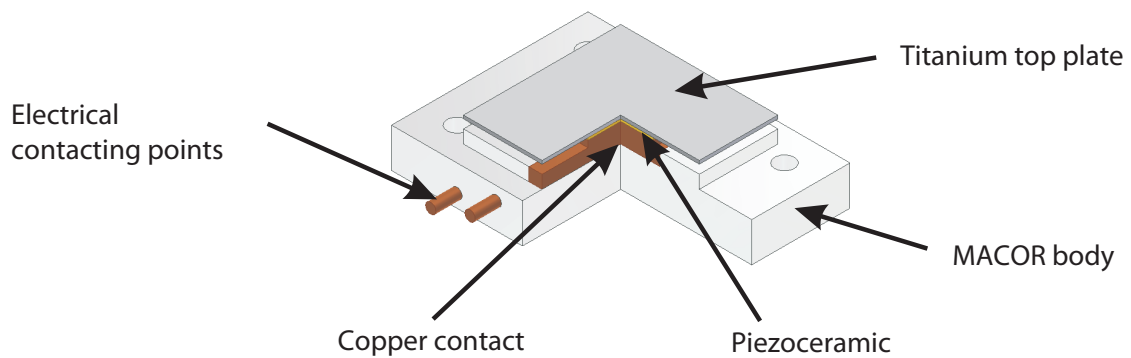
²²JB Weld

²³EBL Products inc.

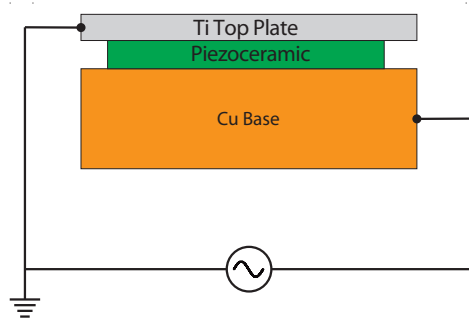
²⁴Epotek H20E-PFC



(a)



(b)



(c)

Figure 5.6: (a) Photo showing the sample holder used as part of this work. (b) Cutout showing the makeup of the sample holder. (c) Cross section of the sample holder showing the electrical connections to the piezoceramic.

5.5 Measurement Techniques

So far in this chapter we have introduced the components that make up the experimental setup. We will now turn our attention to the control electronics and measurement techniques employed in this work. These can be divided into two measurement types: confocal imaging, where the sample is imaged by scanning the positioning stages and rf measurements where the frequency response of a mechanical device is measured.

This section outlines how the measurements are taken and the data are analysed. As part of this measurements made using the interferometer on nanomechanical devices (made from high-stress silicon nitride) and on quartz tuning forks will be presented. Measurements are made using control software written in LABVIEW, while the data analysis is carried out in MATLAB.

5.5.1 Confocal Imaging

In order to accurately position the device an image must be built up of the surface of the sample beneath the optical spot. This is done by operating the interferometer as a confocal microscope.

In confocal microscopy light from a laser source is spatially filtered by passing the light through an aperture such as a pinhole or, as in this case, the core of a single mode fibre. This produces a beam with a Gaussian profile which is then collimated and focussed onto the sample by an objective lens. The beam is reflected and scattered by the surface before being recaptured by the objective lens. Spatial filtering occurs once more with only light in focus passing back into the core of the fibre while the out of focus light is rejected [19].

If the stage is scanned while recording the intensity of light at I2 it is possible to build up an image of the sample surface pixel by pixel. In the following sections an overview of how surface scans are acquired using the interferometer are presented.

Stage Control

As mentioned previously an image is constructed by moving the sample relative to the fibre and recording the reflected optical power as a function of position. The acquisition of each pixel is made up of three parts, each with an associated time: moving the stage (T_{step}), allowing the stage to stabilise at the new position (T_{stab}) and taking a measurement (T_{meas}). Hence the total time taken to acquire a datapoint is $T = T_{step} + T_{stab} + T_{meas}$.

The step time is defined by how quickly the control electronics can make a step and the time taken for the stage to move. Control voltages are applied at frequencies of at least 200 Hz, which means the time taken for a single step is at most 5 ms. The unit that drives the positioning stages²⁵ has two inputs that can be used for computer control, an RS232 connection and a TTL input. The RS232 connection is used to send ASCII commands to configure and control the stages, while the TTL inputs can only be used to step the stages [73].

A serial port is used to send ASCII commands, for which the manufacturer specifies a minimum time per command of 50 ms, the TTL input on the other hand can step the positioner by being held high for just 10 ms. It was decided to use the RS232 interface to configure the stages, while the actual stepping of the positioner would be accomplished using the TTL input as during earlier tests the TTL input was seen to not only be quicker, but also more reliable as the RS232 connection would on occasion not register commands when they were sent in rapid succession.

TTL pulses were generated by a DAQ card²⁶, in order to control the motion of travel 6 digital lines were required, two (corresponding to the up and down directions) for each of the three axes. A digital output was also used to trigger the data acquisition on an analog input of the DAQ card.

The other two times (stabilisation and measurement) are defined by the user. In tests it was found that a time of 20 ms for both the settling and data acquisition gave

²⁵Attocube ANC150 control unit

²⁶National Instruments PCI6052E

good results. A spike during T_{step} due to the sharp motion of the stage was observed, so a value of $T_{stab} = 20$ ms was chosen to allow the sample to settle and the signal to stabilise. In order to remove any noise arising from the mains supply measurements were made over $T_{meas} = 20$ ms (corresponding to one cycle of the 50 Hz mains frequency) and a mean taken. Images acquired generally consisted of 10,000 pixels (a 100×100 pixel field), for which the acquisition time is approximately 8 minutes.

Scan Patterns

Slip-stick motors are normally used for coarse positioning only. This is due to issues in reproducibility that arise from the way in which they operate. For the stages used in this work, the manufacturer gives a typical step asymmetry of 5 % for the xy- and 5 – 10 % for the z-positioner[65]. Previous work [74] has shown the step asymmetry does not pose as large a problem as first thought, with the fast scan axis “locking” into a stable region after a few rows and giving reproducible consecutive scans.

In order to determine the sample position and locate the optical spot on a device of interest, images were acquired by rastering the surface of the sample beneath the optical spot. The axes can be thought of in terms of a fast and a slow axis. On the fast axis one (or more) rows of datapoints are recorded before the slow axis is moved, allowing a new region of the sample to be imaged and a picture of the sample built up row by row. The two scan patterns shown in figure 5.7 were used in this work. The quicker of the two, figure 5.7(a), scans the fast axis in one direction before a step is taken on the slow axis and the fast axis scanned in the opposite direction.

In the slower scan pattern, figure 5.7(b), the fast axis is scanned up and down between each slow axis step. This scan pattern therefore produces twice the datapoints (and consequently take twice as long) as the faster scan, but appears to give the most reproducible results and minimizes the effects of step asymmetry on the scan pattern. This performance is attributed to the locking of the stages mentioned earlier.

Any asymmetry in the step sizes in the up and down directions of the fast axis will

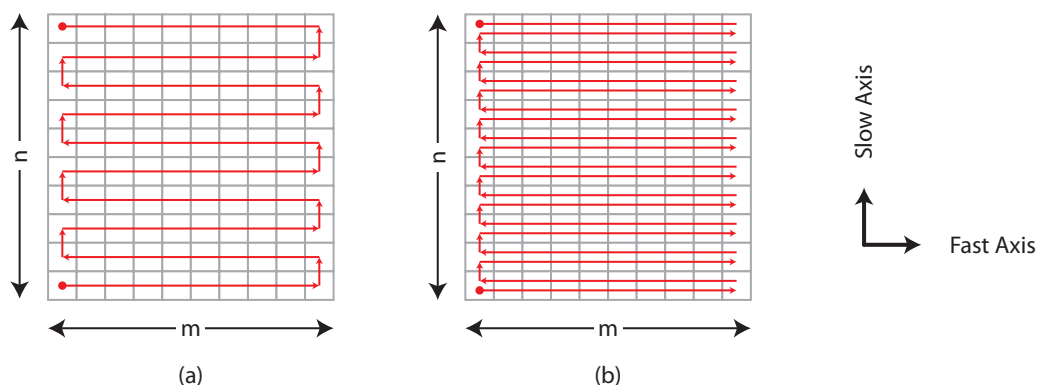


Figure 5.7: Scan patterns used when acquiring confocal images. (a) Shows the quicker of the two scan patterns, where between each fast axis scan the slow axis is stepped. (b) Shows a slower scan pattern, where a scan up and down the fast axis is carried out before stepping up in the slow axis.

tilt the features as the up and down rows shift out of alignment on successive scans. If the stages lock into a specific range of motion this asymmetry will no longer cause a problem and successive fast axis scans will align. The downside to this is that, if the range of motion to which the stages lock is too small, then for part of the fast scan, the stages will be stationary. An extreme example of this is shown in figure 5.8 which was obtained using the faster of the two scan patterns.

Figure 5.8(a) shows all of the pixels obtained during the scan, and at first glance appears to show two sets of location markers. If we separate the fast scan axis data into points recorded in the down (figure 5.8(b)) and up (figure 5.8(c)) directions the extent to which the stages have locked becomes clear. For almost half the fast axis scan the stages are not in motion, and when they are in motion it appears that the steps in the up direction are larger than those in the down direction. If the stages were not operating over a fixed range then the rows would not line up and the scan would be distorted.

Meyer *et al.* [74] attribute this locking to self organisation of the surface between

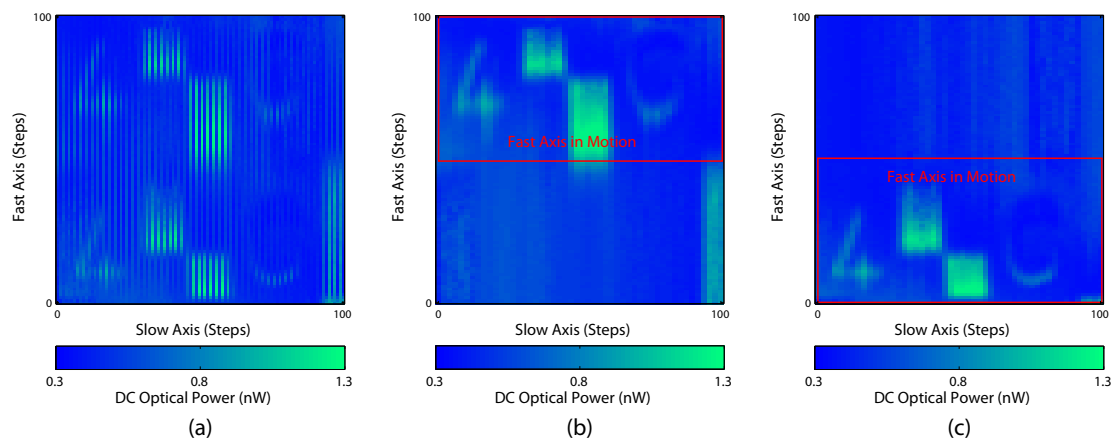


Figure 5.8: Confocal image of a gold pattern on silicon nitride imaged at 4.2 K using the fast scan pattern. (a) Shows the full scan, while the down and up scans in the fast axis have been isolated and are shown in (b) and (c) respectively.

the piezoceramic element and the mount. This “locking” while useful when imaging a small region of the sample did cause issues if the region to which locking occurred was not of interest. In these cases it was sometimes necessary to scan the offending stage over a large range of motion several times to break the locking effect.

Confocal Imaging of Silicon Nitride Nanomechanical Devices

In this section, a range of confocal measurements made on silicon nitride samples are presented. We examine how the coherence length of the light can affect the image obtained, and the quality of images that can be generated when the stages are behaving as expected. We will then move on to examine how images of the frequency response of a nanomechanical resonator are obtained.

In order to improve the resolution, the coherence length of the laser diode was reduced by decreasing the supply current to just below the lasing threshold, this results in a lower detected optical power and drastically reduces the intensity of interference fringes seen. The lower optical power is compensated for by increasing the gain of the photomultiplier.

Two examples of this are shown in figure 5.9.

For metalised features, such as those shown in figure 5.9(a) and (b) a cavity is formed between the sample, and the microscope slide at the top of the sample mounting can. In the case of light where the coherence length is greater than twice the separation between the sample and the reflective surfaces interference fringes are seen that correspond to any tilt there may be on the sample. This tilt introduces a gradual change in the cavity length as seen in figure 5.9(a), where fringes of varying intensity can be seen. In the case of light with a shorter coherence length, figure 5.9(b), the light reflecting from the surface at the top of the cavity and the sample is no longer coherent and does not interfere and as such these fringes are no longer present.

In the case of a nanomechanical device, such as the cantilevers shown in figures 5.9(c) and (d), two cavities exist within the experimental setup; one where reflections from the sample and the coverslip at the top of the sample space interfere and a second cavity within the layers of the sample itself. If the coherence length of the light is reduced, the interference fringes visible in figure 5.9(c) are no longer present, as shown in figure 5.9(d).

In figure 5.9(d) we also see the effect that nitride thickness has on the reflectivity of the sample. A variation in the intensity of the reflected light can be seen along the length of the cantilever, with a maximum lying near to the tip of the beam that corresponds to the point at which the thickness of the vacuum gap, and the nitride combine to give a maximum in reflectivity. This variation in nitride thickness arises from the fabrication process, and the variation in accessibility of the hydrofluoric acid to the sacrificial oxide layer beneath the mechanical element.

A large area scan, 500×500 pixels in size was taken, and is shown in figure 5.10(a) alongside SEM and optical images of the same region of device, showing very good correlation between the confocal images taken using the system described in this thesis, and images taken using commercially available systems during fabrication.

The optical spot probing the sample has a finite size that will introduce a blurring to

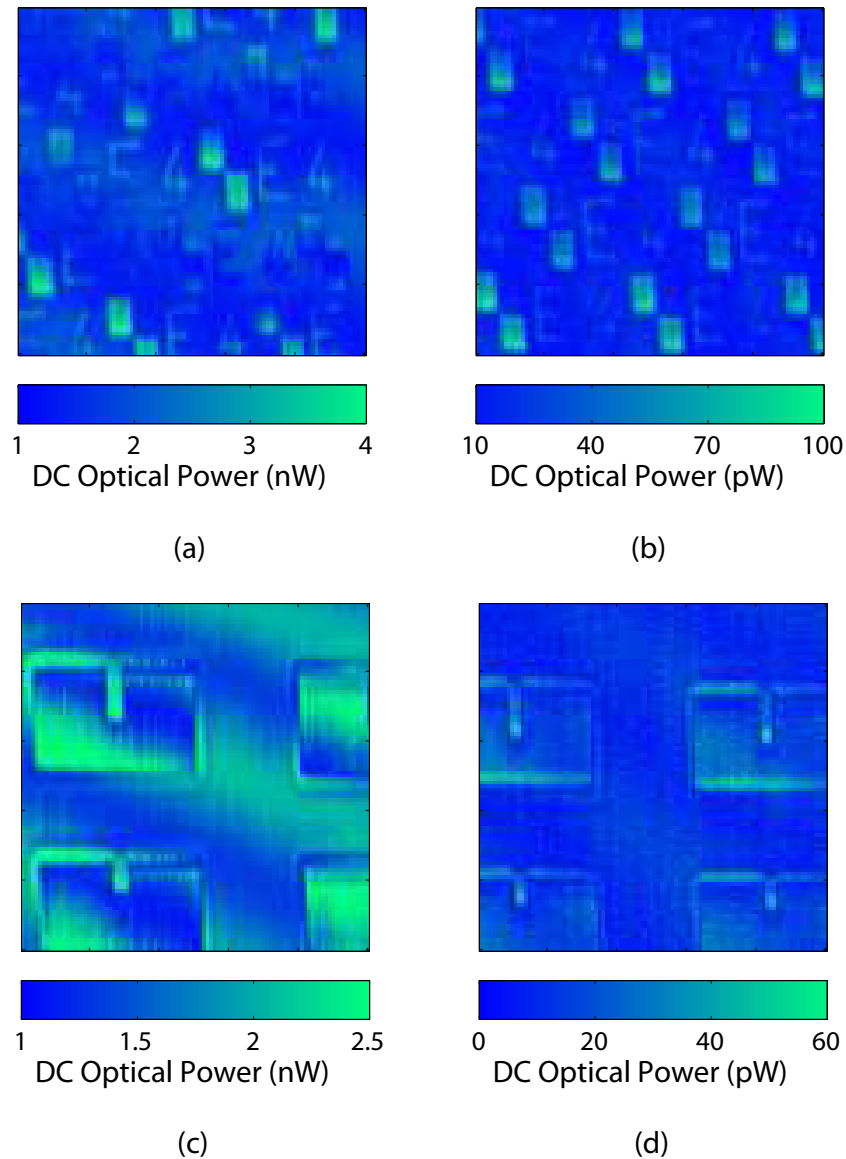


Figure 5.9: Confocal images of two samples. Images were taken of a gold patterned substrate ((a) and (b)) and stress relieved silicon nitride cantilevers ((c) and (d)). A diode laser was used as the optical source, operated above the lasing threshold, resulting in a longer coherence length ((a) and (c)) and below the lasing threshold, resulting in a shorter coherence length ((b) and (d)).

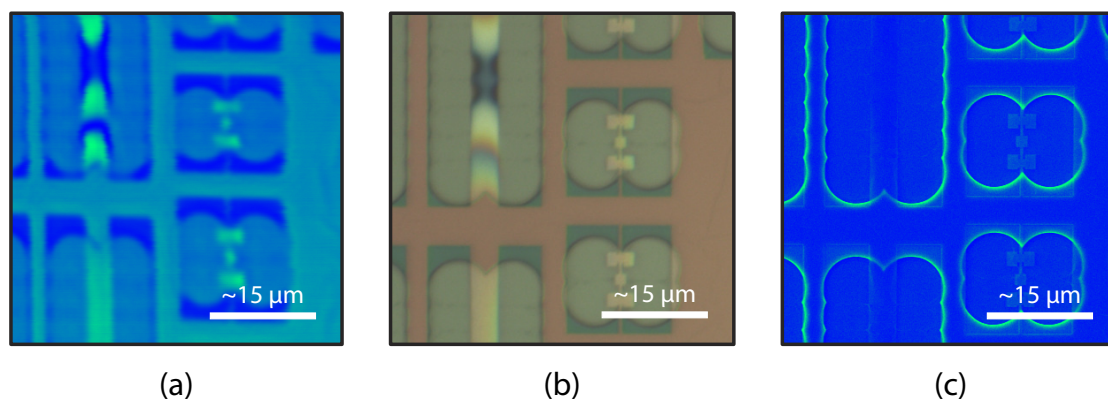


Figure 5.10: (a) Confocal scan at ~ 4.2 K, short coherence; (b) Optical microscope image ($100\times$ magnification); (c) SEM image.

the recorded image. The profile of the optical spot is described by a Gaussian function of width σ [75]:

$$G(x) = \frac{1}{\sqrt{2\pi\sigma^2}} e^{-x^2/2\sigma^2} \quad (5.1)$$

The blurring due to the optical spot is equivalent to convolving a Gaussian with the expected response [37]. To determine the resolution of the system the expected response was convolved with several Gaussian functions of varying width and compared with experimental data. A comparison of this kind is shown in figure 5.11 where a subset of the confocal data presented in figure 5.10(c) was compared with the expected response for several Gaussian functions of varying widths.

The subset analysed is indicated by the box in the inset of figure 5.11 and a mean of the rows (indicated by the direction of the arrow) calculated. The idealised response of the sample was made up of three top hat functions representing the three paddles. The central paddle was not present in all of the lines and to account for this the amplitude of the central top hat function was reduced from 1.00 to 0.85²⁷. Once convolved the signals are normalised such that the maximum amplitudes were equal and compared with the

²⁷Central paddle detected in $\sim 85\%$ of the lines from which the mean was taken

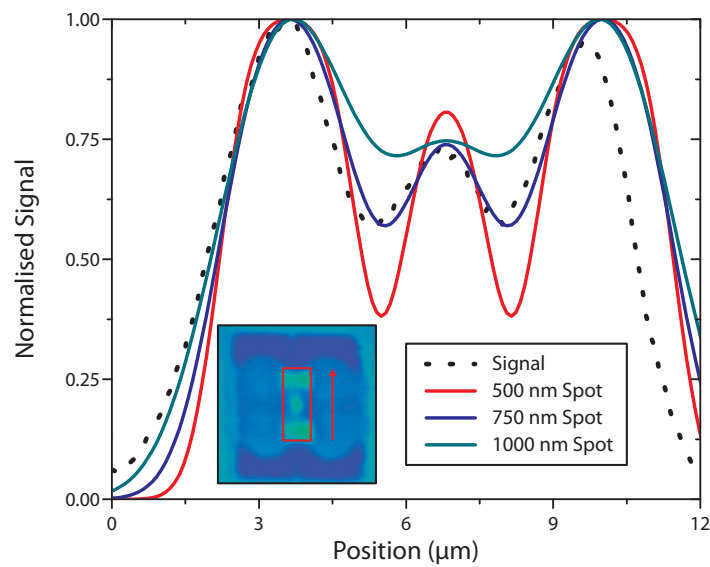


Figure 5.11: Comparison of experimental data with simulated data obtained by convolving a step function representing the three paddles of the torsional resonator with three gaussian functions of varying widths.

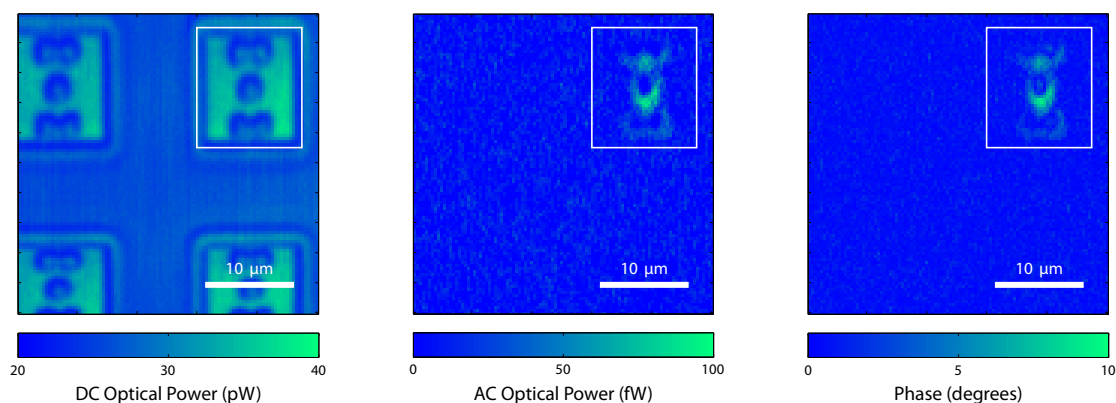


Figure 5.12: Confocal image of an array of torsional resonators imaged at 4.2 K. The image on the left shows the dc response, with the magnitude and phase of the ac response shown in the central and right images respectively. The sample was driven at 12.709 MHz with a power of -16 dBm inserted at the top of the fridge. The square is a guide to the eye, identifying the area of the sample in which the torsional resonator of interest lies.

experimental data the resolution of the system was determined to be $\sim 0.75 \mu\text{m}$.

In addition to the static response of a nanomechanical device the ac response of a device was also imaged. An example of this sort of a measurement made on a three paddle torsional resonator is shown in figure 5.12. Having located and determined the resonant frequency of the first flexural mode of the resonator, the stage was relocated and the resonator scanned. The piezoelectric holder was driven at 12.709 MHz with the ac output of the photomultiplier monitored using a lock-in amplifier. In addition to recording the dc signal, the magnitude response was also recorded using the monitor output of the lock-in amplifier connected to an analogue input of the DAC card.

Figure 5.12(a) shows the dc scan, in which an array of 4 torsional resonators is visible. During the ac scan, figure 5.12(b), only the torsional resonator that is in motion is visible and moving in phase, as seen in figure 5.12(c), which confirms that we are observing the lowest order flexural mode of the torsional resonator. A frequency sweep

of the torsional resonator measured it to have a quality factor of $\sim 1.05 \times 10^4$, this is presented in the following section where rf measurement techniques are discussed. The fact that only one device is seen to be in motion indicates that the resonant frequencies of the other resonators are sufficiently different, most likely due to variations in the fabrication process over the sample, that the resonances do not overlap significantly.

5.5.2 RF Measurement Techniques

Once amplified the ac signal was monitored in one of two ways. A network analyser²⁸ was used initially to determine the resonant frequency of the devices, as it allows a large range of frequencies to be swept in a short amount of time. Once a resonance was detected an rf lock-in amplifier²⁹ was used to demodulate the frequency response of the device into orthogonal in-phase (X) and quadrature (Y) components. This response could be recorded in two ways, by sweeping the frequency and recording the response of the device (frequency domain), or applying an rf pulse at the resonant frequency and recording the temporal decay (time domain).

Frequency Domain Analysis

The frequency domain method allows a direct measurement of the response of the resonator which when operating in the linear regime is described by the Lorentzian (introduced in section 2.1):

$$R(f) = \frac{\frac{Af_0^2}{Q}}{(f_0^2 - f^2) + i\frac{ff_0}{Q}} \quad (5.2)$$

In the following section the fitting procedure is illustrated using measurements made on a 28 μm long doubly clamped high-stress silicon nitride beam at 2 K.

The in-phase (X) and quadrature (Y) components are recorded and Matlab is used to perform a 6 parameter fit to $R = X + iY$ allowing the resonant frequency and quality factor to be extracted. The fit parameters are the magnitude of the response (A_0),

²⁸Agilent 8172ET

²⁹Stanford Research Systems SR844

the resonant frequency (f_0) and the quality factor (Q). The fit also takes into account the experimental setup via C_x and C_y which account for any dc offsets in the lock-in amplifier. The phase angle, ϕ , between the resonator response and the detection frequency is applied to $\Re(R)$ and $\Im(R)$ using the rotation matrix [75]:

$$\begin{bmatrix} X \\ Y \end{bmatrix} = \begin{bmatrix} \cos \phi & \sin \phi \\ -\sin \phi & \cos \phi \end{bmatrix} \begin{bmatrix} \Re(R) \\ \Im(R) \end{bmatrix} \quad (5.3)$$

Given the large number of fitting parameters good initial guesses are required. The first stage is to fit a Lorentzian to the absolute data

$$|R(f)| = \frac{\frac{Af_0^2}{Q}}{\sqrt{(f_0^2 - f^2)^2 + \left(\frac{ff_0}{Q}\right)^2}} + C_0 \quad (5.4)$$

which is a 4 parameter fit consisting of A_0 , f_0 , Q , that were introduced previously and C_0 that accounts for any dc offsets in the system. From this initial fit values used as starting points for the 6 parameter fit are obtained.

In order that the solver converge on a solution within a reasonable amount of time good initial guesses for the fit parameters are needed and the magnitude of the coefficients guessed by the solver should be similar. To ensure this the frequency data, measured in kHz, is shifted so that the centre frequency lies at 0 Hz. The data is normalised such that the maximum value of R (and consequently the initial guess for A_0) is equal to 1, with f_0 taken to be the frequency at which this maximum value occurs.

An estimate of Q is obtained by finding the FWHM, Δf , with $Q = f_0/\Delta f$. The quality factors are expected to be in excess of 10^4 , for a resonator with $f_0 = 1$ MHz this would correspond to a FWHM of 0.1 kHz. Working in kHz and centring the frequency range on 0 Hz ensures that when guessing the resonant frequency the changes made by the solver to f_0 are of a similar magnitude to those made to the other coefficients. The quality factor is also rescaled by dividing by 10^4 . An estimate for C_0 is obtained by taking the mean of the first and last 10 normalised datapoints away from resonance. A fit to the displacement magnitude data for a doubly clamped silicon nitride beam is

shown in figure 5.13.

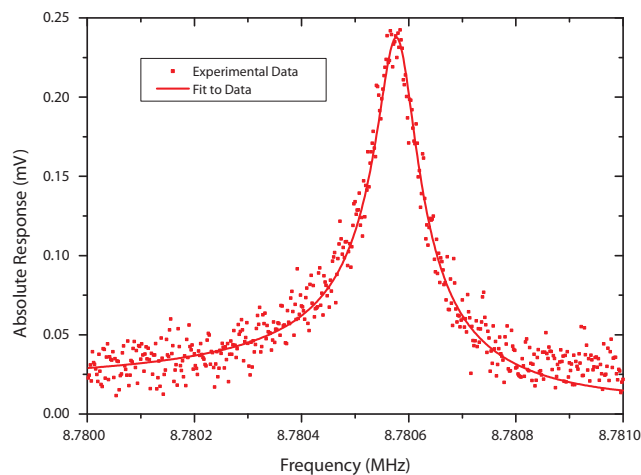


Figure 5.13: The magnitude of the displacement response of a 28 μm doubly clamped beam of silicon nitride measured in vacuum at a temperature of 2 K. The points show the experimental data, with the fit indicated by the solid line.

Once initial values have been calculated, a full 6 parameter fit can be carried out, using values from the previous fit as starting guesses. Additional coefficients required are a phase angle for the rotation matrix (assumed to be $\pi/4$) and values of C_x and C_y which are assumed to be unique to each channel of the lock-in amplifier and therefore not affected by the phase angle. These are again estimated by averaging the first and last 10 datapoints away from resonance, and are added after the rotation matrix has been applied. A full fit to the experimental data is shown in figure 5.14, for which a quality factor of $(1.135 \pm 0.003) \times 10^5$ was measured, with a resonant frequency of 8.78 ± 0.01 MHz. Errors were taken to be the standard deviations of the coefficients, obtained from the covariance matrix of the fit.

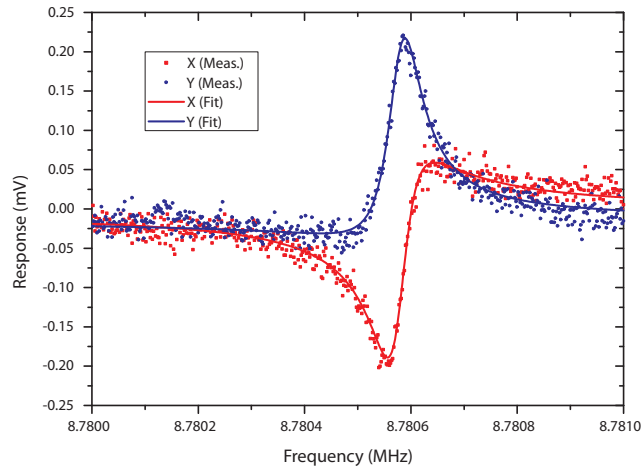


Figure 5.14: The X and Y response of a $28 \mu\text{m}$ doubly clamped beam of silicon nitride measured in vacuum at a temperature of 2 K. The points show the experimental data, with a non-linear fit indicated by the solid line.

Time Domain Analysis

For a time domain measurement (sometimes referred to as a ringdown measurement) a pulse of rf is applied to the resonator and the evolution of the response with time recorded. A lock-in amplifier is used to demodulate the resonator signal which is then recorded using a DAQ card.

Measurements are made using the arrangement shown in figure 5.15, where two signal generators³⁰ (synchronised by connecting their 10 MHz timebases) are used. One drives the sample with the other synchronising the lock-in generator to the excitation frequency. A digital pulse from the DAQ card is used to gate the rf output of the drive signal generator. Typically a 1 Hz square wave with a 20 % duty cycle is used to produce 200 ms long pulses of rf.

The rf signal drives the nanomechanical resonator at the resonant frequency, with the ac output of the photomultiplier tube connected to the lock-in amplifier, the time

³⁰Agilent E4420B (drive signal) and Agilent E4400B (detect signal).

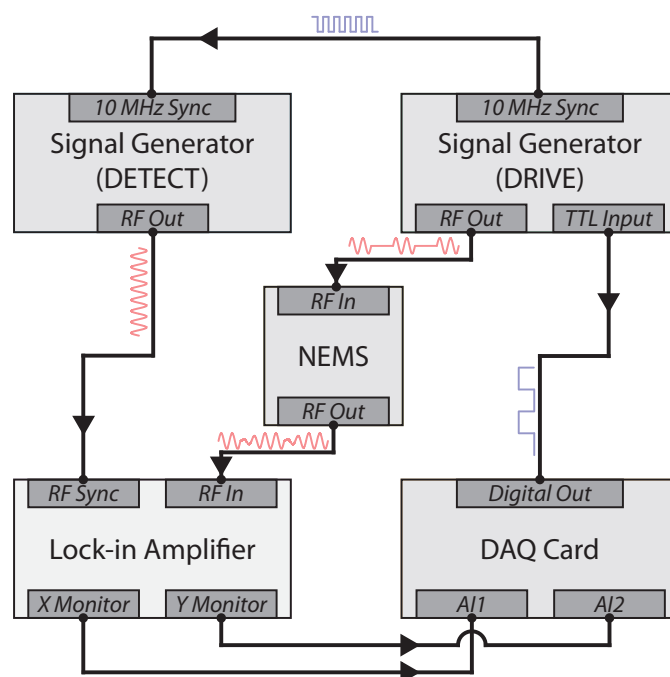


Figure 5.15: Diagram of the experimental setup used to make time domain measurements. Two signal generators are used to drive the sample and synchronise the lock-in amplifier. Pulses are generated using the digital output of a DAQ card to provide TTL pulses that gate the rf output of the drive signal generator. These pulses are used to drive the NEMS and the evolution of the resonator over time is recorded using the analog inputs of the DAQ card.

constant of which is set to $100 \mu\text{s}$. The monitor outputs for the X and Y channels of the lock-in amplifier are recorded using the analog inputs of the DAQ card.

Upon removing the rf drive from the resonator, the signal will decay exponentially. The rate at which this decay occurs is directly related to the damping of the resonator and is described by

$$\begin{aligned} X(t) &= A_x e^{-t/\tau} \sin(2\pi ft) \\ Y(t) &= A_y e^{-t/\tau} \cos(2\pi ft) \end{aligned} \quad (5.5)$$

In both channels the function is sinusoidal with an exponentially decaying envelope

function the form of which contains information regarding the damping of the resonator. The damping time can be extracted from the absolute response of the resonator, $R(t)$ which is

$$R(t) = \sqrt{X(t)^2 + Y(t)^2} = A_0 e^{-t/\tau} \quad (5.6)$$

Ringdown measurements are quicker than swept frequency measurements, but the fast time constant of the lock-in amplifier introduces noise to the measurement. In order to overcome this the measurement is repeated a number of times and an average taken. Unfortunately the pulses produced by the signal generator are not phase coherent (starting at different points in the excitation cycle) and as such averaging the X and Y values will result in the signal averaging to zero. Therefore R is calculated for each run and a mean of this value taken. If the signal were to be Fourier transformed, the frequency domain response of the resonator would be obtained, which could then be analysed in the way described in section 5.5.2 requiring a fit with 4 coefficients. A simpler approach is to analyse the response in the time domain by taking the natural log of equation 5.6 which can then be rewritten as

$$\ln(R(t)) = \ln(A_0) - \frac{t}{\tau} \quad (5.7)$$

for which a solution can be obtained using linear regression. This results in a solution with a gradient of $1/\tau$, and an intercept of $\ln(A_0)$.

In figure 5.16 the time domain response of a 200 μm square high-stress silicon nitride membrane is shown. The measurement was made at 1.2 K, with a driving frequency of 3.401 MHz (corresponding to the $(1, 2)^{\text{th}}$ mode) averaged over 128 repetitions. The lower plot shows the response of the NEMS plotted on a logarithmic scale, with a linear fit to the first 25 ms of data. The coefficients from this fit have been used to generate the red line in the upper plot. A value of $\tau = 19.4$ ms is obtained, recalling from section 2.1 that the quality factor of a resonant system with small damping is $Q = \omega_0\tau/2$ gives a quality factor of $Q = 2.1 \times 10^5$. This value is in fair agreement with the value of

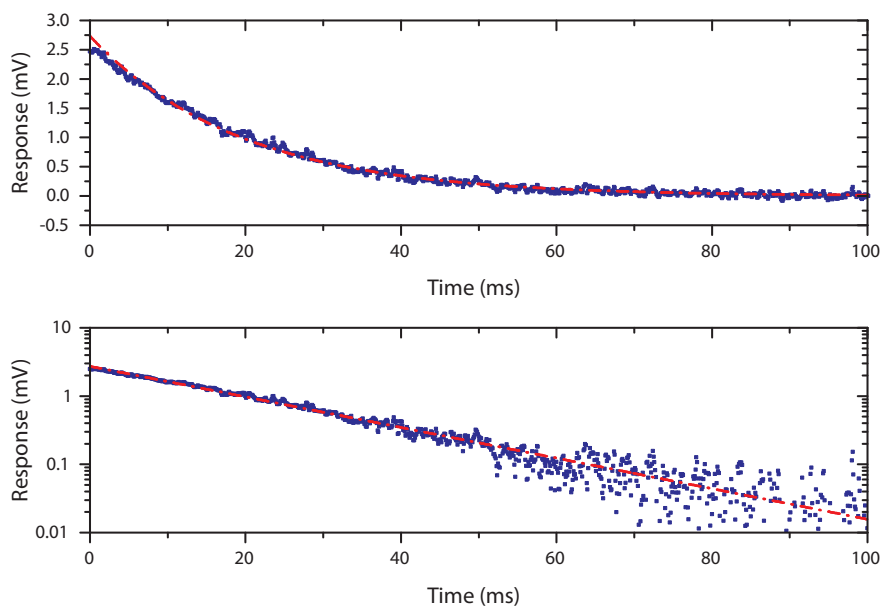


Figure 5.16: Ringdown measurements made on a $200\ \mu\text{m}$ square high-stress silicon nitride membrane driven at a frequency of $3.401\ \text{MHz}$ and averaged over 128 repetitions. The blue squares indicate experimental measurements, while the red lines show the fit to the data.

$Q = 3.1 \times 10^5$ obtained from a frequency domain analysis.

5.6 Sensitivity Calibration Using a Quartz Tuning Fork

Measurements to test the frequency response and calibrate the responsivity of the interferometer were made on quartz tuning forks³¹. A microscope image of one of these forks which have a resonant frequency of $32.768\ \text{kHz}$ ($2^{15}\ \text{Hz}$) and quality factors of order 10^5 [76, 77] is shown in figure 5.17. They are normally used as the frequency standard in clocks and watches, but have also found applications in physics as sensors for scanning probe systems [76, 78–81] and in studying the dynamics of quantum fluids [77, 82].

The quartz crystal is machined into the shape of a tuning fork and electrodes de-

³¹Epson Toyocom C-005R

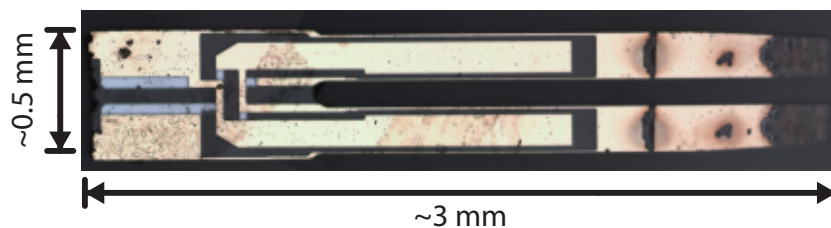


Figure 5.17: Optical microscope image of a quartz tuning fork used in these measurements.

positioned (as shown in the image). A voltage applied to the fork will cause the tines to move, which induces a current within the fork that was detected using a lock-in amplifier with built-in IV converter³².

There is a linear relation between the current induced within the fork (I) and the tine displacement from equilibrium (x). The constant α is referred to as the piezo-electro-mechanical constant and describes the charge upon the electrode, Q , per unit displacement from equilibrium, x . If the current within the fork is known from measurements it can be related to the tine displacement by:

$$\begin{aligned}
 Q &= \alpha x \\
 I &= \alpha \dot{x} \\
 I_{rms} &= \alpha \omega x_{rms} \\
 I &= 2\pi f \alpha x
 \end{aligned}
 \tag{5.8}$$

Using this equation it is possible to convert the induced current within the fork to a displacement. One tine of the fork is affixed to a sample holder using a non-conductive epoxy. The fork motion is measured by positioning the optical spot onto the tip of the free tine. The oscillation of the fork causes a modulation of the cavity length, which can be converted to a displacement. In the following sections the optical calibration of the interferometer is discussed and optical measurements of a quartz tuning fork presented. The optical and electrical measurements are then compared and a value for

³²Stanford Research Systems SR830

the fork constant calculated. By comparing the fork constant to values published in the literature the optical calibration of the interferometer was confirmed.

5.6.1 Optical Measurements of a Quartz Tuning Fork

Optical measurements of the motion of the quartz tuning fork were made by focussing the light from the fibre onto the tip of the fork. A HeNe laser ($\lambda = 633$ nm) was used, as the cavity formed needs to be between the fibre and the fork as light reflected from the end of the fork must be coherent with the $\sim 4\%$ of light reflected at the air-fibre interface. In this way it was possible to measure the modulation in the length of the optical cavity due to the motion of the fork.

Sensitivity Calibration

The interferometer responsivity was determined by changing the overall length of the cavity. As the cavity length was changed, the intensity as a function of change in cavity length ($I(z)$) was recorded. This change in intensity is described by:

$$I(z) = A_0 \cos\left(\frac{4\pi z}{\lambda} + \delta\right) + C_0 \quad (5.9)$$

Here A_0 is related to the magnitude of the sinusoidal function, λ is the wavelength of the light, δ is a phase angle that describes the starting position of the fork within the cavity and the dc offset of the system is C_0 . A dc voltage, V is applied to the z positioner, which produced a linear extension of the piezoceramic element in the stage of $z = C_p V$. The constant, C_p , allows the voltage applied to the positioning stage to be converted to a displacement.

An example of the intensity pattern obtained when sweeping the cavity length is shown in figure 5.18. Here the dc light level recorded while sweeping the z-position of a quartz tuning fork at 4.2 K is shown along with a least-squares fit to equation 5.9.

By obtaining values for the fit parameters the responsivity, the change in the detected signal with cavity length, $\frac{dI}{dz}$, can be determined from:

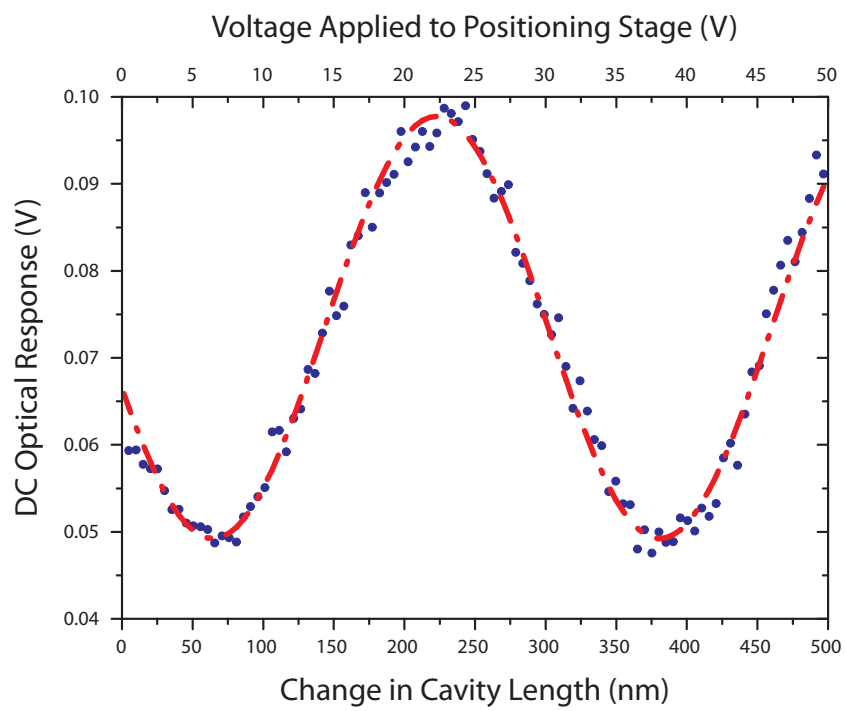


Figure 5.18: Graph showing the detected dc optical signal as a function of z position at 4.2 K. The red line shows a least squares fit to the data.

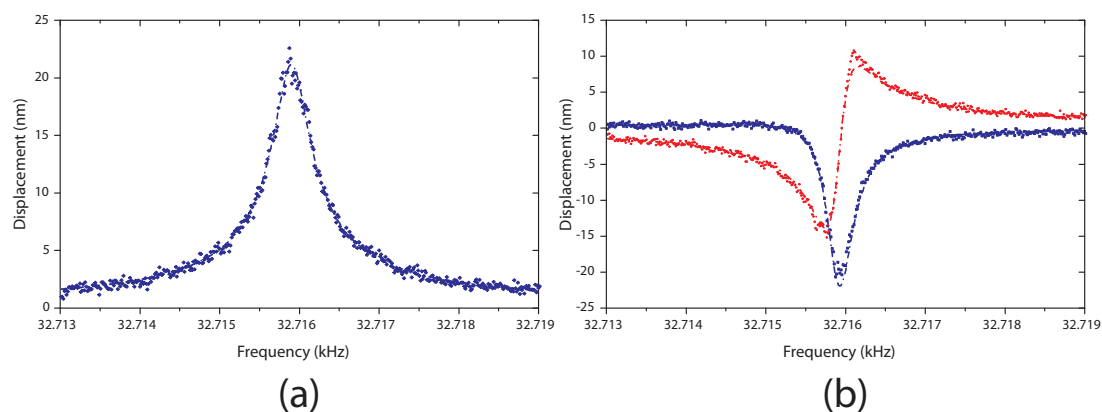


Figure 5.19: Optical measurements of a Quartz Tuning Fork made at 4.2 K, experimental datapoints are indicated by the points, with the lines of best fit shown by the dashed lines. (a) shows the absolute displacement of the fork, while (b) shows the X (blue) and Y (red) channels of the lock-in amplifier.

$$\frac{dI}{dz} = -\frac{4\pi A_0}{\lambda} \sin\left(\frac{4\pi z}{\lambda} + \delta\right) \quad (5.10)$$

From this relation we can extract the maximum responsivity of the interferometer $\frac{4\pi A_0}{\lambda}$ and obtain a value for the conversion factor from a voltage to displacement (at maximum responsivity) of $768 \mu\text{V}/\text{nm}$ for the dc output of the transimpedance amplifier. Recalling from section 5.3.4 that the gain of the ac output of the amplifier is 40 times that of the dc allows the responsivity to be scaled. This yields an ac responsivity of $30.7 \text{ mV}/\text{nm}$, which is used to calculate the fork displacement as the frequency is swept.

Optical Measurements of a Quartz Tuning Fork

Optical measurements as the fork is swept through resonance were made to allow the quality factor and optical displacement on resonance to be measured. An example of a frequency response measurement calibrated using the values obtained in the previous section is shown in figure 5.19.

To the displacement data a Lorentzian has been fitted and the resonant frequency

and quality factor extracted. These were $Q = (81.64 \pm 0.15) \times 10^3$ and $f_0 = (32.716 \pm 0.001) \times 10^3$ Hz, which give good agreement with the values obtained from an electrical measurement carried out at the same time ($Q = 93.71 \times 10^3$ and $f_0 = 32.716$ kHz). The difference in the values of the quality factors for the two measurement techniques may arise from the frequency dependent background associated with the parallel capacitance of the quartz tuning fork [76, 81]. Failing to account for this background signal in the fit to the data could explain the difference in measured quality factors.

These measurements were made during an initial run of the system, where there was a leak from the main bath into the IVC. Measurements were made while pumping directly on the IVC using a rotary pump, however a low pressure of helium was present in the sample space, which explains the lower than expected quality factor and resonant frequency. It was however suitable to demonstrate the ability of the interferometer to measure displacements on the nanometer scale.

5.6.2 Comparison of Electrical and Optical Quartz Tuning Fork Measurements

In order to confirm the validity of the responsivity calibration carried out the current induced within the fork was compared to the displacement amplitude. As discussed earlier the responsivity of the interferometer is related to the position of the fork within the cavity; any drift in the vertical position, or misplacement of the fork will reduce the responsivity. In order to overcome this the oscillation amplitude of the fork on resonance was measured as the z position was varied. This allowed the amplitude of the fork to be measured at every responsivity within the cavity. From this the displacement amplitude of the fork was calculated. This measurement was repeated at a range of drive amplitudes and optical powers to produce the plot shown in figure 5.20.

A straight line fit to the data was carried out and the gradient, equal to $2\pi f\alpha$, calculated. Averaging the result for each dataset gives a value for alpha of $2.18 \pm 0.06 \mu\text{Cm}^{-1}$. Table 5.3 shows fork constants measured by other groups on different size

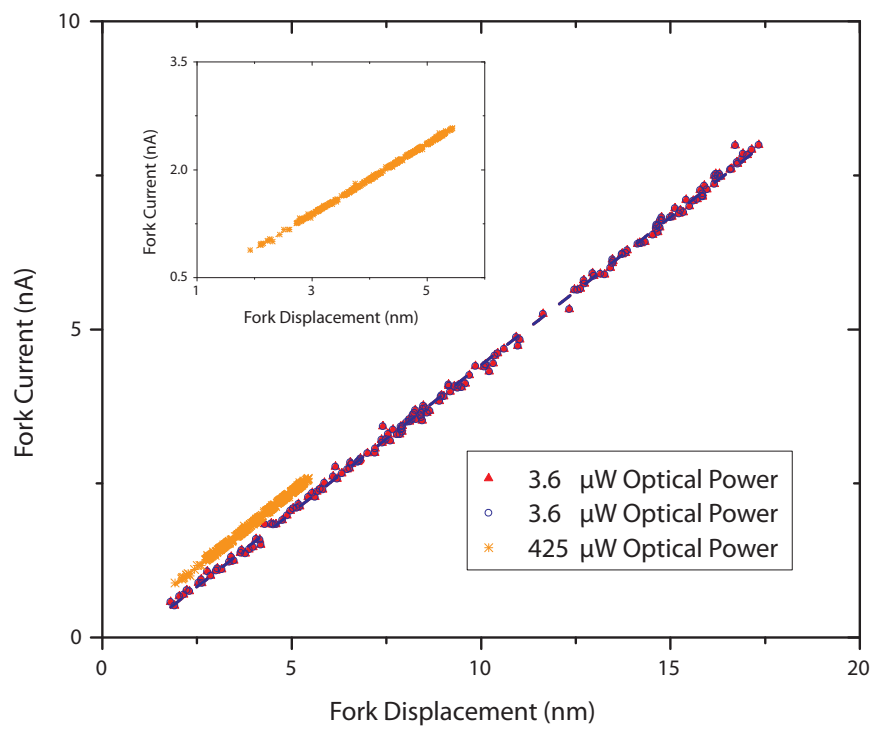


Figure 5.20: Fork displacement against current induced in fork at a range of drive amplitudes and optical powers. The inset plot shows a close-up view of the 425 μW data.

forks.

The value obtained using the setup in Nottingham gives very good agreement with measurements made by other groups on forks of similar dimensions. Any variation can be accounted for by the position of the optical spot on the tine of the tuning fork, for maximum accuracy this spot should be at the very end of the tine. While the spot was positioned as accurately as possible to maximise the signal, this may not correspond to the point of maximum displacement. The value obtained for α shows very good agreement with the other values that have been measured and gives confidence that the interferometer responsivity has been calibrated reliably.

5.7 Summary

In this chapter the design and construction of the interferometer has been described. Measurements of a range of nanomechanical devices have been presented that demonstrate the different modes of operation of the interferometer.

In order to verify that the responsivity of the interferometer operating in the two-beam interference mode is correct, measurements were made on a quartz tuning fork and a value for the piezo-electro-mechanical constant were made of $\alpha = 2.18 \pm 0.06 \mu\text{Cm}^{-1}$ obtained, which is in good agreement with the values published in the literature.

Fork Length [mm]	α [$\mu\text{C}/\text{m}$]	Measurement Method Method	Ref.
~ 2	2.18 ± 0.06	As discussed	–
1.7	2.09 ± 0.06	Optically	[77]
1.7	1.90	Electromechanically	[77]
~ 3	4.26 ± 0.06	Optically	[76]
3.2	4.90 ± 0.11	Optically	[83]

Table 5.3: Comparison of α values measured by several groups.

Chapter 6

Measurements of High-Stress Silicon Nitride Membranes

In this chapter results from dissipation measurements of square ($200 \times 200 \mu\text{m}$) and circular ($r = 100 \mu\text{m}$) membranes of high-stress silicon nitride with a thickness of $\sim 125 \text{ nm}$ are presented. These membranes were fabricated using the process outlined in Chapter 4 using substrates grown at the Cornell Nanoscale Science and Technology Facility. The silicon nitride should possess almost identical mechanical and thermal properties to that used in the work by Wilson-Rae [29], Adiga [30] and Southworth [33].

Membranes were fabricated on a 1 cm^2 square silicon substrate with centre to centre separations of $250 \mu\text{m}$ such that the majority of the sample surface was covered. A typical membrane thickness was measured to be $\sim 100 \text{ nm}$ (see section 4.5.1), two or three times thicker than those measured in previous work [29–31, 33]. This increased thickness results in a stiffer membrane which combined with an increase in the interface area with the substrate leads to an increase in dissipation through clamping losses.

6.1 Frequency Dependence

In Chapter 2 expressions for the resonant frequency of membranes (of thickness h) were derived, which were for a rectangular membrane (of sides $a \times b$):

$$\omega_{n,m} = \pi c \sqrt{\frac{n^2}{a^2} + \frac{m^2}{b^2}} \quad (6.1)$$

and a circular membrane (of radius a):

$$\omega_{n,m} = \frac{\zeta_{n,m} c}{a} \quad (6.2)$$

where c is the speed of the sound within the membrane, $c = \sqrt{\sigma/\rho}$, with stress σ , density ρ and $\zeta_{n,m}$ representing the m^{th} zero of the n^{th} Bessel function of the first kind.

The silicon nitride from which the membranes were fabricated had an initial intrinsic stress of ~ 1.2 GPa¹. When the membrane is released there will be a local deformation of the membrane which will result in a decrease of stress within the membrane [29]. The actual stress in the membrane can be determined by examining the ratio of the frequency between the fundamental and higher harmonics.

The rectangular membranes studied in this work were designed to have sides of equal length ($a = b$). Due to processing tolerances they will not be a perfect squares, but by examining the difference in frequency between asymmetric modes (for example $(1, 2)^{\text{th}}$ and $(2, 1)^{\text{th}}$) the lengths are seen to lie within 4 % of one another and we are able to describe the membrane in terms of a mean side length, L . This allows us to rewrite equation 6.1 as $\omega_{n,m} = \pi c \sqrt{n^2 + m^2}/L$, with the fundamental mode having a frequency of $\omega_{1,1} = \pi c \sqrt{2}/L$. Taking the ratio between $\omega_{n,m}$ and the fundamental mode allows us to obtain an expression for the mode number:

$$\sqrt{n^2 + m^2} = \sqrt{2} \left(\frac{\omega_{n,m}}{\omega_{1,1}} \right) \quad (6.3)$$

If we plot $\sqrt{n^2 + m^2}$ against resonant frequency we should obtain a straight line, the gradient of which is equal to $\pi c/a$. A similar approach can be taken with the circular membranes to extract the value of $\zeta_{n,m}$:

$$\zeta_{n,m} = \zeta_{0,1} \left(\frac{\omega_{n,m}}{\omega_{0,1}} \right) \quad (6.4)$$

¹As quoted by the supplier Cornell Nanoscale Science and Technology Facility

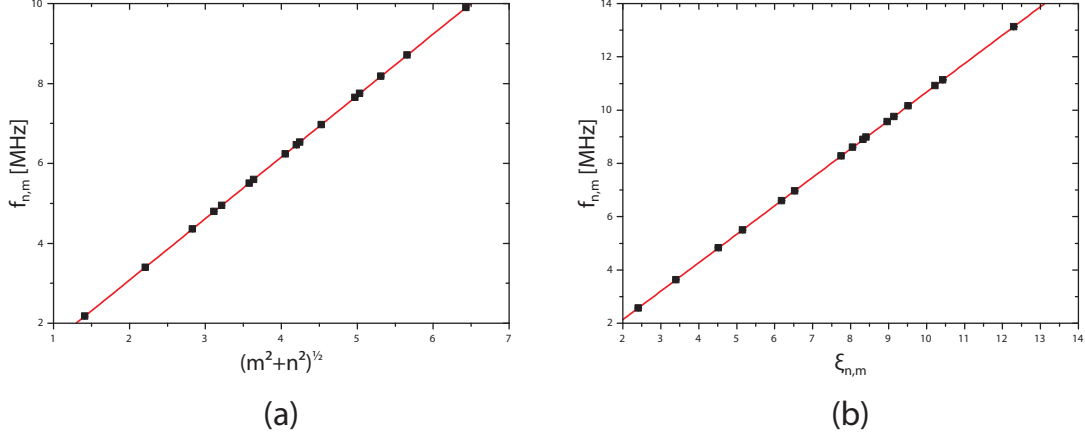


Figure 6.1: Plots of (a) $\sqrt{m^2 + n^2}$ against $f_{n,m}$ for a 200 μm membrane measured at 3.7 K and (b) $\zeta_{n,m}$ against $f_{n,m}$ for a 200 μm diameter circular membrane measured at 2.5 K. The red lines are linear fits of the data with y intercept fixed at 0.

In figure 6.1 a plot of the modal dependence against frequency is shown for square and circular membranes at 3.7 K and 2.5 K respectively. The straight lines in figure 6.1 show linear fits to the data that are constrained to pass through the origin. From the gradients of these fits values for the speed of sound within the membranes of $c_{square} = 616 \pm 15 \text{ ms}^{-1}$ and $c_{circular} = 671 \pm 12 \text{ ms}^{-1}$ were obtained.

The frequency dependence of these plots indicate that the resonators are operating within the membrane regime, where with a large tension the bending moments can be ignored. In a plate these forces needed to be accounted for and as such result in modal dependences of $f_{n,m} \propto (m^2/a^2 + n^2/b^2)$ for a square and $f_{n,m} \propto (m + 2n)^2$ for circular geometry [26].

Using the speed of sound we are able to determine the internal stress, σ of the membrane using the relation $c = \sqrt{\sigma/\rho}$. Taking $\rho = 2700 \text{ kgm}^{-3}$ [29] gives a value for the stress within the membranes of $\sigma_{square} = 1020 \text{ MPa}$ and $\sigma_{circle} = 1150 \text{ MPa}$.

Upon cooling from 300 K to ~ 4 K the membrane and substrate will undergo differential thermal contraction, introducing a compressive strain into the membrane and

reducing the internal stress. The magnitude of this thermal compression is given by the difference in the coefficients of thermal expansion (α) of silicon ($\alpha = 2.8 \times 10^{-6} \text{ K}^{-1}$) and silicon nitride ($\alpha = 2.0 \times 10^{-6} \text{ K}^{-1}$) [20]. Upon cooling by ΔT the strain induced within the membrane will be:

$$\epsilon_{SiN} = (\alpha_{T_{SiN}} - \alpha_{T_{Si}})\Delta T \quad (6.5)$$

which can be used to calculate the compressive stress contribution [20]:

$$\sigma_{SiN} = \frac{E_{SiN}}{1 - \nu} \epsilon_{SiN} \quad (6.6)$$

Using the values of α given above with values for the Young's modulus and Poisson ratio of $E_{SiN} = 211 \text{ GPa}$ and $\nu = 0.3$ respectively [84] we expect a compressive stress upon cooling from 300 K to 4 K of $\sigma_{T_{SiN}} = 71 \text{ MPa}$. In calculating this value the silicon dioxide layer is ignored as during fabrication the region beneath the membrane was removed. Any thermal contraction affecting the membrane will therefore be due to the difference in thermal expansion coefficients of the silicon nitride and the silicon substrate [64].

This compressive stress will reduce the tensile stress within the membrane from 1.2 GPa (as specified by supplier) to $\sim 1.13 \text{ GPa}$ once cooled. This gives good agreement with the values obtained from the fit to the drum data, but is out by $\sim 100 \text{ MPa}$ in the case of the square geometry. This discrepancy can be accounted for by a local deformation of the membrane during the release stage in processing. The etch holes used to allow hydrofluoric acid to the underlying silicon dioxide have a hole to hole spacing of $5 \mu\text{m}$, however their arrangement differs between membranes with the square membrane etch holes arranged on a rectangular grid, while the circular membrane has holes arranged radially about the membrane centre producing a hexagonal arrangement. The hexagonal arrangement of holes in a circular membrane might allow the membrane to retain the tensile stress better when compared with the long rows of holes that run across the surface of the square membrane.

After the low temperature measurements were made the membranes were allowed to warm back up to room temperature, where the internal stress of square membrane was measured to be 1050 GPa. When compared to $\sigma_{square} = 1020$ MPa at 3.7 K this shows a decrease upon cooling of just 30 MPa less than half that predicted from the compressive stress calculation. This may be due to these measurements being made after the low temperature set with the thermal cycling affecting the overall stress within the membrane.

6.2 Thermoelastic Damping

Much of the behaviour observed in the membranes studied as part of this work can be described in terms of the theory of elasticity as presented by Landau and Lifshitz [85]. In this section we will use this framework to describe the behaviour of the flexural modes of a membrane and see how this can be used to predict the fQ floor bought about through thermoelastic damping and how this then relates to our experimental measurements.

The membrane discussed here is a square membrane with sides of length L and a thickness h with the membrane centre lying at $(x, y, z) = (L/2, L/2, 0)$. The membrane motion is described in terms of a neutral plane that lies in the centre of the membrane and does not undergo compression or extension when the membrane is bent. This plane lies in the centre of the membrane at $z = 0$ with the displacement of this plane defined by equation 2.15 which is reproduced here:

$$\xi(x, y)e^{-i\omega t} = \xi_0 \sin(\alpha x) \cos(\beta y)e^{-i\omega t} \quad (6.7)$$

where ξ_0 is the amplitude of displacement and ω the mechanical frequency. The values $\alpha = m\pi/L$ and $\beta = n\pi/L$ define the node structure within the membrane. In the limit of small displacements any transverse motion of the membrane can be ignored and we simply state that $z = \xi(x, y)$. The free energy per unit volume within the membrane can then be written as [85, 86]:

$$F = z^2 \frac{E}{1 + \nu} \left\{ \frac{1}{2(1 - \nu)} \left(\frac{\partial^2 \xi}{\partial x^2} + \frac{\partial^2 \xi}{\partial y^2} \right)^2 + \left[\frac{\partial^2 \xi}{\partial x \partial y} - \frac{\partial^2 \xi}{\partial x^2} \frac{\partial^2 \xi}{\partial y^2} \right] \right\} \quad (6.8)$$

which when integrated over the membrane volume yields the total energy within the system:

$$U = \frac{Eh^3}{24(1 - \nu^2)} \int_0^L \int_0^L \left[(\nabla^2 \xi)^2 + 2(1 - \nu) \left\{ \left(\frac{\partial^2 \xi}{\partial x \partial y} \right) - \frac{\partial^2 \xi}{\partial x^2} \frac{\partial^2 \xi}{\partial y^2} \right\} \right] dx dy \quad (6.9)$$

When determining the quality factor of a system we are interested in the fraction of this energy lost over one cycle, $Q = 2\pi U / \Delta U$ [86]. One dissipation mechanism present at room temperature is thermoelastic damping. Figure 6.2 shows a plot of the dissipation in even ($m = n$) modes of a 200 μm square membrane measured at 300 K. In previous measurements of membranes it was seen that the dissipation in even modes exhibits a strong modal dependence, decreasing as the mode number increases [29]. This behaviour is due to the destructive interference of elastic waves within the membrane minimising clamping losses and is observed in this data up to a frequency of 13 MHz at which point the dissipation mechanism changes and an increase in dissipation is observed tending towards a constant fQ product, indicative of thermoelastic damping.

In these measurements we see an fQ floor of 0.5 THz, indicated by the red line in figure 6.2. At lower temperatures this fQ floor is no longer visible, indicating a temperature dependent mechanism, the most likely of which is the thermoelastic effect.

For an elastic solid with a non-zero coefficient of thermal expansion, α , a deformation will lead to a localised heating and cooling of the membrane, displacing it from thermal equilibrium. In order to return to thermal equilibrium heat must flow along the thermal gradient between these two points. This flow of heat is driven by the mechanical energy, leading to a finite Q . The time taken for the heat to diffuse across this gradient is given by the thermal diffusion time of the solid, which was defined by Lifshitz and Roukes [87] as $\tau_{th} = h^2 / (\pi^2 a)$ where a is the thermal diffusivity of the solid. In the regime where the thermal relaxation time of the phonon gas, τ_{th} is much less than the

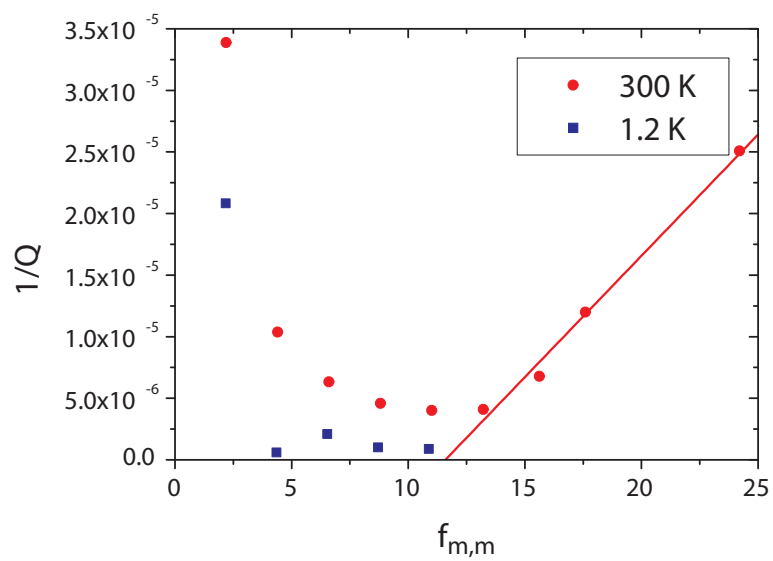


Figure 6.2: Dissipation in the even modes of a $200 \mu\text{m}$ square membrane measured at 300 K and 1.2 K. The solid line is a linear fit to the 300 K data indicating an fQ floor of ~ 0.5 THz.

period of oscillation of the strain field, $1/f_{nm}$ the thermal phonons are able to relax faster than the oscillating strain wave and thermoelastic damping will occur. When the mechanical period is shorter than $\tau_t h$ the phonons are no longer able to diffuse across the solid quickly enough and thermoelastic damping will decrease. For the 125 nm thick membranes discussed here, where the speed of sound is 616 ms^{-1} , this occurs above a frequency of $\sim 5 \times 10^9 \text{ Hz}$ and as such is not observed.

In order to quantify the dissipation due to these heat flows we return to the theory of elasticity introduced earlier and consider the even ($m = n$) flexural modes of a square membrane, which allows the expression for the membrane displacement to be rewritten as:

$$\xi(x, y)e^{-i\omega t} = \xi_0 \sin(\alpha x) \cos(\alpha y)e^{-i\omega t} \quad (6.10)$$

by using this expression to evaluate equation 6.9 for the $(m, m)^{th}$ mode we obtain an expression for the total energy within the membrane of:

$$U = \frac{Eh^3 \xi_0^2 m^4 \pi^4}{24L^2(1 - \nu^2)} \quad (6.11)$$

As the membrane undergoes flexural motion there will be periodic changes in the local strain of the membrane leading to temperature gradients between which heat will flow in order to bring the membrane back into thermal equilibrium. In order to determine the energy lost per cycle we must first determine the temperature profile across the thickness of the membrane which should satisfy the driven heat equation [10, 85, 86]:

$$\left(c_v \frac{\partial}{\partial t} - \kappa_{th} \frac{\partial^2}{\partial z^2} \right) \Delta T = \frac{E\alpha T_0 z}{3(1 - 2\nu)} \frac{\partial}{\partial t} \nabla^2 \xi e^{-i\omega t} \quad (6.12)$$

where c_v is the specific heat capacity and κ_{th} is the thermal conductivity. With the strain varying most rapidly across the thickness of the membrane we are able to ignore the relatively small transverse temperature gradients and find a temperature field of the form $T = T_0 + \Delta T(x, y, z, t)$. The strains induced within the membrane will be periodic

at the mechanical resonant frequency, so we take a solution for $\Delta T = \Theta(z)e^{-i\omega t}$ allowing equation 6.12 to be rewritten as:

$$i\omega c_v \Theta(z) + \kappa_{th} \frac{\partial^2 \Theta}{\partial z^2} = \frac{i\omega E \alpha T_0 z}{3(1-2\nu)} \nabla^2 \xi \quad (6.13)$$

$$\frac{\partial^2 \Theta}{\partial z^2} = \frac{i\omega c_v}{\kappa_{th}} \left(\frac{E \alpha T_0 z}{3c_v(1-2\nu)} \nabla^2 \xi - \Theta(z) \right) \quad (6.14)$$

which when starting from a solution of the form $\Theta(z) = A \sin(kz) + B \cos(kz)$ we obtain [87]:

$$\frac{i\omega c_v}{\kappa_{th}} \left[\frac{E \alpha T_0 z}{3c_v(1-2\nu)} \nabla^2 \xi - \Theta(z) \right] = k^2 [A \sin(kz) + B \cos(kz)] \quad (6.15)$$

where $k = \sqrt{i\omega c_v / \kappa_{th}}$. The values of coefficients A and B are determined by requiring that $\partial\Theta/\partial z = 0$ at $z = \pm h/2$, *i.e.* zero heat flow across the membrane boundary, for which the solution is:

$$\Theta(z) = \frac{E \alpha T_0}{3c_v(1-2\nu)} \nabla^2 \xi \left(z - \frac{\sin(kz)}{k \cos\left(\frac{kh}{2}\right)} \right) \quad (6.16)$$

Having determined an expression for the thermal gradient induced within the membrane by the time-varying strain we are now in a position to determine the energy lost per cycle, which is given in [86] as:

$$\Delta U \approx \frac{\pi \omega \alpha^2 E^2 d^5 T_0}{1080 \kappa_{th} (1-\nu)^2} \int_0^L \int_0^L (\nabla^2 \xi)^2 dx dy \quad (6.17)$$

for which the integral over the surface of the membrane for an even mode is:

$$\int_0^L \int_0^L (\nabla^2 \xi)^2 dx dy = \frac{n^4 \xi_0^2 \pi^4}{L^2} \quad (6.18)$$

The thermoelastic quality factor is $Q = 2\pi U / \Delta U$ [86], which by substituting in equations 6.11 and 6.17 we obtain an expression for the thermoelastic quality factor of:

$$f Q_{TE} = \frac{45 \kappa_{th}}{\pi \alpha^2 E T_0 h^2} \frac{(1-\nu)}{(1+\nu)} \quad (6.19)$$

Quantity	Value	Units	Ref.
κ_{th}	3	$\text{Wm}^{-1}\text{K}^{-1}$	[88]
α	4.8×10^{-6}	K^{-1}	[86]
c_v	2×10^6	$\text{Jm}^{-3}\text{K}^{-1}$	[86]
E	211	GPa	[20]
ν	0.3	-	[86]
T_0	300	K	-
h	125×10^{-9}	m	-

Table 6.1: Parameters used in estimating the fQ product for a square silicon nitride membrane at 300 K. The value of alpha given in this table is the linear coefficient of thermal expansion, which is related to the coefficient of volumetric expansion by $\alpha_V = 3\alpha_L$ [64]. This scaling factor is included directly in equation 6.12.

Evaluating equation 6.19 using the parameters shown in table 6.1 gives a value for fQ of 0.8 THz, very close to that observed in the experimental data. The strong agreement between the predicted fQ floor and the measured value indicates that above 13 MHz the dominant dissipation within the membrane is thermoelastic dissipation.

The fQ product in equation 6.19 has a $1/h^2$ dependence, with a decrease in membrane thickness leading to an increase in the fQ product. In the work of Adiga *et al.* where measurements were made on thinner (27 nm) circular membranes the authors suggest an fQ floor of 10 THz. Evaluating equation 6.19 for their system gives $fQ = 17$ THz, these disagreements between the theory and experimental can be attributed to the value of κ_{th} which can vary greatly between materials, in reviewing the literature there was seen to be an order of magnitude difference between quoted values. The value of κ_{th} used in these calculations was obtained from measurements of an LPCVD membrane of low-stress amorphous silicon nitride with a thickness of 180 – 200 nm [88].

In amorphous solids the phonon mean free path is of the same order as the structural disorder, this results in a size independent thermal conductivity [89]. Orbach *et al.* [90] suggest that heat transfer within amorphous solids occurs by phonons coupling to, and

hopping between, highly localised vibrational modes within the solid known as fractons. The low (but non-zero) thermal conductivity of amorphous solids suggests that the spatial overlap between adjacent fractons must be minimal. A strain applied to the solid is able to modify this overlap and in work by Alam *et al.* [89] a decrease in the thermal conductivity of silicon nitride with increasing strain was seen.

The fact that the dissipation measurements are made dynamically (with a time-varying strain) on a stressed silicon nitride membrane make it reasonable to assume that the thermal conductivity will be lower than that of an unstressed silicon nitride membrane. Using the experimentally observed fQ floor a value for κ_{th} of $1.9 \text{ Wm}^{-1}\text{K}^{-1}$ is observed, $2/3$ that given in [88]. From the measurements of Alam *et al.* [89] this corresponds to a strain of approximately 0.5 %. With a Young's modulus for silicon nitride of 211 GPa a strain of 0.4 % would equate to a stress within the membrane of $\sim 1 \text{ GPa}$, similar to the stress within the membrane determined from the frequency dependence shown earlier.

The silicon nitride used to fabricate the membranes measured as part of this work and by Adiga *et al.* [30] were grown at the same facility using the same equipment and processes and as such should have essentially identical physical properties. Repeating the fQ calculation for the Adiga membranes this time using a thermal conductivity of $\kappa_{th} = 1.9 \text{ Wm}^{-1}\text{K}^{-1}$ we obtain $fQ = 10 \text{ THz}$, identical to the value stated in [30].

6.3 Inter-Membrane Coupling

The large number of membranes present upon the surface of the substrate allowed indirect observation of nearby membranes that were able to couple into the response of the membrane under observation. An example of one of these measurements is shown in figure 6.3. The fit shown is the sum of multiple Lorentzian functions, which allows an overall response for the coupled membranes to be obtained. The quality factors and resonant frequencies shown in figure 6.3 are obtained from these individual plots.

In order to observe this effect it is essential that the resonant frequencies of the

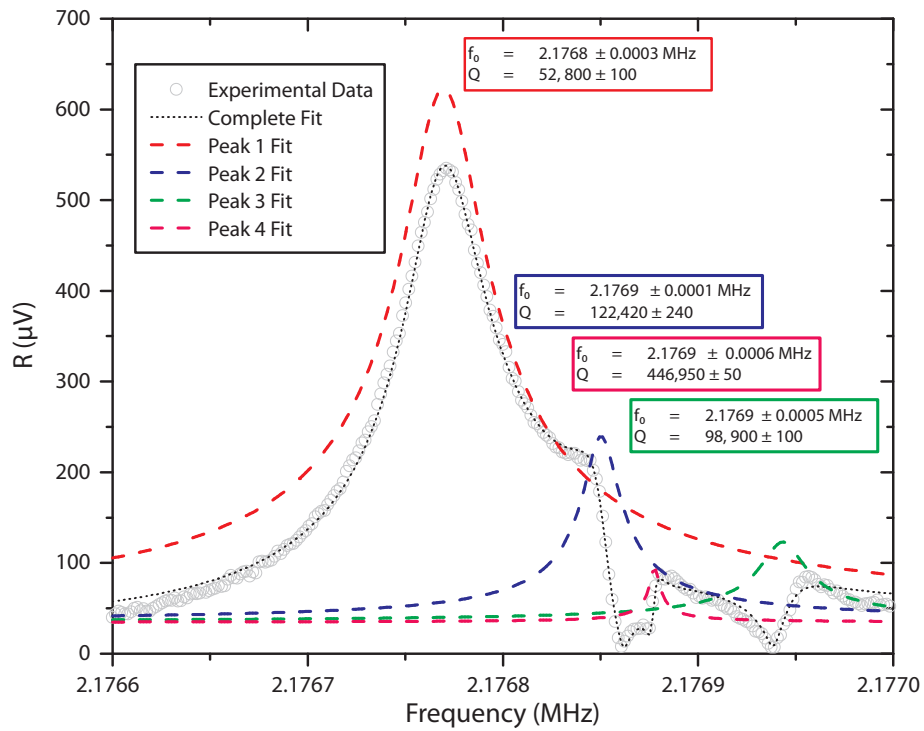


Figure 6.3: Example of intra-membrane coupling in a $200 \mu\text{m}$ square membrane of high-stress silicon nitride measured at a temperature of 2 K. Displayed is the complete fit to the experimental data along with the responses from the individual Lorentzian functions that comprise the complete response.

unobserved resonators lie within the bandwidth of the illuminated membrane. Incident acoustic waves from the nearby membranes are then able to couple into and be amplified by the mechanical resonance of the illuminated membrane. If the response lies outside the bandwidth of the illuminated mode the amplitude of the acoustic wave is insufficient to produce detectable motion within the membrane.

Looking at the difference in frequency between the observed modes it is possible to quantify the processing tolerances of the membranes on the sample. Taking values from figure 6.3 the difference in frequency between observed and unobserved modes is approximately 200 Hz. For a resonant frequency of 2.176 MHz this represents a difference of 1 part in 10^4 between membranes.

Comparing the quality factors observed we see a quality factor for the observed membrane half that of the unobserved membrane. This damping could arise in two ways: through a heating of the membrane by the optical spot or by the optical field exerting a force on the membrane, amplified by the low-finesse cavity of which the membrane is part. In order to determine whether one of these is responsible for the heating of the membrane we will estimate their effect.

6.3.1 Optical Heating

The amount of optical power absorbed by the silicon nitride can be determined by the optical absorption coefficient, α which for silicon nitride is 150 dB/m [91]. A 125 nm thick sheet of silicon nitride will therefore attenuate the incident light by $A = 2 \times 10^{-5}$ dB. The fraction of optical power absorbed is therefore equal to $\gamma = 1 - 10^{-0.1A}$. In these measurements the optical powers used were typically of order ~ 50 nW, resulting in the membrane absorbing 0.2 pW during one passage through the membrane. At the silicon substrate the reflectivity is $R \sim 0.5$ at 633 nm, so on the return trip a further 0.1 pW will be absorbed, giving a total power absorbed by the membrane of $P_0 = 0.3$ pW.

In order to simplify things we assume that the membrane is circular with a radius of $R_2 = 100 \mu\text{m}$ and the optical power is deposited into the membrane in a spot of radius $R_1 = 0.5 \mu\text{m}$ positioned at the membrane centre. The difference in temperature between

the edge of the optical spot and the edge of the membrane (assumed to be heat sunk to the fridge temperature) is given by the solution to Fourier's equation:

$$\Delta T = \frac{-P_0}{2\pi\kappa_{th}h} \ln\left(\frac{R_2}{R_1}\right) \quad (6.20)$$

where κ_{th} , the thermal conductivity for silicon nitride is $5 \times 10^{-2} \text{ Wm}^{-1}\text{K}^{-1}$ at 2 K [92]. This gives a value for the difference between the membrane perimeter and centre, $\Delta T \sim 50 \mu\text{K}$. If optical heating was responsible for the difference in quality factors observed between membranes then a change in bath temperature of $5 \mu\text{K}$ should halve the quality factor (doubling the dissipation). As an indicator of the temperature change required we can revisit the work of Southworth *et al.* [33]. Figure 2.9 shows dissipation as a function of temperature in high-stress membranes we see that in order to double the dissipation seen at 2 K ($1/Q \sim 4 \times 10^{-7}$) requires a temperature rise of more than 10 K. When compared with the magnitude of the required temperature change this temperature change due to optical heating is so small that at this temperature it cannot be responsible for the reduced quality factor of the observed membrane.

Having obtained a value for ΔT it is now useful to look at how this heating will vary as the temperature decreases. For a dielectric at low temperatures the thermal conductivity will scale as T^3 [64] which if we assume a spatially homogeneous value for κ_{th} allows us to estimate the optical heating of the membrane at lower temperatures, the results of which are shown in Table 6.2.

From this calculation we see that as the bath temperature is decreased so too does κ_{th} , leading to an increase in the magnitude of the optical heating. At a temperature of 0.2 K the difference in temperature between the membrane edge and centre would be 50 mK, a difference of 25 %. This would most likely have an effect on the mechanical response of the observed membrane. Using the inter-membrane coupling however it would be possible to indirectly observe surrounding membranes that are still at 50 mK without reducing the optical power. As stated earlier we have assumed a spatially homogeneous value for κ_{th} , however moderate heating will change the value of κ_{th} and so the estimates

T_0	ΔT	$\Delta T/T_0$
2.0 K	50 μ K	2.5×10^{-5}
1.0 K	400 μ K	4.0×10^{-4}
0.5 K	3.2 mK	6.4×10^{-3}
0.2 K	50 mK	0.25
0.1 K	400 mK	4.0

Table 6.2: Estimate of the optical heating experienced by a membrane as the temperature decreases with $\kappa_{th} \propto T^3$ [64].

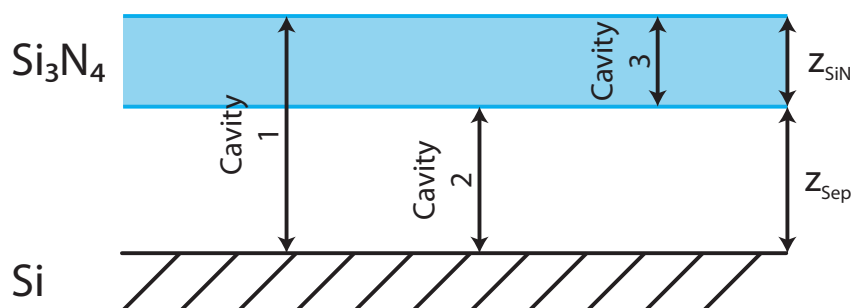


Figure 6.4: Magnitude of the optomechanical force for the silicon nitride setup as the cavity length is varied. The red dot indicates the positioning of the silicon nitride membrane in these measurements.

given in Table 6.2 are upper limits on heating caused by an optical spot.

6.3.2 Optomechanical Forces

Light incident on the membrane will exert a radiation pressure that will work to damp the vibrational motion of the membrane. The magnitude of this force will be amplified by the three optical cavities formed within the membrane shown in figure 6.4.

Within the cavity reflections will occur at three points, the two surfaces of the silicon nitride and the silicon substrate. Each reflection will affect the motion of the resonator

to a different extent dependant upon the separation of the two reflective surfaces. As the membrane moves on resonance there will be a change in z_{sep} which will modify the force, with the gradient of this force leading to either a damping or an amplification of the mechanical mode.

The mathematical description of this cavity is non-trivial and unfortunately it was not possible to quantify the magnitude of the optomechanical effect in the time available. Having ruled out optical heating as a source of damping in the observed membrane it is highly likely that an optomechanical force is damping the cavity.

6.4 Summary

In this chapter several results from measurements of a high-stress silicon nitride membrane have been presented. Through analysis of the resonant frequencies of the harmonics it was possible to determine the stress present in the membrane after cooling and attribute much of it to differential thermal contraction between silicon and silicon nitride. In studying the dissipation of these membranes at room temperature a trend towards an fQ floor of 0.8 THz was observed in the even modes whose resonant frequency is above 13 MHz. Using the theory of elasticity [85] we were able to show that this dissipation arises from thermoelastic effects. From this analysis a thermal conductivity $\sim 2/3$ that published in the literature was observed. This decrease is due most likely to the internal stress of the silicon nitride modifying the spatial overlap of fractons within the solid.

Inter-membrane coupling was also discussed, where the vibrational mode of the observed membrane is able to amplify acoustic waves radiated from nearby unobserved membranes. The observed quality factor is considerably lower than that of the unobserved modes suggesting that an optical effect may be damping the observed mode. In attempting to determine the source of this damping we were able to exclude optical heating as the cause and showed that as the temperature (and the thermal conductivity) is decreased optical heating will increase, which makes inter-membrane coupling an ideal

method by which to observe nearby membranes at mK temperatures without optically heating them.

The second possible cause for the observed membrane damping are optomechanical forces, the cavity arrangement makes a mathematical description of this system difficult and unfortunately it was not possible to quantify the effect that optomechanical forces may have on the membrane.

Chapter 7

Summary and Future Work

7.1 Summary

In this thesis a fibre interferometer capable of detecting nanomechanical motion at low temperatures has been designed and built. The fibre interferometer was mounted on the mixing chamber of a commercial dilution refrigerator and used to successfully measure both micro- and nano-mechanical devices.

In order to confirm the behaviour of the interferometer, measurements on quartz tuning forks were made at liquid helium temperatures. From these measurements it was possible to extract a value for the piezo-electro-mechanical coupling constant of $\alpha = 2.18 \pm 0.06 \mu\text{Cm}^{-1}$, in good agreement with the values published in the literature.

High-stress silicon nitride has been identified as a material able to exhibit very high-quality factors due to the intrinsic stress. With an interferometric setup it is possible to measure the dissipation in pure dielectrics such as silicon nitride, for which high quality factors have been observed. As part of this work fabrication recipes for a number of nanomechanical devices made of silicon nitride have been developed, and results from measurements of a number of these devices presented. In addition to performing frequency response measurements it has also been possible to confocally image nanomechanical resonators with a resolution of ~ 750 nm, a value only just above the diffraction limit of 633 nm imposed by the wavelength of the light.

A modal analysis of the resonant frequencies of square and circle high-stress silicon nitride membranes allowed the internal stress of these devices to be calculated. An examination of the modal dependence of the even ($m = n$) modes of these membranes at room temperature showed a regime of dissipation via thermoelastic damping with the fQ floor tending towards a value of 0.8 THz that can be predicted by the theory of elasticity. From this fQ floor the thermal conductivity of the membrane can be calculated which is in good agreement with thermal conductivity measurements made of low-stress silicon nitride subjected to a level of strain comparable to the intrinsic stress of the membranes.

Measurements of the silicon nitride membranes at low temperatures (2-4 K) revealed inter-membrane coupling for the fundamental mode of square membranes. When comparing quality factors between observed and unobserved modes a lower quality factor in the observed mode was seen that is most likely due to optomechanical damping. In determining the likely cause of these differences in quality factor, the optical heating was evaluated, for which there will be significant optical heating of the membrane at temperatures below 0.5 K. In this instance the inter-membrane coupling would allow the observation of the surrounding modes that will be at T_0 without requiring a decrease in the optical power.

The thermoelastic damping seen in silicon nitride membranes at room temperature was analysed with respect to the even modes of a square membrane it would be of interest to extend the mathematical description of thermoelastic damping included in this thesis to allow analysis of the odd modes to determine the extent to which thermoelastic damping is affecting them.

Three-paddle torsional resonators fabricated from high-stress silicon nitride were fabricated for measurement using the interferometer, but due to time constraints it was not possible to detect torsional motion in these devices. The dissipation in torsional modes of low-stress silicon nitride membranes have been studied which displayed a strong relation between mode and quality factor. The effect of stress on these torsional modes is unclear but using the fabrication techniques developed and the interferometer it should

be possible to study this effect.

7.2 Future Work

During this work the dilution refrigerator was beset by problems and was unable to cool sufficiently to allow the measurement of membranes at temperatures below 1 K. Determining and resolving the cause of this inability to cool would allow measurements on the dissipation in these devices at temperatures lower than 1 K to be performed. This would be of great interest, as to date measurements below 1 K of silicon nitride have been performed magnetomotively [20, 21] which requires devices that are fabricated with a layer of gold to allow actuation, thereby modifying the physical properties of the high-stress silicon nitride.

The membranes measured in this work were several times thicker than membranes measured in other work, resulting in increased clamping losses and a lower observed quality factor when compared with thinner membranes of comparable lateral dimensions. In order to determine the effect that thickness has on clamping losses it would be of interest to fabricate thinner membranes to study the effect of thickness on dissipation. This should hopefully allow a family of modes to be identified for which dissipation through clamping loss is minimal and the dominant dissipation mechanism is material based.

For vibrational modes with dissipation identified as being material loss dominated a systematic study of the temperature dependence of dissipation below 1 K could be performed. In previous work carried out in Nottingham a strongly temperature dependent dissipation was observed below 1 K for doubly clamped beams of high-stress silicon nitride coated with a layer of gold to detect motion magnetomotively. Through a dissipation study using optical techniques it would be possible to investigate the effect that the metallic layer has on the mechanical properties of the silicon nitride.

It was not possible to detect the torsional modes of three-paddle resonators fabricated as part of this work. This is due to the inertial actuation method used which couples

preferentially to the flexural modes of oscillation. In the future it would be of interest to explore the effect of stress on the quality factors of the torsional modes. The actuation of the torsional modes may be achievable using inertial actuation but failing that an rf coil could be used to produce a time-varying magnetic field that could induce motion in a resonator patterned with a magnetic layer. If successful, these high-stress torsional resonators could be used to perform torque magnetometry studies of magnetic materials.

7.3 Conclusion

In conclusion the interferometer fabricated as part of this work has shown itself to be a versatile tool capable of measuring nanomechanical motion from room temperature down to liquid helium temperatures. Initial measurements of high-stress silicon nitride membranes have shown behaviour in agreement with work being carried out by other groups, and have highlighted the role of thermoelastic dissipation in high-stress silicon nitride membranes at room temperature. It has also been possible to detect coupling between nearby membranes allowing the indirect detection of motion in these other coupled devices.

Appendix A

Fabrication Recipes

Detailed fabrication recipes for the devices discussed in this thesis are presented in this thesis to supplement the information given in Chapter 4.

The processes consist of three main parts. Defining the alignment marks via optical lithography and metallization (section A.2), defining the location markers via electron-beam lithography and metallization (section A.3) and finally fabricating the nanomechanical structures via electron-beam lithography and etching (section A.4).

A.1 Reactive Ion Etch Recipes

Two reactive ion etch recipes are used in the processes described in this appendix. The recipe settings for the Corial 200IL system are shown in table A.1. Process times are given in the following sections.

A.2 Alignment Mark Metallization

1. The substrate is cleaved into 9.8×9.8 mm squares, followed by a four solvent cleaning process (ethyl lactate, acetone, methanol and isopropyl alcohol (IPA)) at 20 °C, 5 minutes per solvent with ultrasonic agitation.

Process Name	A_Descum_Graphite	A_SiO2_RIE
Gas (Flow Rate)	O ₂ (25 sccm)	CHF ₃ (100 sccm) O ₂ (5 sccm)
Working Pressure	10 mT	50 mT
RF Forward Power	60 W	150 W
RF Bias	-350 V	-490 V
Shuttle Temperature	20 C	20 C
Shuttle Material	Graphite	Graphite

Table A.1: RIE recipe settings used in these processes.

2. The samples are baked at 115 °C for 10 minutes to dehydrate them.
3. The samples are coated with a 1.4 μm thick layer of AZ5214E¹ photoresist by spinning at 5,000 rpm for 45 seconds followed by baking on a hotplate at 110 °C for 50 seconds. After baking the samples are soaked in toluene for 5 minutes to toughen the top layer of the resist.
4. The alignment marks are then exposed through an optical mask at a power of 12 mW/cm² for 7.8 s. The sample is developed in AZ726MIF (metal-ion free) developer for 15 seconds followed by a rinse in DI water.
5. A 60 second O₂ descum step (A_Descum_Graphite) is then performed to remove any residual resist from the exposed regions. This is followed by a 30 second silicon dioxide reactive ion etch to roughen the nitride surface and improve the adhesion of the metallic film (A_SiO2_RIE).
6. The samples are then loaded into a thermal evaporator, where a 30 second argon plasma clean is carried out.
7. The pattern is then transferred to the sample by thermally evaporating 5 nm of

¹AZ5214E is an image reversal resist, but in this work it is used in positive tone

chrome and 50 nm of gold onto the sample. This is done at a pressure below 10^{-6} mBar at a rate of ~ 0.2 nm/s.

8. Lift-off of the unwanted metal is achieved by soaking the sample in acetone at 50 °C followed by a two solvent clean (methanol and IPA), 5 minutes per solvent at 20 °C with ultrasonic agitation.

A.3 Location Marker Definition

1. A sample patterned with alignment markers is given a four solvent cleaning process (ethyl lactate, acetone, methanol and isopropyl alcohol (IPA)) at 20 °C, 5 minutes per solvent with ultrasonic agitation.
2. The sample is coated with a 450 nm thick layer of 495 k PMMA (A5, 5% in anisole) electron-beam resist by spinning at 5,000 rpm for 45 seconds followed by baking on a hotplate at 180 °C for 60 seconds.
3. The location markers are exposed at an acceleration voltage of 30 kV and a current of 500 pA. A dwell time of 550 ns is used, which is equivalent to an area dose of $275 \mu\text{C}/\text{cm}^2$.
4. The exposed sample is developed in a solution of 3 parts IPA to 1 part methyl isobutyl ketone (MIBK) for 120 seconds followed by a rinse in IPA and blow drying with nitrogen.
5. A 60 second O_2 descum step (`A.Descum.Graphite`) is then performed to remove any residual resist from the exposed regions. This is followed by a 30 second silicon dioxide reactive ion etch to roughen the nitride surface and improve the adhesion of the metallic film (`A.SiO2.RIE`).
6. The samples are then loaded into a thermal evaporator, where a 30 second argon plasma clean is carried out.

7. The pattern is then transferred to the sample by thermally evaporating 5 nm of chrome and 50 nm of gold onto the sample. This is done at a pressure below 10^{-6} mBar at a rate of ~ 0.2 nm/s.
8. Lift-off of the unwanted metal is achieved by soaking the sample in acetone at 50°C followed by a two solvent clean (methanol and IPA), 5 minutes per solvent at 20°C with ultrasonic agitation.

A.4 Nanomechanical Device Fabrication

A.4.1 Membranes

1. The sample is given a four solvent clean (ethyl lactate, acetone, methanol and isopropyl alcohol (IPA)) with ultrasonic agitation.
2. The sample is coated with a 450 nm thick layer of 495 k PMMA (A8, 8% in anisole) electron-beam resist by spinning at 5,000 rpm for 45 seconds followed by baking at 180°C on a hotplate for 60 seconds.
3. An electron-beam lithography exposure is carried out at an acceleration voltage of 30 kV and a current of 500 pA. An array of $\sim 1\ \mu\text{m}$ holes separated by $5\ \mu\text{m}$ are patterned over an area equal to the desired membrane dimensions. A dwell time of ~ 1500 ns is used, equivalent to an area dose of $\sim 750\ \mu\text{C}/\text{cm}^2$.
4. The exposed sample is developed in a solution of 3 parts IPA to 1 part methyl isobutyl ketone (MIBK) for 120 seconds followed by a rinse in IPA and blow drying with nitrogen.
5. The sample is given a 20 second oxygen plasma descum (A_Descum_Graphite) followed by a CHF_3/O_2 reactive ion etch (A_SiO2_RIE) for between 300 and 360 seconds.
6. Any residual PMMA is removed by soaking in Microchem Remover PG at $\sim 70^\circ\text{C}$, followed by a rinse in DI water.

7. Before wet etching the sample is wetted by placing it first in acetone, before transferring to methanol, IPA and then DI water without allowing it to dry.
8. The sample is then transferred from the DI water into hydrofluoric acid for 240-300 seconds.
9. After etching, the sample is rinsed by soaking in several DI water baths, before being transferred to IPA. Care must be taken to ensure that the sample does not dry when being transferred between baths to protect the membrane from collapsing. Once in the IPA the sample and 10 ml of IPA are loaded into a Tousimis Samdri 215B critical point dryer.
10. The chamber of the critical point drier is slowly pressurised to ~ 1000 PSI with liquid carbon dioxide over a period of 60 seconds. The carbon dioxide and IPA mixture is then flushed through using a steady flow of pure liquid carbon dioxide for 4 minutes, at the end of which the chamber is sealed and heated to drive the carbon dioxide to the supercritical regime.
11. Once in the supercritical regime the pressure in the chamber is isothermally reduced (at a flow rate of ~ 5 SCFH), allowing the supercritical carbon dioxide to evaporate with no surface tension.

A.4.2 Direct Fabrication of Torsional Resonators

1. The sample is given a four solvent clean (ethyl lactate, acetone, methanol and isopropyl alcohol (IPA)) with ultrasonic agitation.
2. The sample is coated with a 200 nm thick layer of 495 k PMMA (A5, 5% in anisole) electron-beam resist by spinning at 5,000 rpm for 45 seconds followed by baking at 180 °C on a hotplate for 60 seconds.
3. An electron-beam lithography exposure is carried out at an acceleration voltage of 30 kV and a current of 500 pA. The inverse of the resonator is exposed.

4. The exposed sample is developed in a solution of 3 parts IPA to 1 part methyl isobutyl ketone (MIBK) for 120 seconds followed by a rinse in IPA and blow drying with nitrogen.
5. The sample is given a 20 second oxygen plasma descum (`A_Descum_Graphite`) followed by an CHF_3/O_2 reactive ion etch (`A_SiO2_RIE`) for between 240 and 300 seconds.
6. Any residual PMMA is removed by soaking in acetone at $\sim 50^\circ\text{C}$.
7. Before wet etching the sample is wetted by placing it first in acetone, before transferring to methanol, IPA and then DI water without allowing it to dry.
8. The sample is then transferred from the water into hydrofluoric acid for 240 seconds.
9. After etching, the sample is soaked in DI water, before being transferred to IPA and then methanol; At this stage the sample is blow dried with nitrogen.

A.4.3 Indirect Fabrication of Torsional Resonators using a Membrane

1. The sample is given a four solvent clean (ethyl lactate, acetone, methanol and isopropyl alcohol (IPA)) with ultrasonic agitation.
2. The sample is coated with a 200 nm thick layer of 495 k PMMA (A5, 5% in anisole) electron-beam resist by spinning at 5,000 rpm for 45 seconds followed by baking at 180°C on a hotplate for 60 seconds.
3. The first electron-beam lithography exposure is carried out at an acceleration voltage of 30 kV and a current of 500 pA. An array of $\sim 1\ \mu\text{m}$ holes are patterned, their spacing determined by the final device dimensions. A dwell time of ~ 1000 ns is used, equivalent to an area dose of $\sim 500\ \mu\text{C}/\text{cm}^2$.
4. The exposed sample is developed in a solution of 3 parts IPA to 1 part methyl isobutyl ketone (MIBK) for 120 seconds followed by a rinse in IPA and blow drying

- with nitrogen.
5. The sample is given a 20 second oxygen plasma descum (`A_Descum_Graphite`) followed by an CHF_3/O_2 reactive ion etch (`A_SiO2_RIE`) for between 240 and 300 seconds.
 6. Any residual PMMA is removed by soaking in acetone at $\sim 50^\circ\text{C}$.
 7. Before wet etching the sample is wetted by placing it first in acetone, before transferring to methanol, IPA and then DI water without allowing it to dry.
 8. The sample is then transferred from the water into hydrofluoric acid for 360 seconds. The etch can be done in one go, however if the gold alignment marks begin to wrinkle and discolor the etch should be broken into smaller sections separated by 30 – 40 second periods where the sample is transferred to DI water. 3×120 second long sections seems to work fairly well.
 9. After etching, the sample is soaked in DI water, before being transferred to IPA; At this stage the sample is blow dried with nitrogen.
 10. The sample is recoated with a 200 nm thick layer of PMMA by spinning at 5,000 rpm for 45 seconds followed by baking in a convection oven at 180°C for 30 minutes.
 11. The second electron-beam lithography exposure is carried out at an acceleration voltage of 30 kV and a current of 500 pA. The resonator structures are defined during this exposure. A dwell time of $\sim 500 - 600$ ns is used, equivalent to an area dose of $\sim 250 - 300 \mu\text{C}/\text{cm}^2$.
 12. The exposed sample is developed in a solution of 3 parts IPA to 1 part methyl isobutyl ketone (MIBK) for 60 seconds followed by a rinse in IPA and blow drying with nitrogen.
 13. The devices are released using a 20 second oxygen plasma descum (`A_Descum_Graphite`) followed by an CHF_3/O_2 reactive ion etch (`A_SiO2_RIE`) for ~ 120 seconds.

-
14. Residual PMMA can be removed either by soaking in acetone or using an oxygen plasma.

Bibliography

- [1] K. L. Ekinici, X. M. H. Huang, and M. L. Roukes, “Ultrasensitive nanoelectromechanical mass detection,” *Applied Physics Letters*, vol. 84, no. 22, p. 4469, 2004.
- [2] Y. Yang, C. Callegari, X. Feng, K. Ekinici, and M. L. Roukes, “Zeptogram-scale nanomechanical mass sensing,” *Nano Letters*, vol. 6, no. 4, pp. 583–586, 2006.
- [3] D. Rugar, B. Stipe, H. Mamin, and C. Yannoni, “Adventures in attonewton force detection,” *Applied Physics A: Materials Science and Processing*, vol. 72 [Suppl.], pp. S3–S10, 2001.
- [4] H. Mamin and D. Rugar, “Sub-attonewton force detection at millikelvin temperatures,” *Applied Physics Letters*, vol. 79, no. 20, p. 3358, 2001.
- [5] D. Rugar, R. Budakian, H. J. Mamin, and B. W. Chui, “Single spin detection by magnetic resonance force microscopy,” *Nature*, vol. 430, pp. 329–332, July 2004.
- [6] M. Blencowe, “Quantum electromechanical systems,” *Physics Reports*, vol. 395, pp. 159–222, 2004.
- [7] A. D. O’Connell, M. Hofheinz, M. Ansmann, R. C. Bialczak, M. Lenander, E. Lucero, M. Neeley, D. Sank, H. Wang, M. Weides, J. Wenner, J. M. Martinis, and A. N. Cleland, “Quantum ground state and single-phonon control of a mechanical resonator,” *Nature*, vol. 464, pp. 697–703, Jan. 2010.
- [8] K. L. Ekinici and M. L. Roukes, “Nanoelectromechanical systems,” *Review Of Scientific Instruments*, vol. 76, p. 061101, 2005.

-
- [9] K. Ekinici, “Electromechanical Transducers at the Nanoscale: Actuation and Sensing of Motion in Nanoelectromechanical Systems (NEMS),” *Small*, vol. 1, no. 8-9, pp. 786–797, 2005.
- [10] A. Cleland and M. L. Roukes, “External control of dissipation in a nanometer-scale radiofrequency mechanical resonator,” *Sensors & Actuators: A. Physical*, vol. 72, no. 3, pp. 256–261, 1999.
- [11] R. G. Knobel and A. N. Cleland, “Nanometre-scale displacement sensing using a single electron transistor,” *Nature*, vol. 424, pp. 291–293, July 2003.
- [12] K. L. Ekinici, Y. T. Yang, X. M. H. Huang, and M. L. Roukes, “Balanced electronic detection of displacement in nanoelectromechanical systems,” *Applied Physics Letters*, vol. 81, no. 12, p. 2253, 2002.
- [13] P. A. Truitt, J. B. Hertzberg, C. Huang, K. L. Ekinici, and K. C. Schwab, “Efficient and sensitive capacitive readout of nanomechanical resonator arrays,” *Nano Letters*, vol. 7, no. 1, pp. 120–126, 2007.
- [14] S. S. Verbridge, D. F. Shapiro, H. G. Craighead, and J. M. Parpia, “Macroscopic tuning of nanomechanics: Substrate bending for reversible control of frequency and quality factor of nanostring resonators,” *Nano Letters*, vol. 7, no. 6, pp. 1728–1735, 2007.
- [15] Q. P. Unterreithmeier, S. Manus, and J. P. Kotthaus, “Coherent detection of nonlinear nanomechanical motion using a stroboscopic downconversion technique,” *Applied Physics Letters*, vol. 94, no. 26, pp. 263104:1–3, 2009.
- [16] N. O. Azak, M. Shagam, D. Karabacak, K. Ekinici, D. Kim, and D. Jang, “Nanomechanical displacement detection using fiber-optic interferometry,” *Applied Physics Letters*, vol. 91, p. 093112, 2007.
- [17] Q. P. Unterreithmeier, *Gradient Field Transduction of Nanomechanical Resonators*. PhD thesis, Ludwig–Maximilians–Universität München, Oct. 2010.

- [18] Q. P. Unterreithmeier, E. M. Weig, and J. P. Kotthaus, “Universal transduction scheme for nanomechanical systems based on dielectric forces,” *Nature*, vol. 458, no. 7241, pp. 1001–1004, 2009.
- [19] L. Novotny and B. Hecht, *Principles of Nano-Optics*. Cambridge: Cambridge University Press, 2006.
- [20] K. J. Lulla, *Dissipation and Nonlinear Effects in Nanomechanical Resonators at Low Temperatures*. PhD thesis, The University of Nottingham, Sept. 2011.
- [21] K. J. Lulla, R. B. Cousins, A. Venkatesan, M. J. Patton, A. D. Armour, C. J. Mellor, and J. R. Owers-Bradley, “Nonlinear modal coupling in a high-stress doubly-clamped nanomechanical resonator,” *arXiv.org*, vol. cond-mat.mes-hall, Apr. 2012.
- [22] A. N. Cleland, *Foundations of Nanomechanics: From Solid-State Theory to Device Applications*. Berlin ; New York: Springer, 2003.
- [23] C. Liu, *Foundations of MEMS*. Upper Saddle River, NJ: Pearson Prentice Hall, 2nd ed., 2006.
- [24] B. Witkamp, *High-frequency nanotube resonators*. PhD thesis, Technische Universiteit Delft, 2009.
- [25] J. P. Davis, D. Vick, D. C. Fortin, J. A. J. Burgess, W. K. Hiebert, and M. R. Freeman, “Nanotorsional resonator torque magnetometry,” *Applied Physics Letters*, vol. 96, no. 7, p. 072513, 2010.
- [26] P. Hagedorn and A. DasGupta, *Vibrations and Waves in Continuous Mechanical Systems*. Chichester: John Wiley & Sons, 2007.
- [27] J. P. Davis, D. Vick, P. Li, S. K. Portillo, A. E. Fraser, J. A. J. Burgess, D. C. Fortin, W. K. Hiebert, and M. R. Freeman, “Nanomechanical torsional resonator torque magnetometry,” *Journal of Applied Physics*, vol. 109, p. 07D309, 2011.

- [28] I. Wilson-Rae, “Intrinsic dissipation in nanomechanical resonators due to phonon tunneling,” *Physical Review B*, vol. 77, no. 24, p. 245418, 2008.
- [29] I. Wilson-Rae, R. A. Barton, S. S. Verbridge, D. R. Southworth, B. Ilic, H. G. Craighead, and J. M. Parpia, “High-Q Nanomechanics via Destructive Interference of Elastic Waves,” *Physical Review Letters*, vol. 106, p. 047205, 2011.
- [30] V. P. Adiga, B. Ilic, R. A. Barton, I. Wilson-Rae, H. G. Craighead, and J. M. Parpia, “Modal dependence of dissipation in silicon nitride drum resonators,” *Applied Physics Letters*, vol. 99, no. 25, p. 253103, 2011.
- [31] P. L. Yu, T. P. Purdy, and C. A. Regal, “Control of Material Damping in High-Q Membrane Microresonators,” *arXiv.org*, vol. cond-mat.mes-hall, Nov. 2011.
- [32] A. Venkatesan, K. J. Lulla, M. Patton, and A. D. Armour, “Dissipation due to tunneling two-level systems in gold nanomechanical resonators,” *Physical Review B*, vol. 81, p. 073410, 2010.
- [33] D. R. Southworth, R. A. Barton, S. S. Verbridge, and B. Ilic, “Stress and silicon nitride: A crack in the universal dissipation of glasses,” *Physical Review Letters*, vol. 102, p. 225503, 2009.
- [34] S. S. Verbridge, J. M. Parpia, R. Reichenbach, L. M. Bellan, and H. G. Craighead, “High quality factor resonance at room temperature with nanostrings under high tensile stress,” *Journal of Applied Physics*, vol. 99, p. 124304, 2006.
- [35] Q. P. Unterreithmeier, T. Faust, and J. P. Kotthaus, “Damping of Nanomechanical Resonators,” *Physical Review Letters*, vol. 105, p. 027205, July 2010.
- [36] D. Karabacak and T. Kouh, “Analysis of optical interferometric displacement detection in nanoelectromechanical systems,” *Journal of Applied Physics*, vol. 98, no. 12, p. 124309, 2005.
- [37] F. L. Pedrotti and L. S. Pedrotti, *Introduction to Optics*. Englewood Cliffs, N.J.: Prentice-Hall, 2nd ed., 1993.

- [38] T. Kouh, D. Karabacak, D. Kim, and K. Ekinici, “Diffraction effects in optical interferometric displacement detection in nanoelectromechanical systems,” *Applied Physics Letters*, vol. 86, no. 1, pp. 013106–013106–3, 2005.
- [39] D. Karabacak, *Resonant Operation of Nanoelectromechanical Systems in Fluidic Environments*. PhD thesis, Boston University College of Engineering, 2007.
- [40] E. Kreyszig, *Advanced Engineering Mathematics*. Hoboken, NJ: John Wiley & Sons, 9th ed., 2006.
- [41] J. Santos, A. Leite, and D. Jackson, “Optical fiber sensing with a low-finesse Fabry-Perot cavity,” *Applied Optics*, vol. 31, no. 34, pp. 7361–7366, 1992.
- [42] D. Rugar, H. Mamin, R. Erlandsson, J. E. Stern, and B. Terris, “Force microscope using a fiberoptic displacement sensor,” *Review Of Scientific Instruments*, vol. 59, no. 11, pp. 2337–2340, 1988.
- [43] E. D. Palik, ed., *Handbook of Optical Constants of Solids [Electronic Resource]*. San Diego: Academic Press, 1998.
- [44] I. Favero, C. Metzger, S. Camerer, D. Konig, H. Lorenz, J. P. Kotthaus, and K. Karrai, “Optical cooling of a micromirror of wavelength size,” *Applied Physics Letters*, vol. 90, no. 10, pp. 104101–104101–3, 2007.
- [45] C. Metzger, I. Favero, A. Ortlieb, and K. Karrai, “Optical self cooling of a deformable Fabry-Perot cavity in the classical limit,” *Physical Review B*, vol. 78, no. 3, p. 035309, 2008.
- [46] M. Vogel, C. Mooser, K. Karrai, and R. J. Warburton, “Optically tunable mechanics of microlevers,” *Applied Physics Letters*, vol. 83, no. 7, p. 1337, 2003.
- [47] T. J. Kippenberg and K. J. Vahala, “Cavity Opto-Mechanics,” *Optics Express*, vol. 15, no. 25, pp. 17172–17205, 2007.

- [48] Q. P. Unterreithmeier, T. Faust, S. Manus, and J. P. Kotthaus, “On-Chip Interferometric Detection of Nanomechanical Motion,” *Nano Letters*, vol. 10, no. 3, pp. 887–890, 2010.
- [49] P. Mulhern, T. Hubbard, C. S. Arnold, B. L. Blackford, and M. Jericho, “A scanning force microscope with a fiberopticinterferometer displacement sensor,” *Review Of Scientific Instruments*, vol. 62, no. 5, pp. 1280–1284, 1991.
- [50] D. Karabacak, T. Kouh, C. Huang, and K. Ekinici, “Optical knife-edge technique for nanomechanical displacement detection,” *Applied Physics Letters*, vol. 88, no. 19, p. 193122, 2006.
- [51] Attocube Systems, “Low Temperature Confocal Microscopy Product Catalog 2007-2008.” Attocube Systems, 2007.
- [52] A. Högele, S. Seidl, M. Kroner, K. Karrai, C. Schulhauser, O. Sqalli, J. Scrimgeour, and R. J. Warburton, “Fiber-based confocal microscope for cryogenic spectroscopy,” *Review Of Scientific Instruments*, vol. 79, p. 023709, 2008.
- [53] I. Bargatin, E. Myers, J. L. Arlett, B. Gudlewski, and M. L. Roukes, “Sensitive detection of nanomechanical motion using piezoresistive signal downmixing,” *Applied Physics Letters*, vol. 86, p. 133109, 2005.
- [54] I. Kozinsky, H. W. C. Postma, O. Kogan, A. Husain, and M. L. Roukes, “Basins of attraction of a nonlinear nanomechanical resonator,” *Physical Review Letters*, vol. 99, no. 20, p. 207201, 2007.
- [55] D. V. Pelekhov, J. B. Becker, and G. Nunes Jr, “Atomic force microscope for operation in high magnetic fields at millikelvin temperatures,” *Review Of Scientific Instruments*, vol. 70, p. 114, 1999.
- [56] M. J. Madou, *Fundamentals of Microfabrication: the Science of Miniaturization*. Boca Raton, Fla. ; London: CRC Press, 2nd ed., 2002.

- [57] P. Rai-Choudhury, ed., *Handbook of Microlithography, Micromachining and Micro-fabrication*. Bellingham, Wa: SPIE Optical Engineering Press, 1997.
- [58] K. Williams, K. Gupta, and M. Wasilik, "Etch Rates for Micromachining Processing-Part II," *Journal of Microelectromechanical Systems*, vol. 12, no. 6, pp. 761–778, 2003.
- [59] W. M. Haynes, ed., *CRC Handbook of Chemistry and Physics*. Boca Raton, Fla. ; London: CRC Press, 92nd ed., 2011.
- [60] J. C. McDonald, D. C. Duffy, J. R. Anderson, D. T. Chiu, H. Wu, O. J. A. Schueller, and G. M. Whitesides, "Fabrication of microfluidic systems in poly(dimethylsiloxane)," *Electrophoresis*, vol. 21, no. 1, pp. 27–40, 2000.
- [61] D. C. Duffy, J. C. McDonald, O. J. A. Schueller, and G. M. Whitesides, "Rapid prototyping of microfluidic systems in poly(dimethylsiloxane)," *Analytical Chemistry*, vol. 70, no. 23, pp. 4974–4984, 1998.
- [62] K. Tang, E. Liao, W. Ong, J. Wong, A. Agarwal, R. Nagarajan, and L. Yobas, "Evaluation of bonding between oxygen plasma treated polydimethyl siloxane and passivated silicon," *Journal of Physics: Conference Series*, vol. 34, p. 155, 2006.
- [63] L. San Emeterio Alvarez, K. Y. Wang, S. Lepadatu, S. Landi, S. J. Bending, and C. Marrows, "Spin-transfer-torque-assisted domain-wall creep in a Co/Pt multilayer wire," *Physical Review Letters*, vol. 104, no. 13, p. 137205, 2010.
- [64] G. White and P. Meeson, *Experimental Techniques in Low Temperature Physics*. Oxford: Clarendon, 4th ed., Dec. 2005.
- [65] Attocube Systems, *Attocube Systems' Flex Positioners: User Manual*.
- [66] Thorlabs, *HNL020R, HNL020L, HNL050R, HNL050L Red HeNe Laser System User Guide*, 2012.

-
- [67] E. G. Neumann, *Single-Mode Fibers: Fundamentals*. Berlin; New York: Springer, 1988.
- [68] H. Photonics, "Hamamatsu Photomultiplier Tube 1P28 ," tech. rep., Hamamatsu Photonics.
- [69] Hamamatsu Photonics, *Photomultiplier Tubes: Basics and Applications*, 3rd ed., 2007.
- [70] S. Breen, B. Paton, B. L. Blackford, and M. Jericho, "Fiber optic displacement sensor with subangstrom resolution," *Applied Optics*, vol. 29, no. 1, pp. 16–18, 1990.
- [71] J. Lee, J. Chae, C. Kim, H. Kim, S. Oh, and e. al, "Versatile low-temperature atomic force microscope with in situ piezomotor controls, charge-coupled device vision, and tip-gated transport measurement capability," *Review Of Scientific Instruments*, vol. 76, 2005.
- [72] Attocube Systems, "High-Precision, Real Time Displacement Sensor," tech. rep., 2010.
- [73] Attocube Systems, *Attocube Systems' ANC150 Piezo-Controller: User Manual*. Attocube.
- [74] C. Meyer, O. Sqalli, H. Lorenz, and K. Karrai, "Slip-stick step-scanner for scanning probe microscopy," *Review Of Scientific Instruments*, vol. 76, no. 6, p. 063706, 2005.
- [75] M. L. Boas, *Mathematical Methods in the Physical Sciences*. New York ; Chichester: John Wiley & Sons, 2nd ed., 1983.
- [76] J. Rychen, T. Ihn, P. Studerus, A. Herrmann, K. Ensslin, H. J. Hug, P. J. A. Van Schendel, and H. J. Güntherodt, "Operation characteristics of piezoelectric quartz tuning forks in high magnetic fields at liquid helium temperatures," *Review Of Scientific Instruments*, vol. 71, no. 4, p. 1695, 2000.

- [77] D. I. Bradley, P. Crookston, M. J. Fear, S. N. Fisher, G. Foulds, D. Garg, A. M. Guénault, E. Guise, R. P. Haley, O. Kolosov, G. R. Pickett, R. Schanen, and V. Tsepelin, “Measuring the Prong Velocity of Quartz Tuning Forks Used to Probe Quantum Fluids,” *Journal of Low Temperature Physics*, vol. 161, pp. 536–547, Oct. 2010.
- [78] R. Grober, J. Acimovic, J. Schuck, D. Hessman, P. Kindlemann, J. Hespanha, A. S. Morse, K. Karrai, I. Tiemann, and S. Manus, “Fundamental limits to force detection using quartz tuning forks,” *Review Of Scientific Instruments*, vol. 71, p. 2776, 2000.
- [79] M. Lee, J. Jahng, K. Kim, and W. Jhe, “Quantitative atomic force measurement with a quartz tuning fork,” *Applied Physics Letters*, vol. 91, p. 023117, 2007.
- [80] Nanonis GMBH, “Piezoelectric Quartz Tuning Forks for Scanning Probe Microscopy,” tech. rep., Nanonis GMBH.
- [81] M. E. Suddards, *Scanning Capacitance Microscopy in the Quantum Hall Regime*. PhD thesis, The University of Nottingham, 2007.
- [82] R. Blaauwgeers, M. Blazkova, M. Clovecko, V. B. Eltsov, R. de Graaf, J. Hosio, M. Krusius, D. Schmoranzer, W. Schoepe, L. Skrbek, P. Skyba, R. E. Solntsev, and D. E. Zmeev, “Quartz tuning fork: Thermometer, pressure- and viscometer for helium liquids,” *Journal of Low Temperature Physics*, vol. 146, no. 5-6, pp. 537–562, 2007.
- [83] Y. Qin and R. Reifenberger, “Calibrating a tuning fork for use as a scanning probe microscope force sensor,” *Review Of Scientific Instruments*, vol. 78, no. 6, p. 063704, 2007.
- [84] W. H. Chuang, T. Luger, R. K. Fettig, and R. Ghodssi, “Mechanical Property Characterization of LPCVD Silicon Nitride Thin Films at Cryogenic Temperatures,” *Journal of Microelectromechanical Systems*, vol. 13, pp. 870–879, Oct. 2004.
- [85] L. D. Landau and E. M. Lifshitz, *Theory of Elasticity*. Oxford: Pergamon Press, 3rd ed., 1970.

- [86] D. E. Chang, K. K. Ni, O. Painter, and H. J. Kimble, “Ultrahigh-Q mechanical oscillators through optical trapping,” *New Journal of Physics*, vol. 14, p. 045002, 2012.
- [87] R. Lifshitz and M. L. Roukes, “Thermoelastic damping in micro-and nanomechanical systems,” *Physical Review B*, vol. 61, no. 8, p. 5600, 2000.
- [88] B. L. Zink, B. Revaz, J. Cherry, and F. Hellman, “Measurement of thermal conductivity of thin films with a Si-N membrane-based microcalorimeter,” *Review Of Scientific Instruments*, vol. 76, p. 024901, 2005.
- [89] M. T. Alam, M. P. Manoharan, M. A. Haque, C. Muratore, and A. Voevodin, “Influence of strain on thermal conductivity of silicon nitride thin films,” *Journal of Micromechanics and Microengineering*, vol. 22, no. 4, p. 045001, 2012.
- [90] A. Jagannathan, R. Orbach, and O. Entin-Wohlman, “Thermal conductivity of amorphous materials above the plateau,” *Physical Review B*, vol. 39, no. 18, p. 13465, 1989.
- [91] N. Daldosso, M. Melchiorri, F. Riboli, F. Sbrana, L. Pavesi, G. Pucker, C. Kom-pocholis, M. Crivellari, P. Bellutti, and A. Lui, “Fabrication and optical characterization of thin two-dimensional Si₃N₄ waveguides,” *Materials science in semiconductor processing*, vol. 7, no. 4, pp. 453–458, 2004.
- [92] B. L. Zink and F. Hellman, “Specific heat and thermal conductivity of low-stress amorphous Si–N membranes,” *Solid State Communications*, vol. 129, no. 3, pp. 199–204, 2004.